UNIVERSITÀ DEGLI STUDI DI MESSINA

Dipartimento di Scienze Matematiche e Informatiche, Scienze Fisiche e Scienze della Terra

DOTTORATO DI RICERCA IN FISICA
XXX Ciclo

THERMODYNAMICS OF WATER AND BIOSYSTEMS

Dottorando:
Sebastiano VASI

Tutore:
Prof. Francesco MALLAMACE

Coordinatore:
Prof. Lorenzo TORRISI

"All things are from water and all things are resolved into water."

Thales

Riassunto

Il presente lavoro di tesi è incentrato sullo studio termodinamico dell'interazione dell'acqua con alcuni biosistemi, illustrando come l'acqua rivesta un ruolo importante nel "guidare" le proprietà di tali sistemi. In particolare, gli esperimenti sono stati condotti utilizzando la tecnica della Risonanza Magnetica Nucleare, passando dal metanolo, la più semplice molecola anfifilica, ad un sistema più complesso come il lisozima, una proteina enzimatica dotata di attività battericida.

Le misure di Risonanza Magnetica Nucleare sono state eseguite con uno spettrometro Avance della Bruker operante a 700 MHz ed utilizzando diverse tecniche e sequenze, tra cui il "Pulsed Field Gradient Stimulated Echo" e la "High-Resolution Magic Angle Spinning". La strumentazione utilizzata è localizzata nel Laboratorio di Fisica dei Sistemi Complessi gestito dal Prof. F. Mallamace, presso il "Dipartimento di Scienze Matematiche e Informatiche, Scienze Fisiche e Scienze della Terra" (MIFT) dell'Università di Messina.

Sono stati oggetto di studio molte grandezze dinamiche e termodinamiche dei sistemi investigati, tra cui la diffusione, misure ottenute mediante l'utilizzo di gradienti di campo magnetico che permettono di effettuare una codifica spaziale delle frequenze di precessione degli spin attivi, in grado quindi di rilevare uno spostamento degli stessi durante il tempo di osservazione. In particolare l'universalità e la rilevanza di temperature estremamente importanti per l'acqua sono state osservate anche nei processi caratterizzanti i sistemi acquosi. Un esempio è dato dalla temperatura "magica" di circa 315 K alla quale avviene un cambiamento nella dinamica dell'acqua in quanto l'acqua passa dall'essere un fluido normale all'essere un liquido complesso ed anomalo, e viceversa. Nel caso dei sistemi acquosi, per esempio acqua e proteina, tale temperatura rappresenta l'inizio del processo di "unfolding" della proteina in cui essa comincia a denaturare per assumerere lo stato di semplice catena polipeptidica lineare. I risultati ottenuti hanno permesso anche di mettere in evidenza l'importanza del legame idrogeno in relazione alla sua competizione con l'effetto idrofobico. Infatti, è tale competizione che genera un cambiamento nella dinamica dei sistemi acquosi rispetto al caso dei sistemi puri.

Tale lavoro ha potuto avvalersi di collaborazioni con il gruppo del Prof. E. H. Stanley del "Center for Polymer Studies and Department of Physics" della Boston University, Boston (USA) e del Prof. S.-H. Chen del "Department of Nuclear Science and Engineering" del Massachusetts Institute of Technology, Boston (USA).

Summary

This thesis focuses on the thermodynamical study of water interaction with some biosystems, illustrating how water plays an important role in "driving" the properties of such systems. In particular, the experiments were conducted by means of Nuclear Magnetic Resonance technique and by passing from methanol, the simplest amphiphilic molecule, to a more complex system such as lysozyme, an enzyme protein with bactericidal activity.

Nuclear Magnetic Resonance measurements were performed by means of a Bruker Avance spectrometer operating at 700 MHz and by using various techniques and sequences, including the Pulsed Field Gradient Stimulated Echo and the High-Resolution Magic Angle Spinning. The instrumentation used is located in the Laboratory of Physics of Complex Systems managed by Prof. F. Mallamace at the Department of Mathematical and Informatics Sciences, Physical Sciences and Earth Sciences (MIFT), University of Messina.

Many dynamic and thermodynamic quantities of the investigated systems have been studied, including diffusion obtained by the use of magnetic field gradients which allow to perform a spatial encoding of spin frequencies, thus able to detect a shift of the same during observation time. In particular, the universality and relevance of extremely important temperatures for water have been observed even in processes characterizing aqueous systems. An example is the "magic" temperature of about 315 K at which a change in water dynamics occurs as water passes from being a normal fluid to being a complex and anomalous liquid, and vice versa.

In the case of aqueous systems, e.g., in water and protein solution, such temperature represents the beginning of the unfolding process of the protein in which it begins to denature and to assume the state of a simple linear polypeptide chain. The results obtained also made it possible to highlight the importance of the hydrogen bond in relation to its competition with the hydrophobic effect. In fact, it is such a competition that generates a change in the dynamics of the aqueous systems with respect to the case of pure systems.

In this work, we collaborate with Prof. E. H. Stanley of the Boston University, Boston (USA) and Prof. S.-H. Chen of the Department of Nuclear Science and Engineering of the Massachusetts Institute of Technology, Boston (USA).

Acknowledgements

Firstly, I would like to give my sincere thanks to my girlfriend Sonia and to my entire family with all my heart for supporting and helping me in everyday life, because it is mainly thanks to them if today I have achieved this goal.

I would like to express my gratitude to my advisor Prof. F. Mallamace for the related research of my PhD studies and immense knowledge, and because he provides me the opportunity to join his team, and gave access to the laboratory. Besides my advisor, I thank my labmates, Dr. Carmelo Corsaro and Dr. Domenico Mallamace, not only colleagues with whom I have a lot of interesting discussions or endless work together, but friends with whom I have a lot of fun together. In particular, I am grateful to Dr. Corsaro for helping me during writing my thesis. Also I thank all the staff and my colleagues of the MIFT Department of the University of Messina, and in particular Prof. L. Torrisi and Dr. P. Donato for the useful help during these last three years.

My sincere thanks also goes to Prof. E. H. Stanley of the "Center for Polymer Studies and Department of Physics", Boston University (USA) and Prof. S.-H. Chen of the "Department of Nuclear Science and Engineering", Massachusetts Institute of Technology, Boston (USA).

Lastly, I would like to thank all the people that being part of my life and I have known during my PhD studies.

Contents

List of Figures

List of Tables

List of Abbreviations

AR	(pure) **AR**rhenius (behavior)
CS	**C**onformational **C**onstituents
CSA	**C**hemical-**S**hift **A**nisotropy
DRLS	**D**epolarized **R**ayleigh **L**ight **S**cattering
DSC	**D**ifferential **S**canning **C**alorimetry
DSE	**D**ebye-**S**tokes-**E**instein
EMCT	**E**xtended **M**ode **C**oupling **T**heory
EPSR	**E**mpirical **P**otential **S**tructure **R**efinement
FID	**F**ree **I**ndution **D**ecay
FSDC	**F**ragile-to-**S**trong **D**ynamic-**C**rossover
FST	**F**ragile-to-**S**trong **T**ransition
FT	**F**ourier **T**ransform
FWHM	**F**ull-**W**idth (at) **H**alf-**M**aximum
GPD	**G**aussian **P**hase **D**istribution (approximation)
H	**H**ydrogen
HB	**H**ydrogen **B**ond
HDA	**H**igh-**D**ensity **A**morphous (Phase)
HDL	**H**igh-**D**ensity **L**iquid (Phase)
HDS	**H**igh-**D**ensity **S**tructure
HR	**H**igh-**R**esolution
HR-MAS	**H**igh-**R**esolution **M**agic **A**ngle **S**pinning
LDA	**L**ow-**D**ensity **A**morphous (Phase)
LDL	**L**ow-**D**ensity **L**iquid (Phase)
LDS	**L**ow-**D**ensity **S**tructure
LLCP	**L**iquid-**L**iquid **C**ritical **P**oint
LLPT	**L**iquid-**L**iquid **P**hase **T**ransition
MCT	**M**ode **C**oupling **T**heory
MD	**M**olecular **D**ynamics
MRI	**M**agnetic **R**esonance **I**maging
MSD	**M**ean-**S**quared **D**isplacement
ND	**N**eutron **D**iffraction
NMR	**N**uclear **M**agnetic **R**esonance
PFG	**P**ulsed **F**ield **G**radient
PFGSE	**P**ulsed **F**ield **G**radient **S**pin-**E**cho
PFGSTE	**P**ulsed **F**ield **G**radient **ST**imulated (spin) **E**cho
RF	**R**adio-**F**requency
SA	**S**uper-**A**rrhenius (behavior)
SGP	**S**hort **G**radient **P**ulse (approximation)
SI	**S**ystème **I**nternational (d'unités)
SF	**S**ingularity-**F**ree (Scenario)
SLC	**S**tability **L**imit **C**onjecture
TE	**T**ime (of the) **E**cho
TMD	**T**emperature (of) **M**aximum **D**ensity

TMSC	**T**emperature **M**odulated **S**canning **C**alorimetry
VD	**V**ariable **D**elay (parameter)
VFT	**V**ogel-**F**ulcher-**T**amman
XAS	**X**-ray **A**bsorption **S**pectroscopy

Physical Constants

Boltzmann Constant	$k_B = 1.380\,648\,52(79) \times 10^{-23}\,\mathrm{J\,K^{-1}}$
Nuclear Magneton	$\mu_n = 5.05 \times 10^{-27}\,\mathrm{A\,m^{-2}}$
Proton's Gyromagnetic Ratio	$\gamma = 2.675\,221\,900(18) \times 10^8\,\mathrm{rad\,s^{-1}\,T^{-1}}$
Reduced Proton's Gyromagnetic Ratio	$\bar{\gamma} = 42.58 \times 10^8\,\mathrm{MHz\,T^{-1}}$
Reduced Planck Constant	$\hbar = 1.054\,571\,800(13) \times 10^{-34}\,\mathrm{J\,s\,rad^{-1}}$

List of Symbols

E_a	activation energy	J
m_l	angular quantum number	
l	azimuthal quantum number	
T_B	boiling point temperature	K
H_0	constant magnetic field	$A\,m^{-1}$
D	diffusion coefficient	$m^2\,s^{-1}$
S	entropy	$J\,K^{-1}$
S_{FT}	Fourier transformed signal	
T_L	fragile-to-strong dynamic crossover temperature	K
T_g	glass transition temperature	K
T_H	homogeneous nucleation temperature	K
h	hydration level	
r	interproton distance	$\text{Å}\,(10^{-10}\,m)$
c_P	isobaric specific heat capacity	$J\,g^{-1}\,K^{-1}$
T^*	"magic" temperature	K
B	magnetic field	T
g	magnetic field gradient	$T\,m^{-1}$
m_j	magnetic quantum number	
M	(macroscopic) magnetization	$N\,m\,T^{-1}$
T_M	melting point temperature	K
X_{MeOH}	methanol molar fraction	
t_α^{MeOH}	water relaxation time	s
s_m	molar entropy	$J\,K^{-1}\,mol^{-1}$
X	molar fraction	
υ_m	molar volume	$m^3\,mol^{-1}$
I	nuclear spin quantum number	
L_z	orbital angular momentum (along the z axis)	$N\,m\,s$
P	pressure	$Pa\,(N\,m^{-2})$
T_D	protein denaturation temperature	K
T_1	proton spin-lattice (longitudinal) relaxation time	s
T_2	proton spin-spin (transverse) relaxation time	s
t_α	relaxation time	s
s	spin quantum number	
S_z	spin projection angular momentum along the z-axis	$N\,m\,s$
m_s	spin projection quantum number along the z-axis	
B_0	static magnetic field	T
T	temperature	K
J_z	total angular momentum (along the z axis)	$N\,m\,s$
V	volume	m^3
X_W	water molar fraction	
t_α^W	water relaxation time	s
T_W	Widom line temperature	K

σ	chemical shift	
ρ	density	$\mathrm{kg\,m^{-3}}$
Δ	diffusion time	s
δ	duration of the gradient pulse	s
Ψ	echo attenuation	a. u.
ϕ	fluidity	$\mathrm{Pa^{-1}\,s^{-1}}$
ξ	hydrodynamic radius	m
κ_T	isothermal compressibility	$\mathrm{Pa^{-1}\,(m^2\,N^{-1})}$
ω_0	Larmor angular frequency	$\mathrm{rad\,s^{-1}}$
ν_0	Larmor frequency	$\mathrm{s^{-1}}$
μ	magnetic moment	$\mathrm{N\,m\,T^{-1}}$
ρ_N	number density of nuclei	$\mathrm{m^{-3}}$
τ	delay of the gradient pulse	s
τ_θ	reorientational correlation time	s
τ_c	rotational characteristic correlation time	s
α_P	thermal expansion at constant pressure	$\mathrm{K^{-1}}$
η	viscosity	$\mathrm{Pa\,s}$

Dedicated to those who love and supported me in achieving this goal.

Chapter 1

Water and water systems

1.1 Water

Water is the most copious inorganic molecule in the universe after hydrogen and it is essential to life and human activity [1–11]. Since water is absolutely essential to all living things, it should not be surprising that it has been considered a very important topic in both philosophy and science from ancient times. For example, in the VIth century BC, Thales of Miletus, philosopher, mathematician and astronomer, declared water to be the "principle element" of all things introduced for the first time by Aristotle. Thales claimed that from water all things emerge and to which they return, and, in addition, that all things sooner or later are water. Subsequently, Aristotle agreed that water was the "principle" of biology and thus of all living things. Indeed, all life on Earth needs water to survive (i.e., living organisms require, contain and maintain a balance of water) and/or to fulfill its functional activity. In the human body, water contributes to many biological and physiological functions such as the triggering of enzymatic activity (e.g., water-lysozyme interaction [4, 12, 13] in the human saliva). From the point of view of biology, water acts as a solvent or a solute, and a biomolecule, structuring proteins, nucleic acids and cells [1–5, 14]. Furthermore, water is unique compared to the other substances for all its properties (and anomalies), especially in the supercooled regime [4, 5, 15–17] where water remains liquid below the melting point.

In nature, it is possible to find water in gaseous, liquid and solid phases, and, in particular, water is the only inorganic substance that is liquid at atmospheric pressure and ambient temperature. In these conditions, it is an odorless, tasteless liquid, and appears colorless in small quantities, although it has a hint of blue [1, 7, 18]. Water freezes into ice below 0°C and boils above 100°C. Ice also appears colorless, and water vapor is essentially invisible as a gas.

Because of what has just been said, understanding the thermodynamical and dynamical properties of water is a challenging research subject in both science (including the fields of physics, chemistry, and biology) and technology. In particular, the focus of this thesis is on biological water, i.e. water located in living systems, and the study of its interaction with substances in aqueous solutions.

1.1.1 The water molecule

The water molecule consist in two hydrogen (H) atoms bonded with an oxygen (O) atom, so its chemical formula is H_2O[1] (figure 1.1). Each hydrogen is bound to the central oxygen atom by a covalent chemical bond, in which a pair of electrons are shared between them. The structure of the molecule is "bent" like, with positive and negative sites located in different places. In fact, the O atom has an average electron density about 10

---

[1]The molecular composition of water is due to the London scientist Henry Cavendish in 1781, establishing water as a compound, not an "element" [7, 9, 19].

times more intense than the H atoms and this provokes a dislocation of the center of the positive charge (half way between the two hydrogen atoms) on respect with the center of the negative charge (on the oxygen atom). Indeed, a different and "partial" positive and negative charge distribution is established, giving rise to a permanent dipole moment. In this way, each molecule of H_2O is electrically neutral, but polar. Polarity is responsible for some water's unique properties. For example, it makes water a "good solvent" allowing it to dissociate ions in salts and greatly bond to other polar substances (e.g., alcohols).
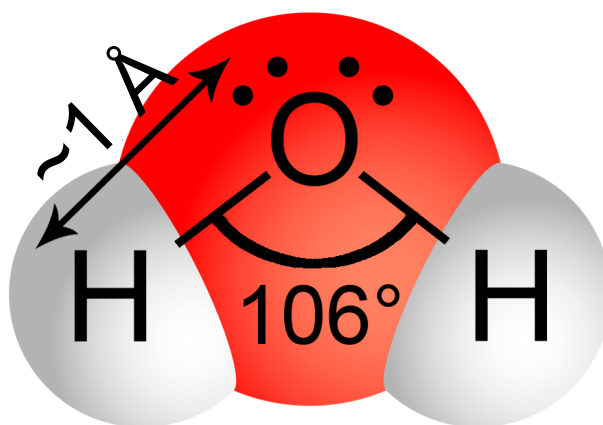

FIGURE 1.1: The liquid water molecule. As experimentally determined, a gaseous water molecule has an O–H length of 0.9718 Å and H–O–H angle of 104.474°, instead in the liquid water molecule these values are slightly greater [7]. Commonly used values for O-H lengths and H-O-H angles in the liquid water molecule are ranged between 0.957 Å and 1.00 Å, and from 104.52° to 109.5°, respectively. Note that the H-O-H angle in both liquid and gaseous phase is somewhat less than the tetrahedral angle (109.47°), because of the lower repulsion between H atoms than between them and the unbonded electrons (lone pairs) of the oxygen atom [1].

The presence of two lone pairs of electrons in the oxygen atom, in addition to be responsible for example of the H–O–H bond angle ($\sim 104.5°$ for the gas phase and $\sim 106°$ for the liquid phase) which is smaller than the typical tetrahedral angle of 109.47°, gives rise to an electrostatic-type bond between water molecules called hydrogen bond.

1.1.2 The hydrogen bond

The hydrogen bond[2] (HB) establishes in water when a hydrogen atom of one molecule ("proton donor") interacts with the oxygen atom of another water molecule ("proton acceptor").

The hydrogen bond in water can be considered as the sum of an electrostatic part ($\sim 90\%$) and a covalent one ($\sim 10\%$), but, normally, HB is established from a complex combination of interdependent interactions [1]. In particular, HBs are not static connections because they switch protons and partners without stop[3].

Liquid water is composed by a combination of (i) long, weak and bent HBs, (ii) short, straight and strong HBs, and (iii) hydrogen bonds with many intermediate between

---

[2]Hydrogen Bonding was first suggested in water by Latimer and Rodebush in 1920 [1, 2, 20, 21] and its concept and denomination were developed later by Pauling [22].

[3]Hydrogen bond lifetimes are 1–20 ps [7] whereas broken bond lifetimes are about 0.1 ps.
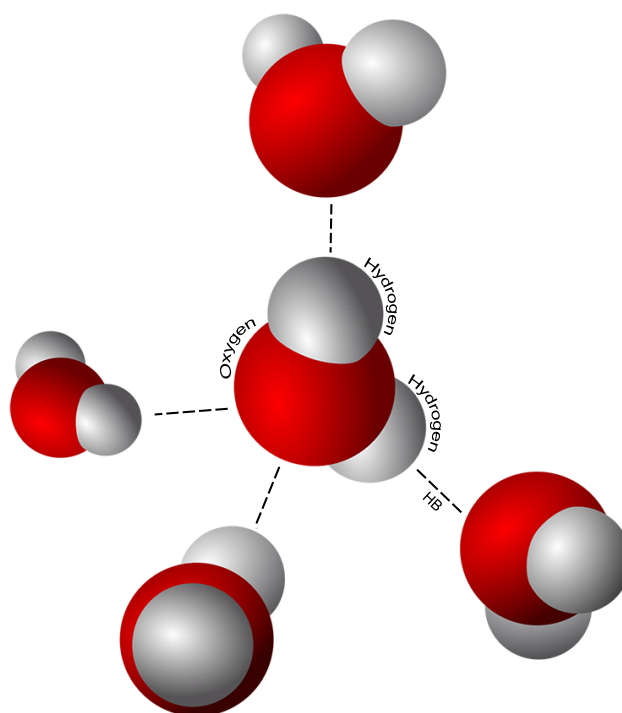
FIGURE 1.2: Hydrogen bond tetrahedron between water molecules in
the liquid phase.

(i) and (ii) [7]. When two isolated H_2O molecules come close, a dimer is formed by means of one or two HBs. In the first case (the most energetically favourable one), the structure formed is called linear, otherwise it is cyclic or bifurcated. When several water molecules approach, they assemble trimers and other different clusters as a function of their value of temperature and pressure[4]. In fact, when T decreases, the HBs cluster and form an open tetrahedrally coordinated HB network. In particular, when the T of the stable liquid phase is lowered, HB lifetime and cluster stability increase. Note that, in liquid water, each H_2O molecule can form at most four HBs with surrounding water molecules establishing, indeed, a HB tetrahedrally coordinated network. This structure emerges because each electrons of the lone pairs of the oxygen and each hydrogen of a water molecule can establish a HB with a H atom and two O atoms of different water molecules, respectively. This situation is well evident in figure 1.2. Generally, water molecules have the ability to form an extended dynamic HB network with localized and structured clustering.

From the point of view of the binding energy, in liquid water, the H atom is connected to the O atom of the same water molecule by means of a covalent bond (~ 492 kJ/mol), but has an additional energy of attraction to the oxygen of another water molecule (hydrogen bond enthalpy: ~ 23 kJ/mol [23]). In particular, this strong attraction (called indeed the hydrogen bond) has an energy strength in liquid water far greater and more directional at room temperature than Van der Waals interaction forces (~ 5.5 kJ/mol) [1, 7, 11].

Anyway, the physics of hydrogen bond, for its complexity and importance not only in water and aqueous systems, should require a complete treatise [7, 11]. It is really important to stress the fact that H_2O molecules have the tendency to attract each other

---

[4]HB length in water depends on temperature and pressure

strongly by means of hydrogen bonds. In particular, HB is the principal addresser for the complex phase diagram of water.

1.1.3   Water phase diagram

In nature, water can be found in gaseous, liquid and solid phases[5] as showed in figure 1.3, a (P,T) plot that represents the phase diagram[6] of water.
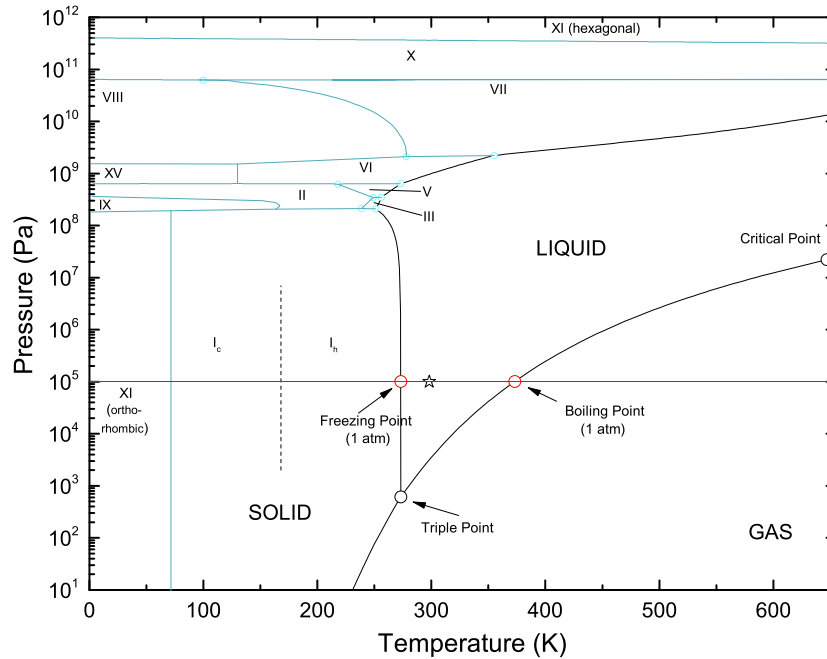
FIGURE 1.3: The (*P,T*) phase diagram of water. The black lines represents the phase curves that divide the physical states of water. Freezing, boiling and triple points are reported. The star (☆) denotes the standard ambient condition. The thirteen forms of ice are also indicated and separated by light blue lines.

At standard ambient temperature and pressure (marked with a ☆ in figure 1.3) water is a liquid, but it becomes gaseous (i.e., water vapor) if its temperature is increased above 100°C or solid (i.e., ice) lowering the temperature below 0°C, at fixed pressure. These "phase transitions" at pressure of 1 atm are denoted with a red line in figure 1.3 that crosses the melting point of ice (or the freezing point of liquid water) at $T_M \sim 273$ K and the boiling point of water at $T_B \sim 373$ K. In particular, the range defined by these equilibrium points corresponds to the stable liquid range. Furthermore, there is a special point at 273.16 K and 611.657 Pa called "triple point" where liquid water, gaseous water and hexagonal ice stably coexist, and where both the melting point and the boiling point are equal.

---

[5]In thermodynamics, a phase is a region of a system in which all physical properties of a material are basically uniform

[6]Phase diagrams illustrate the preferred physical states (phase) of matter at different temperatures and pressure. Each equilibrium curve (phase line) on a phase diagram denotes a phase boundary and gives the conditions when two phases may stably coexist because these states have the same Gibbs free-energy. In fact, here, just a very small change in temperature or pressure possibly causes a phase transition from one physical state to the other. In particular, where three phase lines join each other, there is a "triple point", when even three phases stably coexist.

The end point of the phase curve that denotes conditions under which liquid water and its vapor become indistinguishable from each other is the "critical point", defined by a critical temperature T_c and a critical pressure P_c. At temperatures above T_c a gas cannot be liquefied.

Anyway, the phase diagram of water is quite rich. For example, as shown in figure 1.3, at low temperatures, in its crystalline state, water is found to exist in thirteen different forms, nine of which are stable (ices II, III, V, VI, VII, VIII, X, XI, hexagonal I_h) over a particular ranges of temperature and pressure, and four are metastable (ices IV, IX, XII and cubic I_c). The known ices can be partitioned into the low-pressure ices (I_h, I_c and XI), high pressure ices (VII, VIII and X) and the others (found in the range of moderate pressures around 1 GPa). For example, below 273 K and at 1 atm, the stable crystalline state is the so-called Ice I_h. Here each water molecule has four nearest neighbours consituting, as already mentioned before, a regular tetrahedron held (together) by HBs. Because of the strong directionality of the hydrogen bond, this kind of tetrahedrally coordinated network results to be open. It is important to stress that water molecules can form an extended dynamical HB network and this clustering behavior is commonly accepted to be the cause of water anomalous properties.

1.1.4   Anomalous properties of water

Water is characterized by several uncommon thermodynamic and dynamical properties or anomalies that make it a "sui generis" liquid[7]. So, although it is an apparently simple molecule (see figure 1.1), water shows anomalous and complex behaviors mostly due to its HBs [22, 26, 27], and it seems that life and its processes depend on these anomalous properties [2, 6, 7, 11, 26].

The high cohesion between water molecules due to HBs gives it a high freezing and melting point, and it is because of these that in our planet we find more water in its liquid state. Furthermore, water properties such as its large heat capacity and its high content in organisms permit to more easily control our body temperature. As already mentioned, water has unique hydration properties towards important biological macromolecules (e.g., proteins) that regulate their structures and biological functions [1, 4, 12, 13] and it is also an excellent solvent due to its polarity, high relative permittivity (dielectric constant) and small size.

Nowadays, over 70 anomalies have been found for water [7]. Figure 1.4 displays a detailed region of the phase diagram of figure 1.3 in which some peculiar properties of water are evinced. In particular, it is noteworthy to attention the supercooled regime in which these anomalies become more evident [16, 25]. At atmospheric pressure, water can be "supercooled" down to its crystal homogeneous nucleation at $T_H \sim 231$ K, because at this temperature the nucleation rate suddenly increases [16], and it is not possible to find water in its liquid state below this point. In the supercooled regime, water is in a metastable state, a condition of precarious equilibrium in which it is prepared to collapse in its crystalline state when a perturbation is applied. Note that the process of supercooling depends on the purity of water and the freedom from nucleation sites in the cooling of liquid water [16]. Like any other liquid, water can be also superheated over its boiling point, without going through a phase transition, until ~ 553 K. As seen for the supercooled water, the rate of nucleation control the superheating process too. Thus it is possible in principle to have liquid water within a huge temperature range (231–553 K).

---

[7]The properties of water are seen to be anomalous on respects the materials used in the comparison and the interpretation of the term "anomalous" [7]. In the past decades, a lot of articles have been published on water anomalies, even an historical study [24] Today, water scientists agree that water is the most anomalous substance [25].

These metastable limits are not thermodynamic but kinetic in nature; so, they occur only when the nucleation time is shorter than the experimental observation time.
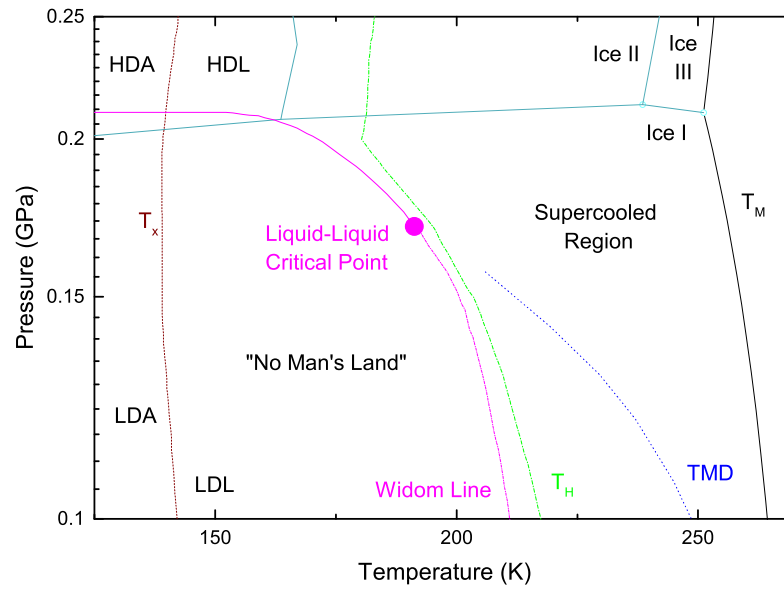

FIGURE 1.4: The (P,T) phase diagram of water in the frame of its polymorphism and the supercooled regime (see the text for more details). At ambient pressure, metastable supercooled water is located on the phase diagram between the melting temperature $T_M \sim 273$ K and the homogeneous nucleation temperature $T_H \sim 231$ K. The amorphous phases, LDA and the HDA, and the LDL and HDL phases are reported together with the melting T_M, the maxima density TMD and the homogeneous nucleation temperature T_H and the crystallization T_X loci. The Liquid-Liquid critical point and the Widom line are also reported and they will be described later.

Liquid water experiences a glass transition[8] when the cooling rate is very high ($\sim 10^6$ K/s) [16, 28, 29] becoming an amorphous solid at the temperature $T_g \sim 130$ K[9] [31, 32]. So, below the glass transition temperature T_g, water exists as glass; above this temperature, it becomes a highly viscous fluid that crystallizes spontaneously into cubic ice (I_c) at $T_X \sim 150$ K.

The region between T_H and T_X represents the temperature range where liquid water is not easily accessible experimentally, known as "No Man's Land" of the phase diagram (see figure 1.4).

Unlike most other substances, glassy water is characterized to be "polyamorphic"[10] at least in two different forms, known as low-density amorphous water (LDA) and high-density amorphous water (HDA), separated by a first-order phase transition and that can

---

[8]The glass transition is a "dynamic arrest" phenomenon (DA) in amorphous materials from a "viscous" state to a noncristalline "glassy" state by cooling fast enough to avoid crystallization [16]. In such conditions, the units constituting the system, switching from single molecules to clusters of molecules, interact more strongly and their dynamics slows down considerably: therefore, it is observed a drastic change of the physical properties of the system. This phenomenon is marked by the glass transition temperature T_g that is different for each material. In fact, this temperature depends on the strength of the interparticle interactions, i.e., the "bonds" that are being broken as the particles rearrange.

[9]It has been argued that the glass transition temperature for water is higher than about 130 K [30]

[10]Polyamorphism is the phenomenon that predicts for a substance its existence in several amorphous modification with different properties [4].

be transformed one into the other by tuning the pressure [4, 15, 29, 33–35]. This "polymorphic glass transition" is combined with a large and sharp variation in the system volume when thermodynamic parameters such as temperature change infinitesimally.

This polyamorphism of water in conjunction with HB networking suggest that liquid water can also be polymorphous, i.e., a mixture of a high-density liquid (HDL) and a low-density liquid (LDL) [16]. In the HDL form, which rules for high temperatures, the local tetrahedrally coordinated structure is not perfectly established, but in the LDL phase, a more open "ice-like" HB network arises.

Some of the most known anomalies of water at atmospheric pressure are (i) the maximum of the density ρ at ~ 277 K (figure 1.5), (ii) the zero value of the coefficient of thermal expansion α_P at ~ 277 K (figure 1.6a), (iii) the minimum of the isothermal compressibility κ_T at ~ 319 K (figure 1.6b), and (iv) the minimum of the isobaric specific heat capacity c_P at ~ 309 K (figure 1.6c).

The density maximum is the reason of the water expansion on heating or cooling at ~ 277 K. Technically, this maximum at 4°C is caused by the contrasting effects due to the increasing of temperature that provides both structural collapse (i.e., an increase of density) and thermal expansion (i.e., a lowering of ρ) [7].
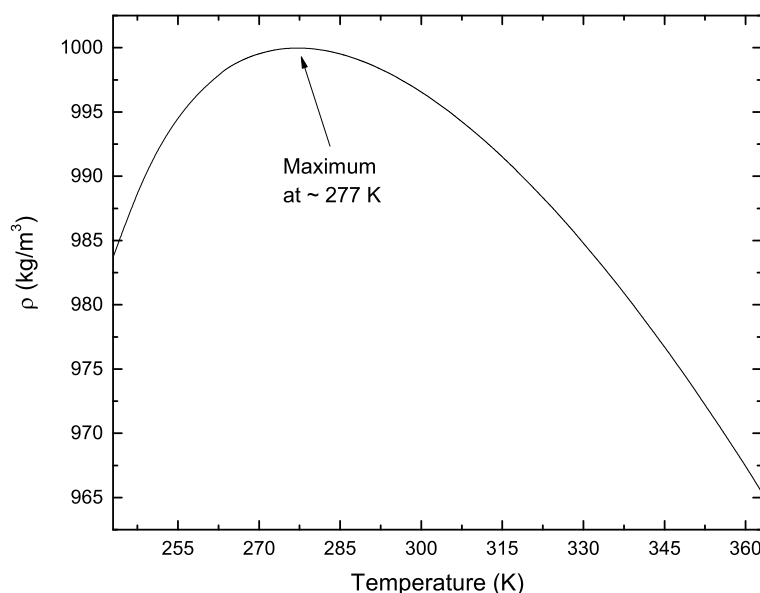
FIGURE 1.5: The temperature dependence of liquid water density ρ at atmospheric pressure. The density maximum is well evident at ~ 277 K. Data taken from [36–38].

At higher temperatures there are more high-density structures (HDS), whereas at lower temperatures there is a higher concentration of low-density structures (LDS). Increasing the temperature, the "transition" from LDS to HDS occurs with positive changes in both enthalpy and entropy due to the greater hydrogen bond bending and the less ordered structure, respectively.

The central property of the water density anomaly is the locus of temperatures at which the density is maximum at fixed pressure that is known as temperature of maximum density (TMD). Note that, if the pressure is positive, this locus has a negative slope in the (P,T) plane. This happens because when T is lowered, the compressibility of liquid water increases [29].

The density maximum results in several important features that affect life. For example, the freezing of rivers, lakes and oceans is from the top down, so permitting survival of the bottom ecology [7].

In addition, at atmospheric pressure, liquid water shows another peculiarity, that is the modulus of its response functions [11] increases sharply on reducing the temperature, diverging towards the supercooled region [16, 29]. Figure 1.6 shows the T dependence of some liquid water response functions at 1 atm.
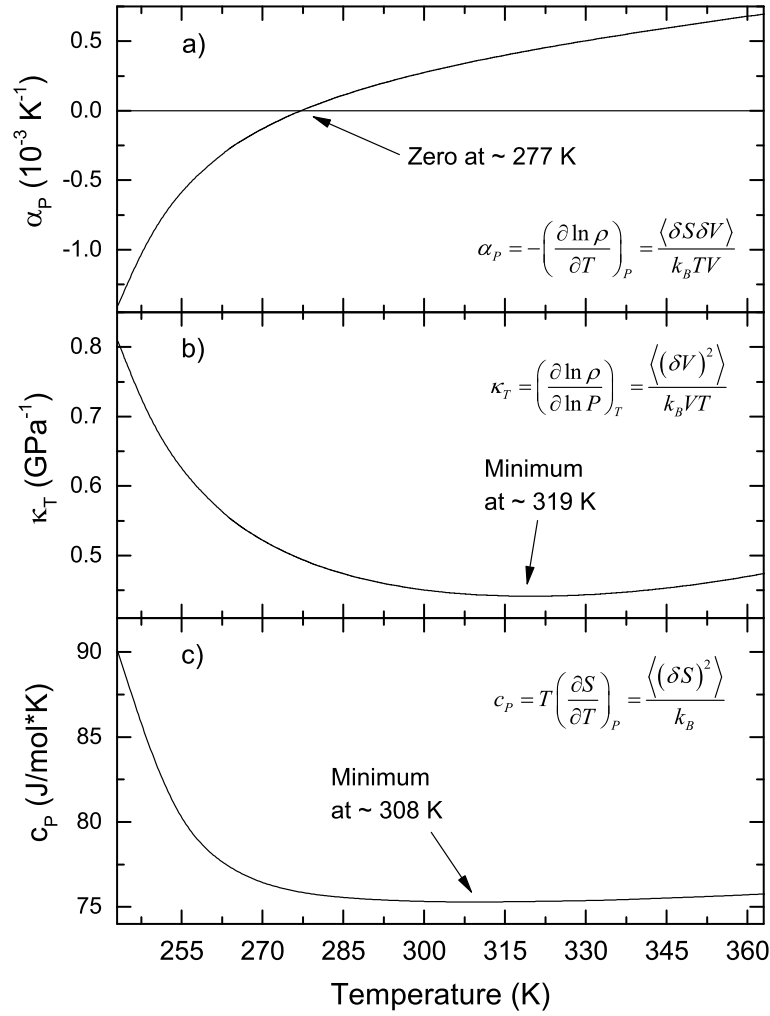
FIGURE 1.6: The temperature dependence of liquid water a) thermal expansion coefficient α_P, b) isothermal compressibility κ_T and c) isobaric specific heat c_P at atmospheric pressure. Equations for each response function are also reported. Data taken from [36, 39].

The first derivative of the natural logarithm of density ρ with respect to the temperature T at constant pressure P determines the coefficient of thermal expansion α_P

$$\alpha_P = -\left(\frac{\partial \ln \rho}{\partial T}\right)_P \tag{1.1}$$

---

[11]In thermodynamics, the response functions represent the variation of a system's thermodynamic observables (e.g., entropy S) and potentials with respect to system parameters (e.g., temperature T).

that can be also express as the cross-correlation between δS and δV, the entropy and volume fluctuations, respectively:

$$\alpha_P = \frac{\langle \delta S \delta V \rangle}{k_B T V} \tag{1.2}$$

Note that δ represents the variation about the mean value of a thermodynamic quantity, k_B is the Boltzmann constant and V being the mean value of δV for a fixed number of molecules. As shown in figure 1.6a, α_P is zero before the melting point, at ~ 277 K, location of the already described maximum value of water density. It is noteworthy that the locus of points where α_P changes its sign coincides with the TMD. In particular, lowering the temperature, the coefficient of thermal expansion becomes negative, and it is a very anomalous behavior compared with normal liquids that remain positive with an almost linear dependence on temperature. In fact, liquids expand on heating, while water contracts with increasing temperature for $T < 277$ K.

The variation of the natural logarithm of the density ρ with respect to the natural logarithm of pressure P at constant T defines the isothermal compressibility κ_T

$$\kappa_T = \left(\frac{\partial \ln \rho}{\partial \ln P} \right)_T \tag{1.3}$$

that is proportional to the microscopic volume fluctuations δV:

$$\kappa_T = \frac{\langle (\delta V)^2 \rangle}{k_B T V} \tag{1.4}$$

The T dependence of the isothermal compressibility is strictly related to the slope of the TMD in the (P,T) plane [40]. In a normal liquid, reducing the temperature, κ_T decreases, whereas in water, as pointed out in figure 1.6b, it increases sharply at $T = 319$ K towards lower temperatures. In addition, from experimental data [41], the lower temperature behavior appears to be described by a power law:

$$Y(T) = A \left(\frac{T}{T_L} - 1 \right)^{\gamma} \tag{1.5}$$

where Y is a thermodynamic quantity, A its amplitude and γ is a critical exponent associated to the divergence of Y at the singular temperature T_L.

The variation of the entropy S with respect to T at constant P multiplied by the temperature determines the isobaric specific heat c_P:

$$c_P = T \left(\frac{\partial S}{\partial T} \right)_P \tag{1.6}$$

that is, microscopically, proportional to entropy fluctuations δS at fixed pressure:

$$c_P = \frac{\langle (\delta S)^2 \rangle}{k_B} \tag{1.7}$$

in which it has been considered the number of moles n equal to 1. The isobaric specific heat of water behaves like its κ_T, but the increase starts at $T = 308$ K (see figure 1.6c). In fact, the water structure equilibrium shifts towards LDS as the temperature is reduced, causing great changes in entropy fluctuations. In particular, at supercooling temperatures where a much larger shift arises, c_P increases a lot and follows a power law similar to that of equation 1.5.

Lowering the temperature, the variation of water response functions appears more pronounced (and less when a pressure is adopted [29]), and, in particular, Speedy and

Angell [42] could assert that the characteristic relaxation times and the thermodynamic response functions of water diverge at a peculiar temperature $T_L = 228$ K. Note that this temperature lies in the already defined "No Man's Land". So, experiments performed within this region could be very useful for understanding the physical origin of this apparent singular temperature T_L, giving possible explanations of many open questions concerning the properties of supercooled water [43].

Water is characterized even by peculiar dynamical properties because of the competition at equilibrium between HB and Van der Waals interactions. Transport coefficients such as viscosity η (or structural relaxation time t_α) and translational diffusion D show a particular trend at lower temperatures when the LDS predominate.

In water, the shear viscosity η^{12} is marked by a large cohesivity due to its extensive 3D hydrogen bonding (figure 1.7 (top)). In fact, HBs tend to form more ordered (and symmetrical) structures, whereas the van der Waals interactions (together with the thermal energy) have the inclination to assemble more packed disordered structures (more similar to those of normal liquids) in conjunction with the thermal energy. As mentioned before, reducing the temperature, HBs win over van der Waals interaction resulting in an increase of the number of LDS with respect to HDS [44]. In this way, the majority of clusters are larger and their presence leads to an increase of viscosity due to a reduction of the movement.

As usually happens when pressure is applied to a liquid, its molecules are forced to stay together and holes and defects vanish increasing the viscosity of the liquid. In liquid water, the application of a pressure provokes the break of the tetrahedral HB network (i.e., the LDS), that is the molecular mobility increases. In fact, the LDS reduce its number and size under pressure, and water will become more like a normal liquid. The variation of the shear viscosity with respect to pressure is shown in figure 1.7 (bottom). It looks clear that it becomes more pronounced at low temperature, where the number of LDS is bigger [45].

In particular, viscosity is connected to the already mentioned glass transition temperature T_g. It is possible to define T_g as the temperature at which viscosity reaches the value of 10^{13} poise [47]. Using Angell's interpretation [28, 30, 48], the "fragility" of a glass-former is described in terms of the deviation of its viscosity and relaxation time t_α temperature dependence from simple Arrhenius behavior. A supercooled liquid is termed "fragile" when it is characterized by a highly non-Arrhenius temperature dependence of t_α; whereas, a supercooled liquid is "strong" when its viscosity shows a temperature dependence close to the Arrhenius law. A fragile liquid changes a lot its structure with temperature; on the contrary, the structure of a strong liquid changes a little when temperature changes. Furthermore, strong liquids become fragile on compression, and this behavior can be related to a polyamorphism in the glassy state. The pure Arrhenius (AR) behavior belonging to strong liquids is identified by an activation energy E_a that is temperature-independent. In this case, the viscosity η is usually written as

$$\eta = A \exp\left(\frac{E_a}{k_B T}\right) \tag{1.8}$$

where A is just a temperature-independent factor, like E_a, and k_B is the Boltzmann's constant. On the other hand, the fragile or Super-Arrhenius (SA) behavior was usually treated with a Vogel-Fulcher-Tamman (VFT) equation [49–51] in which, lowering the temperature, the effective activation energy value increases. In this frame, the viscosity is represented by the following law

---

[12]The shear viscosity of a liquid is established by the cohesiveness of molecules, i.e., the forces holding the molecules together.
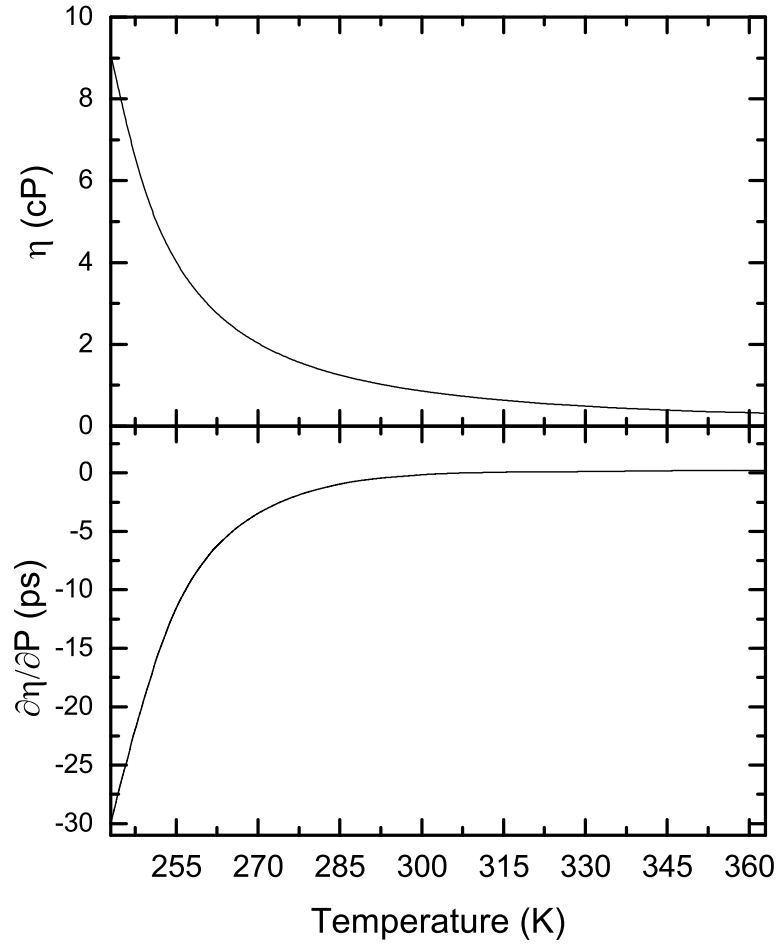
FIGURE 1.7: (Top) Temperature dependence of water shear viscosity at atmospheric pressure and (bottom) its variation with respect to pressure as a function of temperature. Data taken from [45, 46].

$$\eta = A \exp\left(\frac{B}{T - T_0}\right) \tag{1.9}$$

where A and B are factors independent from T and T_0 is the "ideal" glass transition temperature (known as the Kauzmann temperature [30]) which is kinetic in nature. The power law approach has a more physical meaning with respect to the VFT method. In fact, water is one of the most known and studied fragile liquid above 235 K [52], and, in particular, it seems that its viscosity follows a power law diverging at about 228 K [42]. Anyway, the temperature dependence of η must change from its power law form below 235 K because of the presence of T_g at below 180 K. So, it has been proposed [53, 54] that supercooled water experiences a "fragile-to-strong" transition (FST) around the crossover temperature of 228 K, and that it is due to an end point in the formation of a hydrogen bonded tetrahedral network structure [52].

Another transport parameter of great importance is the translational diffusion D. It represents the molecular transport driven by the kinetic energy and it is also related to the size of the diffusing object and the viscosity of the system through the Stokes-Einstein (SE) relation

$$D = \frac{k_B T}{6\pi\eta\xi} \tag{1.10}$$

in which ξ is the hydrodynamic radius for a spherical molecule. It has been reported that this relation breaks down at temperatures not far above the glass transition temperature T_g [55] and also that, for supercooled water, the SE is no longer valid well above T_g, occurring at about 225K [56, 57]. The T-dependence of D in water was shown in figure 1.8 [58, 59]. In particular, by means of Pulsed Field Gradient Spin-Echo (PFGSE) Nuclear Magnetic Resonance (NMR), Price et al. were able to reach 238 K and they found that, lowering the temperature, the diffusion behavior became non-Arrhenius and can be described by a VFT law like that of equation 1.9.
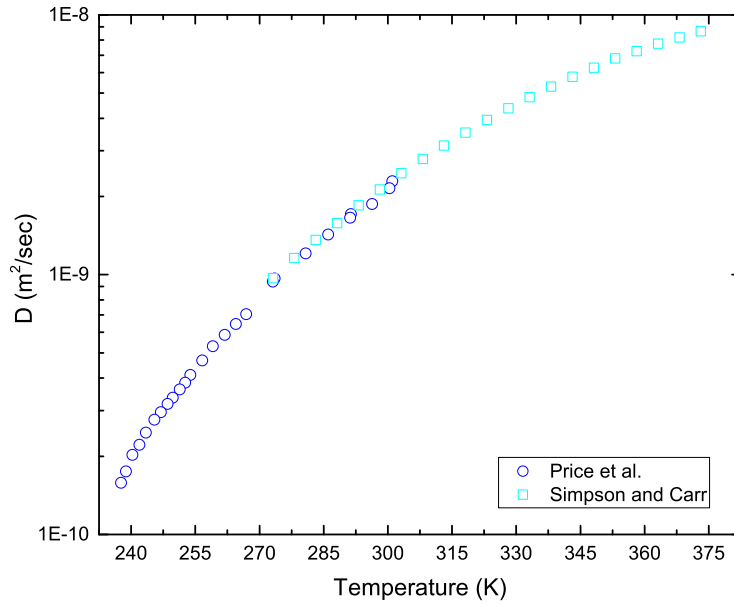
FIGURE 1.8: Temperature dependence of supercooled water self-diffusion in a lin-log plot. Data taken from [58] (dark blue circles) and [59] (light blue squares).

In table 1.1 are listed some of the most known thermal properties of water at 1 atm.

TABLE 1.1: List of some physical characteristic properties of water phases at atmospheric pressure [37].

	Temperature T (K)	Density ρ (kg/m^3)	Specific Heat C_p (J/mol·K)	Thermal Cond. k (W/m·K)	Viscosity η (cP)
liquid	293.16	998.21	75.38	0.56	1.79
vapor	373.16	0.6	37.47	0.03	0.01

Note that Mallamace et al. [60] presented a very complete overview about transport properties and anomalies of water, especially in the supercooled region.

1.1.5 Theoretical models and scenarios

In order to comprehend the anomalous and chemico-physical properties of liquid water, different theoretical models have been developed. However, we will detail only the recent three most plausible interpretations [29].
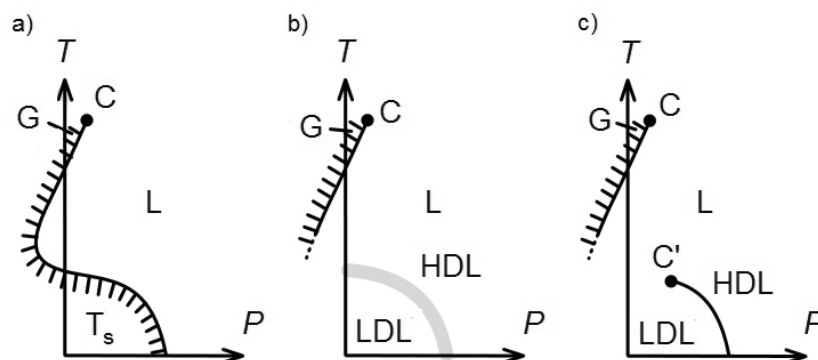
FIGURE 1.9: The (P,T) planes representing the thermodynamic behavior of water predicted by three competing theories, a) the stability limit hypothesis, b) the percolation picture (and singularity-free hypothesis), and c) the liquid–liquid phase-transition hypothesis. Here C denotes the known critical point, C' indicates the hypothesized second critical point, and T_s shows the locus of spinodal temperatures. G and L denote the low-density and high-density fluid phases that exist below C, whereas LDL and HDL denote the low-density and high-density liquid phases that exist below C'. Figure adapted from [61].

Stability limit conjecture

In 1976, Speedy and Angell hypothesized that the temperature $T_L = 228$ K may be consistent with the limit of mechanical stability for the supercooled liquid water [42]. On the basis of this assumption, in 1982 Speedy [62] proposed an "interpretation" to explain the thermodynamics of metastable water, the Stability Limit Conjecture (SLC), according to which the increment in response functions for supercooled water is generated by the approach to the spinodal curve[13], the locus of the points where superheated liquid water becomes unstable with respect to the vapour phase (T_s curve in figure 1.9a). In normal liquids, the spinodal starts at the liquid-gas critical point and, in the (P,T) plane, it has a positive slope and decreases monotonically with decreasing T along a path lying below the liquid-gas coexistence curve. According to Speedy's interpretation, in liquid water, the spinodal is curved inwards instead: it has a minimum at negative P and, decreasing T, it passes back to positive P.

In particular, the spinodal can be considered a locus of diverging density and entropy fluctuations [29], so its retracing character would indeed demonstrate some of the experimentally observed water's anomalies. In fact, the maximum in the density ρ of water at 277 K and the minimum in the isothermal compressibility κ_T at 319 K are possibly manifestations of spinodal-induced thermodynamic singularities occurring in the supercooled region. From a thermodynamic point of view it appears that the slope in the (P,T) plane of a spinodal curve must shift sign upon meeting a line along which the thermal expansion coefficient α_P becomes zero as showed in figure 1.6a [62, 63]. This line is the already mentioned temperature of maximum density (TMD) that is the locus of temperatures at which the density is maximum at fixed pressure. Therefore, for liquids with a density maximum such as water, the most physically plausible way for the TMD line to terminate is at an intersection with a spinodal line [63]. But, the situation in which it is possible the intersection in the (P,T) plane of a positively sloped spinodal line with

---

[13]The liquid spinodal line, or simply spinodal, designates the limit of stability of the (metastable) liquid state with respect to fluctuations toward a thermodynamically stable phase, such as the gas.

a negatively sloped TMD line involves that the liquid spinodal has a minimum at the intersection point [62]. So, at T less than that of the intersection point, the spinodal is negatively sloped and will occur at higher P as T decreases. Since the intersection of the TMD and spinodal lines is in general expected to occur in the negative P region of the (P,T) plane, the spinodal curve T_s changes from negative to positive P as T decreases, as predicted by the SLC, and illustrated in figure 1.9a.

All the considerations done before allow to predict the behavior of the spinodal line near to specific points, such as its intersection with the TMD line. Anyway, the SLC does not provide informations on the specific shape of the spinodal in the entire (P,T) plane. The real lack of this interpretation is just in the retracing of spinodal to positive pressure that, e.g., can generate another lower (implausible) critical point for the vapour–liquid transition [29]. To investigate this evidence, several simulation studies have been performed. For example, Sastry et al. [64], Sasai [65] and Borick et al. [66], using lattice models with directional interactions, demonstrated that the intersection of the TMD and the spinodal causes the latter to retrace. However, the spinodal does not reach positive pressure and it is replaced by a locus of limits of stability of the supercooled liquid with respect to the solid phase. Furthermore, Poole et al. [67], by means of molecular dynamics (MD) simulations found that the spinodal of liquid water is found to be not reentrant and that the TMD line changes slope in the metastable region of the phase diagram at negative pressure.

Singularity-free scenario

Another hypothesis explaining water anomalies is the singularity-free (SF) scenario (figure 1.9b). In this interpretation, the increases in water response functions upon supercooling (figure 1.6) are illustrated as a consequence of the existence of density anomalies [40, 68]. As an example, Sastry et al. [40] proved that the increment of κ_T on cooling below a negatively sloped TMD line is a requirement of thermodynamics, as stated in the following equation:

$$\left(\frac{\partial \kappa_T}{\partial T}\right)_{P,\text{TMD}} = \frac{1}{v}\frac{\frac{\partial^2 v_m}{\partial T^2}}{\left(\frac{\partial P}{\partial T}\right)_{\text{TMD}}} \tag{1.11}$$

where v_m denotes the molar volume and the subscripts "P" and "TMD" indicates that the derivatives are calculated at constant pressure along the TMD locus. Equation 1.11 reports how the temperature dependence of κ_T is related with the slope of the TMD line in the (P,T) plane. Along the TMD line, since $\partial^2 v_m/\partial T^2 > 0$, the signs of $(\partial \kappa_T/\partial T)_{P,\text{TMD}}$ and $(\partial P/\partial T)_{\text{TMD}}$ in equation 1.11 are the same. Consequently, if the TMD has negative slope in the (P,T) plane, therefore the isothermal compressibility will increases on cooling. Thus, in an anomalous liquid such as water, the increase of κ_T upon isobaric cooling is inseparably related to the presence of a negatively sloped TMD.

So in the SF scenario, an increase of compressibility in water is only a thermodynamic requirement and not a priori evidence of any singular behavior as confirmed by Sastry et al. [40] with their lattice model simulation. This model may be viewed as a thermodynamic realization of some basic features of the percolation model of Stanley and Teixeira [69], which indeed predicts the presence of compressibility maxima at low temperatures, i.e., no thermodynamic singularities.

Furthermore, the model explains all the water anomalies in the same way. For example, the coefficient of thermal expansion α_P is related to κ_T by the equation:

$$\left(\frac{\partial \kappa_T}{\partial T}\right)_P = -\left(\frac{\partial \alpha_P}{\partial P}\right)_T \tag{1.12}$$

indicating that it increases in magnitude (having a negative sign) on increasing pressure but remains finite, without displaying any singularities. Equation 1.12 further suggests that the locus of extrema of κ_T with respect to T along isobars coincides with the locus of extrema of α_P with respect to P along isotherms [68]. In particular, Sastry et al. [40] reveal that, on lowering the temperature, liquid water structure equilibrium passes continuously from HDS to LDS (or from High Density Liquid (HDL) to Low density Liquid (LDL)). On the other hand, their model yields two first-order phase transitions. In the low-temperature transition, the phase with higher density also has higher entropy, and hence the transition line has negative slope in the (P,T) plane [70]. This leads to the last scenario that will be presented in the next section.

Second critical point and liquid-liquid transition

The second critical point interpretation was formulated in 1992 by Poole et al. [70]. It ascribes the anomalous properties of supercooled water to the presence of a metastable, low-temperature liquid-liquid critical point (LLCP), already mentioned in figure 1.4 and indicated with C' in figure 1.9c, that is associated with a liquid-liquid phase transition (LLPT) between low-density liquid (LDL) and high-density liquid (HDL) phases.

This hypothesis indeed furnishes a thermodynamically consistent perspective on the global phase behavior of metastable water linking the anomalies of supercooled water to the observed first order transition between LDA and HDA that terminates at the second critical point above which the two metastable forms of amorphous water become indistinguishable [70]. It is well known that in proximity of a critical point, fluctuations between two closing phases are more accentuated. These enhanced fluctuations influence the properties of liquid water leading to anomalous behavior. Therefore, the already mentioned experimentally observed sharp increases in liquid water response functions upon cooling are the macroscopic manifestation of the increased fluctuations (equations 1.2, 1.4 and 1.7) associated with this critical point. In particular, in this interpretation, the transition between a denser, disordered phase and a less dense but more structured phase involves discontinuities of volume and entropy: it is a first-order phase transition. Because the high-density phase is also the one with the largest entropy, the phase transition locus is characterized by a negative slope in the (P,T) plane, and the critical point associated with this transition corresponds to the temperature above which (and, unusually, the pressure below which) is impossible to distinguish the coexisting phases (figure 1.4).

MD simulations were very useful to follow and understand the metastable phases of liquid water and many potentials have been developed and used to reproduce and understand water properties. In 1974 Stillinger and Rahman, using ST2 potential for water, were able to emulate water pair correlation and intermediate scattering functions obtained experimentally [71]. In the 90's, Poole et al. performed several works on this topics using both ST2 and TIP4P potentials for water [67, 70]. According to ST2 model, the LDA phase possesses sharp inflections in which the volume changes abruptly, suggesting the existence of a first-order phase transition between two amorphous solid forms [70]. Furthermore, the response functions of water investigated with the ST2 model increase in the supercooled region in qualitative agreement with experimental observations. The use of TIP4P potential for water furnishes similar results, but adding a contradiction with the stability limit conjecture [67, 72]. In fact, studying the behavior of the liquid spinodal and its relationship to the TMD, Poole et al. found that the TMD retraces towards lower

temperatures at negative pressure, and does not intersect the spinodal. So their calculated spinodal shows a monotonic positive slope in the (P,T) plane and does not retrace towards positive pressure, in contrast with the SLC scenario. Anyway, because of the substantial numerical uncertainties associated with finite-size effects which affect computational studies, the location of the second critical point is different depending on the model used. In fact, the ST2 model predicts that this occurs at approximately 235 K and 2 kbar [73], whereas the TIP5P model predicts it at approximately 218 K and 3.2 kbar [74].

Mishima and Stanley [75] gave the first important experimental support to the second critical point scenario. In particular, they have studied water droplets with diameters of the order of 1-10 μm at high pressures. In such small volumes, nucleation of secondary ice phases following melting in the supercooled regime is kinetically suppressed. So they measured the melting curve of metastable ice IV discovering that this locus experiences a sharp change of slope in the region where it would intersect the presumed line of first-order liquid-liquid phase transitions. It was just this sudden change in the melting curve slope to be attributed to a change in nature of the liquid phase into which the solid melts. This concept is expressed by the Clausius-Clapeyron equation:

$$\frac{dP}{dT} = \frac{\Delta s_m}{\Delta v_m} \tag{1.13}$$

in which dP/dT indicates the slope of the melting curve in the (P,T) plane, and Δv_m and Δs_m denote the difference in volume and molar entropy, respectively, between the coexisting liquid and solid phases. Furthermore, Mishima and Stanley predicted a low-temperature critical point at approximately 220 K and 1 kbar for supercooled water [75] (figure 1.9c). However, because of the proximity between homogeneous nucleation locus and the first-order transition line, these experiments did not completely clarify the situation.

In the past years, new light was shed on this hot topic. Following the idea of confining water, Chen et al. [53, 76, 77] have studied the dynamics of water contained in laboratory synthesized nanoporous silica matrices MCM-41-S with pore diameters of 18 and 14 Å. In this frame, crystallization can be avoided and water can be studied in its liquid state well below 235 K (T_H). In their work, they interpreted the sharp change in the thermal behavior of the average translational relaxation time at $T = 225$ K as the predicted fragile-to-strong liquid-liquid transition. Furthermore, Liu et al. [76] showed that the L-L transition temperature decreases steadily with an increasing pressure, until it intersects the T_H line of bulk water at a pressure of 1600 bar. Above this value of pressure, it is no longer possible to distinguish the characteristic feature of the FST. This end point seems to coincide just with the hypothesized second critical point (figures 1.4 and 1.9c). In the (P,T) plane showed in 1.4, the continuation of L-L transition locus at pressure lower than that of the critical point is called *Widom line* and coincides with the locus of specific heat maxima, being a critical isochore. Xu et al. [78], by means of MD simulations, found a correlation between the F-S dynamic crossover and the Widom line. In particular, as stated by the Adams-Gibbs theory [79], they evidenced a possible thermodynamic-dynamic relation, in this case between the LLPT and the fragile-to-strong dynamical transition. In particular, this correlation is given by the temperature $T \simeq 225$ K that is called T_L and represents both the temperature of the FST and the Widom line temperature (T_W). Recently, Xu et al. [80] review the recent experimental and theoretical progresses on the study of the LLPT in water.

1.2 Water interacting with other systems

As already stated in 1.1, water has some unusual and important physical and chemical properties, playing a very essential role as a solvent and sustaining the biochemistry of life [1–5, 14]. In fact, over the past three decades, water is not longer considered only as a simply "life's solvent", but indeed as a "matrix of life" that actively interacts with biomolecules. Water may be considered as a biomolecule in the sense that aggregates of H_2O molecules accomplish delicate biochemical tasks in their interaction with biosystems.

Water is called the "universal solvent"[14] because more substances can be dissolved in water than in any other chemical. In fact, much of life's chemistry takes place in aqueous solutions, or solutions with water as the solvent. Anyway, the attribute "universal" is not entirely accurate, since there are some substances (such as oils) that do not dissolve well in water. Water's behavior as a solvent depends on its polarity and the response of its hydrogen-bonded network to the presence of an intruding solute particle [1].

H_2O is an extremely "good solvent" for ions allowing their dissociation in salts and greatly bond to other polar substances (e.g., alcohols). In particular, this is a result of water's polarity and high dielectric constant, which enables it to screen the Coulombic potential of ions. In the same way, water is an efficient solvent for biomolecular poly-electrolytes such as proteins [1]. As a polar species, water is good at dissolving polar molecules engaging in favorable Coulombic interactions with ions and other polar solutes. On the contrary, is a "bad solvent" for non-polar molecules. In fact, non-polar molecules stay together in water because the strong attractive forces that water molecules generate between each other are more intense than the Van der Waals interactions with non-polar molecules. When a polar compound is inserted in aqueous solution, it is surrounded by small sized water molecules that constitute an interface called hydration shell.

In this frame, two different types of substances can be distinguished: (i) hydrophilic ("water-loving") polar substances that will mix well and dissolve in water, and (ii) hydrophobic ("water-fearing") non-polar substances, that do not mix well in H_2O.

These non-polar molecules are called hydrophobes and usually have a long chain of carbons that do not interact with water. This tendency of water to exclude hydrophobes is named "hydrophobic effect" [81, 82]. In fact, when a hydrophobe is dropped in water, higly dynamic HBs between liquid water molecules will be broken to make room for the hydrophobe. So, hydrophobic solutes in water experience a force that causes them to aggregate. It seems clear that this hydrophobic interaction is in some way responsible for several important biological processes [83], e.g., the folding of proteins. In addition to proteins, there are many other biological substances that rely on hydrophobic interactions for its survival and functions, like the aggregation of phospholipids into bilayer membranes in every cell of human body. Particularly interesting is the case of the interaction of water and amphiphiles, such as methanol.

Here, the role of biological water in its interaction with several biosystems will be highlighted.

1.2.1 Water-methanol solutions

Small amphiphiles in solution with water can be used as "model systems" to analyze water HB interactions and the consequent HB networks [84]. Amphiphilic or amphipathic molecules can be considered approximately as linear molecules constituted by a hydrophobic terminal groups and a hydrophilic head. When such "surfactant" molecules

---

[14]A solvent is a substance that can dissolve other molecules and compounds, which are known as solutes. A homogeneous mixture of solvent and solute is called a solution.

are dispersed in a liquid (e.g,. water), the competition between hydrophobicity and hydrophilicity generates a reduction in the entropy of the system. This decrease gives rise to the formation of an aggregate (called "micelle") in which the hydrophilic regions are in contact with surrounding solvent, isolating the hydrophobic single-tail area in the micelle centre [1, 85, 86]. When water is mixed with these systems, the competition of structures that, depending on variables such as temperature and concentration, assume different geometric forms (spheres, ellipsoids, cylinders, layers and bilayers).

The simplest amphiphilic molecule is methanol (also known as "methyl alcohol") that consists of a single hydrophobic methyl (CH_3) group and a single hydrophilic hydroxyl (OH) group: so, it is molecular formula is CH_3OH (often abbreviated MeOH). In this alcohol, the carbon atom is at the center of a more or less regular tetrahedron whose vertices are occupied by the oxygen atom and three hydrogen atoms directly linked to the carbon atom (figure 1.10a).

At room temperature, methanol is a polar liquid, and appears colorless with a characteristic odor. It is very volatile and extremely flammable.

Methanol has one donor and one (or two) acceptor sites owing to one of the donor sites in the methanol molecule is replaced by a hydrophobic group (methyl), so, in its liquid state, this alcohol has both one-dimensional (chains) and two-dimensional (rings) HB networks [87, 88].

This is the most salient feature of methanol, that is the fact that despite CH_3OH molecules are held together by HBs, it does not show those anomalous behaviors that characterize water both for its thermodynamics and dynamics. For example, the density of methanol [37] varies almost linearly, and in any case monotonously decreases with the temperature without any maximum, as happens for water (see 1.1.4, figure 1.5).

Unlike water, that is considered a prototype glass-forming material, methanol can be thought as a strong liquid and it exhibits an Arrhenius behavior (see equation 1.8) in the temperature range $160 < T < 335$ K, with $T_M = 175$ K and $T_g = 100$ K.

Although the structure of the individual components is relatively simple, the behavior of the water-methanol solution is more complicated from those found in simple molecules and the thermodynamic and transport properties are anomalous [89]. For example, diffusion coefficient, compressibility, and excess entropy are significantly smaller and the viscosity profile becomes nonlinear when the mixing ratio is altered.

In 1935, Gibson [90] measured the specific volume (υ) and the compressibility (κ_T) of methanol in aqueous solutions for different molar fractions[15] of methanol (X_{MeOH}) at a temperature of 298 K and at atmospheric pressure. In his work, in particular, he showed that the κ_T coefficient of the mixture present a minimum at $X_{MeOH} = 0.1$ and that the partial volume of water in diluted solutions is greater than the specific volume of pure water. On the basis of his measurements, Gibson suggested that the presence of methanol promote the connection of water molecules, contrary to other types of solute.

In 1945, refferring to the interaction between water and hydrophobes, Frank and Evans [89] suggested that the structure of normal water is significantly enhanced by hydrophobic forces that increase the local order near the methyl headgroup (the "hydrophobic hydration" theory). In this way, the H_2O molecules arrange themselves to increase the local order around the solute particle giving rise to an "iceberg-like" configuration: the hydrophobe is encased in an ice-like solvation shell of water. At hydrophobic sites, water also loses HBs and its enthalpy increases. To compensate for the enthalpy unbalance, the local HB arrangement of water molecules expands to form low-density

---

[15]The molar fraction is used to express the concentration of a chemical species in a homogeneous mixture. It is defined as the ratio of the number of moles of the reference species and the number of moles of all species present in the mixture, $X_i = n_i/n_{tot}$

water clusters with lower entropy. Instead, Kauzmann, in his "entropic" origin of the hydrophobic interaction [91], showed that the formation of such iceberg-like structure leads to an entropy decrease due to the compromised rotational and translational freedom of the molecules in the hydration sphere. Anyway, there is an entropy increase when two "caged" hydrophobes were closed together . Thus, there is an entropically based force of attraction between these solute particles.

In 1961, Mikhail and Kimel [92] performed experiments on the water-methanol solution measuring the density ρ and viscosity η in function of X_{MeOH} for temperatures between 298 K and 323 K. From these measurements it is apparent that η has a maximum at $X_{\mathrm{MeOH}} = 0.28$ above the ambient temperature. On the contrary, the density maintains a linear behavior with the variation of the methanol concentration throughout the temperature range considered.

The values of viscosity found by Mikhail and Kimel coincided with those subsequently measured by Schott [93] in a study aimed at analyzing the hydration of primary alcohols and aggregation phenomena in a liquid binary system. To do this, he focused his attention on the behavior of the fluidity ϕ (the reciprocal of the viscosity) of the system. In particular, the difference ($\Delta\phi$) between the experimental fluidity and the calculated one for the methanol-water system shows a maximum that becomes more defined with increasing the temperature (as shown in figure 1.11a). Since, in the presence of aggregation phenomena, the measured fluidity is smaller than the calculated one, Schott interpreted the presence of this maximum in terms of a more pronounced aggregation at the highest temperatures. This is possible if we consider that in the water-methanol system there are three types of aggregating phenomena that compete with each other and involve different types of interaction: methanol-methanol, water-water and water-methanol. Since the first two interactions mentioned decrease with increasing the temperature, this competition apparently results in a greater water-methanol aggregation at higher T.

In 1985, Derlacki et al. [94] measured the methanol-water diffusion coefficients throughout the whole concentration range at 278 K and 298 K, and atmospheric pressure. Starting from pure water, as the concentration of methanol increases, the water and methanol diffusion coefficients show a miminum at a methanol molar fraction of 0.25 (for MeOH) and 0.33 (for H_2O). Starting from these concentrations, continuing adding methanol, the diffusion coefficients begin to increase, although for water there is a lower growth rate than that of methanol. In the same year, Woolf [95] noted that the diffusion coefficient of the water-methanol mixture is strongly dependent on the pressure at varying concentrations at temperatures below 298 K. In particular, at 278 K, Woolf noted that an increase in pressure greatly improved the freedom of movement of the methanol molecules. From this Woolf deduced that the aggregation between water and methanol molecules is not as strong as that between the only water molecules and consequently a structure distortion, as a result of an increase in pressure, has an effect more pronounced on water-methanol interactions.

In the same years, Easteal and Woolf [96] measured some properties of the water-methanol solution at different concentrations in a temperature range of $278.15 < T < 323.15$ K up to a pressure of 280 MPa. In particular, they investigated the excess of thermodynamic properties [97] finding that the molar excess of entropy is negative through the concentration range and has a minimum at $X_{\mathrm{MeOH}} = 0.25$ and $X_{\mathrm{MeOH}} = 0.35$. An increase in pressure, temperature or molar fraction of methanol (above $X_{\mathrm{MeOH}} = 0.35$) increases the molar excess of entropy. Based on these results, Easteal and Woolf proposed that at low temperatures and pressures the addition of methanol to water up to a MeOH molar concentration between 0.25 and 0.30 modifies the network of HBs of water by favoring the positioning of the alcohol molecules within the cavities resulting in the formation of hydrogen bonds between water and methanol.

In 1993 Soper and Finney [98] performed neutron diffraction (ND) measurements of the water-methanol mixture with a MeOH molar fraction of 0.1. The analysis of the results confirmed the existence of a well-defined shell of hydration of water molecules at a distance of ~ 3.7 Å from the carbon atom present in the methanol molecule. The H_2O molecules in this shell form a disordered cage even maintaining the local tetrahedric structure they possess in pure water. In this shell, they also observed a weak polarization of the water molecules around methanol. Soper and Finney stated that their measurements represent the first experimental evidence that water molecules form a disordered cage of HBs around the methanol molecule. Apparently, such a cage may form without a high degree of hydrogen bonding between the water molecules.

In 1996, Micali et al. [99] studied the dynamics of water in the water-methanol mixture by means of Depolarized Rayleigh Light Scattering (DRLS), considering several concentration and temperature and obtaining important information about the behavior of water around the methanol molecules. The DRLS spectra obtained for water-methanol solutions, like the pure water case, have two contributions, one fast and one slow, modeled by two Lorentzians. In particular, the fast contribution has a near zero dependence, while the slow contribution, attributed to the rotational motions of water molecules and, more precisely, to the HBs [100], has a strong dependence on temperature. The corresponding relaxation time shows an Arrhenius T dependence with an activation energy that corresponds to that of the HB [101]. Two fundamental results emerge from their analysis. The first one is the presence of a maximum for all temperatures at the same molar fraction of methanol $X_{MeOH} = 0.4$, that is the same concentration where the anomalous behavior of thermodynamic properties is observed [91, 102, 103]. In particular, a marked slowing down of the relaxation time is noticed in the same range of concentrations where the minimum of the diffusion coefficient is observed. The second result evidences a strong dependence on temperature of the relaxation time in the water-methanol solution that is evident for all methanol concentrations within the experimental error, while pure methanol behavior is virtually independent of temperature. In accordance with Finney and Soper's neutron diffraction experiments [98] and with MD simulations [103], according to which the dynamic slowing down above is entirely due to the lifetime of HBs that involves water-water interactions, the results obtained from Micali et al. highlighted the presence, in water-rich solutions, of well-defined hydration shells around methanol molecules that include a finite number of water molecules. In addition, the authors observed that dynamic properties of the system within a shell are related to the lifetime of water-water HBs. At the investigated concentrations, the lifetime of the hydrogen bond is longer than those in pure water at the same temperature, which is indicative of greater structural stability of the water. Therefore, the authors stressed the fundamental role played by HB dynamics, suggesting a dynamic origin rather than a structural one for thermodynamic anomalies observed for the methanol-water mixture.

In 2000, Dixit et al. [104] studied the water-methanol mixture by high resolution Raman spectroscopy over the entire composition range and suggested a global image of the progressive hydration of the methanol molecules: water first breaks down the molecular chains of pure methanol, and after completely hydrate the hydroxyl groups before solving the methyl groups. In particular, for a molar fraction of methanol X_{MeOH} between 1 and 0.7, water molecules leave the pure methane chain structure substantially intact. Hydration takes place at the end of the chain where the methanol molecules act primarily as HB receptors.

In 2002, Dixit et al. [105] used ND experiments with isotopic substitution to investigate the molecular-scale structure of the water-methanol solution with a $X_{MeOH} = 0.7$. Their diffraction data were interpreted by "empirical potential structure refinement" (EPSR) and authors derived the point-to-point radial distribution functions that were

compared with those previously obtained for pure water [106] and pure methanol [107]. From this comparison, they examined how the local order of the methanol molecules is modified by the addition of small amounts of water. In particular, they noted that the increasing of the water content induces an aggregation of methyl groups and a simultaneous removal of the hydroxyl groups of methanol. In addition, by comparing the oxygen-oxygen radial distribution function for pure water and for a concentrated methanol-water solution, the authors observed that the second peak, centered at about 4.5 Å and generally interpreted as evidence of a tetrahedral structure of Water, is virtually unchanged to confirm that the water structure within the concentrated blend remains mostly unaltered (see figure 3 of [105]). In contrast, in the diluted regime, a slight shift of this second peak was interpreted as the presence of a slight compression on the structure of the water made by the methanol molecules. Furthermore, since the number of HBs per molecule in the solution is equal to that in the pure liquids before being mixed, the authors suggested that the value and the sign of the excess enthalpy of the mixture are determined by the continuous formation and breaking of several HBs for alcohol-alcohol, water-alcohol and water-water interactions. Polar water interaction with the hydroxyl alcohol groups influences the thermodynamic properties of the water-methanol mixture more than a structural reorganization induced by the methyl groups.
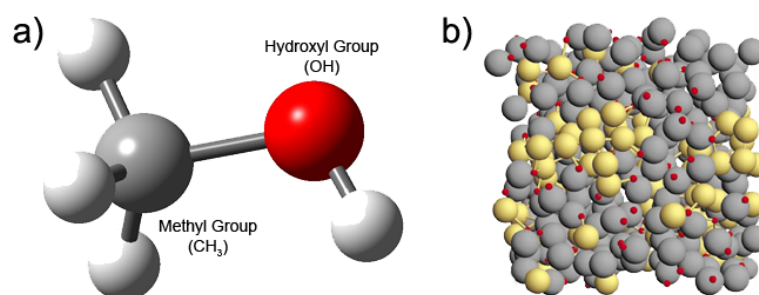

FIGURE 1.10: The methanol molecule is shown in its ball-and-stick model. The hydrogen, the carbon and the oxygen atoms are represented as light grey, dark grey and red spheres, respectively. The simulated water-methanol system is reported in (b). Here, methyl groups are shown as grey balls instead large yellow spheres have been used to highlight the positions of water molecules and small red spheres denote methanol oxygen atoms. Figure adapted from [105].

Finney et al. [108] proposed that the clustering of small hydrophobes might have a more subtle entropic origin referring to the "debate" between Frank and Evans [89] and Kauzmann theories of hydrophobic interaction [91]. They find that the hydration shells of water molecules are slightly altered by the presence of methanol. There is a reduction of the entropy that leads to a small decrease in freedom of the water molecules promoting the aggregation of the methanol molecules. In any event, these direct structural probes seem to have diminished any argument for the classic Kauzmann model [91] of the hydrophobic interaction.

By means of X-ray absorption and selective excitation X-ray spectroscopy, Guo et al. [109] found that molecules in pure methanol form linear chains and rings, each of which consists of 6 or 8 elements held together by HBs between the hydroxyl groups. The results of Guo et al. show that most of the water and methanol molecules present in the mixture persist in structures similar to those of pure liquids. The anomalous increase in entropy observed in the water-methanol mixture is indeed related to an incomplete mixing at the molecular level.

In 2004, Dougan et al. [110] investigated on changes in cluster behavior based on concentration and the limit to which MD simulations coincided with experimental observations to provide additional understanding of cluster dynamics. A series of neutron diffraction experiments analyzed using the EPSR method, along with MD simulations, showed that water-methanol mixtures exhibit extended structure in solution despite the components being totally miscible in all proportions. The region of interest with particular interest was that in which $0.27 < X_{\mathrm{MeOH}} < 0.54$. In this region, both methanol and water form separate networks and many transport properties and excesses of thermodynamic functions reach extreme values. For $X_{\mathrm{MeOH}} = 0.54$, the methanol clusters do not tend to form chains held together by HBs as happen in the case when only pure liquid is considered. On the contrary, methyl groups tend to come closer and the hydroxyl groups bind themselves to the water molecules forming the major boundaries between the regions rich in methanol and water-rich areas. This is what happens in systems driven by hydrophobic interactions and that has been observed mainly using diffraction experiments [111, 112]. According to MD simulations, the size of methanol clusters in solution is much lower than the size of the HBs network in the pure liquid and this can be considered as an index of the significant breakdown of the hydrogen bonds network of methanol. In particular, this situation is due to the fact that H_2O molecules obstruct the formation of extended methanol clusters. In the low methanol concentration range, its molecules seem to exert a compression on the water structure. On the contrary, in the limit of high methanol concentration, the system segregates in molecular-scale microemulsions [112] with the methyl groups pushed to each other and the hydroxyl groups surrounding small clusters of water. Dougan et al. ascribed the approximate concentration below which water aggregates (percolation of clusters) to the molar fraction of $X_{\mathrm{MeOH}} = 0.27$, differently from the behavior of methanol that is isolated in small clusters. In the concentration range $0.27 < X_{\mathrm{MeOH}} < 0.54$, both the clusters of water and methanol perform the percolation at the same time. $X_{\mathrm{MeOH}} > 0.54$, there is the percolation of only the methanol clusters, while the clusters of water become smaller and isolated. Indeed, they found a high heterogeneity of the water-methanol mixture over the entire concentration range despite the apparent miscibility of both components in all proportions.

In 2005, Allison et al. [113] observes clustering and immiscibility phenomena of the water-methanol mixture on microscopic-scale using theoretic simulations. In particular, they showed the agreement between ND diffraction experiments [110] and their MD simulations utilizing the same description of intermolecular interactions for methanol and water.

Soper et al. [114] studied the excess entropy and its concentration dependence in water-alcohol solutions. The authors explained quantitatively this excess negative entropy as a consequence of the tendency of water and alcohol to segregate at the molecular level. They proposed that the cause of the excess entropy is structural in origin as stated in Frank and Evans theory [89], but there is no need to invoke the iceberg-like water structure to explain it.

In 2008, Corsaro et al. [115] measured, using ^{1}H NMR technique, the spin-lattice, T_1, and spin-spin, T_2, relaxation times of the three functional groups in water-methanol solutions at $X_{\mathrm{MeOH}} = 0, 0.04, 0.1, 0.24, 0.5, 1$ in the range $205\,\mathrm{K} < T < 295\,\mathrm{K}$. The measured relaxation times in the mixtures are faster than those of pure water and methanol for all the X_{MeOH} considered because of strong interactions resulting in a complex hydrogen bonding dynamics that regulate the thermodynamic properties of the solution. In particular, HBs are constantly broken and formed between hydroxyl groups in solution; their lifetime and stability depend on both concentration and temperature. In this frame, they observe how the interplay between hydrophobicity and hydrophilicity changes with temperature too. A comparable trend in temperature of the measured relaxation times

of each functional group at every concentration is noticed and exhibits some peculiarities at a specific temperature, $T_k = 245$ K. These results agree with the fact that, above this temperature, HB formation takes place among several hydroxyl groups in solution, granting the development of local water-methanol clusters, whereas, below T_k, HBs are established rather among hydroxyl groups of the same species. These results confirm that there are stable water-methanol clusters at high T due to hydrophobicity, and that at low temperatures, the tetrabonded water clusters strongly influence the properties of the mixture. Later, Corsaro et al. [116] have continued the study of the dynamical and structural properties of water/methanol solutions by means of High-Resolution NMR investigating dynamical quantities and structurally dependent quantities. In particular, they studied separately all the hydrogens belonging to the different functional groups and they stated that the physical properties of the solution are influenced by the interplay between hydrophobic and hydrophilic interactions that in turn depend on the solution concentration and on the temperature (see figure 1.11b).
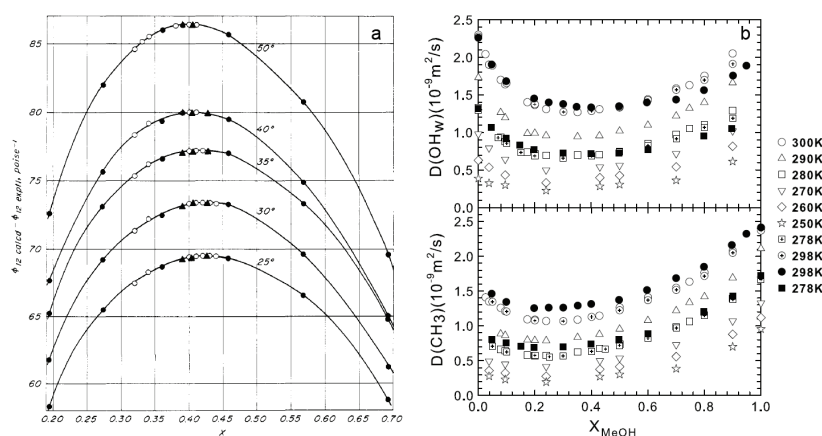

FIGURE 1.11: The figure shows some peculiar properties of the water-methanol solution. In the left side (a), the differences between experimental and calculated fluidities in the water-methanol system are reported. The black and empty circles indicated the values obtained from measurements and calculated by equation 8 of Mikhail and Kimel work [92], respectively. Instead, full triangles reported the Schott's data [93]. In the right side of the figure (b), the self-diffusion coefficient D of the water–methanol mixture for the OH_w (upper panel) and CH_3 (lower panel) functional groups are plotted vs the methanol molar fraction, X_{MeOH} for $250 < T < 300$ K (see [116]). Note that the pointed centered symbols refer to tracer diffusion [94], whereas the full black symbols refer to simulation results [117]. Figure adapted from [93] and [116].

Generally, it is well evident that the interaction between water and methanol is strong [92, 94, 114–116, 118], but there is no clear explanation about the surprising characteristic of this solution, although scattering experiments have revealed 3D HB networks formed by hydrophilic and hydrophobic interactions between water and methanol molecules. In fact, Nagasaka et al. [119] found three local structures around the methyl group at ambient temperature (298 K) using water molar fraction X_W, combining soft X-ray absorption spectroscopy (XAS) experiments combined with a MD simulation. In particular, in the region rich of methanol molecules ($0 < X_W < 0.3$), they detected a small number of H_2O molecules around the dominant 1D/2D HB methanol cluster networks. The mixed methanol-water 3D network structures increase in the intermediate region ($0.3 < X_W < 0.7$) and it makes the hydrophobic interaction of the methyl

group dominant. In the water-rich region ($0.7 < X_W < 0.95$), the methanol molecules are set separately inside dominant 3D HB water networks. At low methanol concentration, methanol molecules exert a slight compressive effect on the water structure. At high methanol concentration, the methyl groups are pushed together and the methanol hydroxyl groups collect around small water clusters [114]. Below specific concentration conditions, these clusters seem to expand their size and percolate, although their structures break and rapidly reform. This indicates that the origin of the behavior of water-methanol solutions is dynamical.

As can be seen from the already discussed studies carried out on the water-methanol mixture, the experimental results obtained so far are not sufficient to describe an exhaustive and coherent picture of the dynamic and structural properties of the water-methanol mixture and their behavior at varying temperatures and concentrations. So, in this thesis, the dynamical properties of water-alcohol mixtures at low temperatures were investigated by means of Nuclear Magnetic Resonance (NMR) spectroscopy. In fact, this technique allows to discriminate and follow the dynamics of the individual molecular group of the molecules within the system. In particular, we study the relaxation times t_α [84] evaluating how the transport parameters of the solution differ from those in an ideal mixture in which there are no interacting molecules.

1.2.2 Water and protein interaction: the case of lysozyme

The role of water assumes particular importance in its interaction with proteins.

Proteins are macromolecules with a wide variety of biologically important functions consisting of one or more long chains of 20 different types of amino acid [120]. The length of such sequences varies from about 40 to 1000 and more amino acids. The amino acids are constituted by a peptide group and a residue R (side chain). The covalent bonds between the peptide groups form the backbone of the protein. The rotational degrees of freedom of peptide bonds make the backbone very flexible and for this reason a protein can be imagined as a heteropolymer. From an "unsophisticated" point of view, amino acids can be distinguished in hydrophobic and hydrophilic. Hydrophobic amino acids usually lie in the native state of the body (that is not exposed to water) forming the "heart" of the protein. In contrast, hydrophilic amino acids are in contact with water and are usually found on the surface of the protein. This classification is considered rough because, generally, the amino acids are amphiphilic molecules. The native structure of a protein is determined by the delicate balance between intra and intermolecular interactions among (i) different residues and (ii) these ones and the water molecules surrounding them. In proteins, we recognize up to four levels of structure [120]: (i) the primary structure that corresponds to the specific sequence of the amino acids of the backbone; (ii) the secondary structure comprehends several amino acids that often form ordered geometric structures located in particular parts of the protein (among that secondary structure motifs, we recognize α-helices and β-sheets)[16]; (iii) the tertiary structure constitutes the true 3D configuration of the protein and corresponds to the structure occupied by the protein when it is in the so-called native state; (iv) the quaternary structure of proteins often consists of several subunits essentially equal to each other.

---

[16]In α-helices, the protein backbone forms a regular spiral (e.g., right-handed). The formation of an helix is accompanied by the formation of HBs between the nitrogen and oxygen atoms of the different peptide groups. These bonds form a network that supports and stabilizes the α-helix itself. In the β-sheets, instead, different sections of the polypeptide chain are adjacent to each other to form almost planar structures. Again, formation of β-sheets is accompanied and stabilized by the formation of hydrogen bonds between hydrogen and oxygen.

Proteins are highly complex systems and they can "fold" in different ways (*folding* process) because of their characteristic structural disorder. This is reflected in the existence of several conformational constituents (CS) whose number depends on the temperature and the chemical-physical characteristics of the solvent (especially water) in which proteins are found. In protein folding, water mediates the collapse of the chain [121] and, in particular, it is believed that the conformational motion is coupled with the dynamics of the hydration water [122]. The folding process of proteins depends on the incompatibility between low-density water and the hydrophobic surface that folds to form a hydrophobic core. This competition between hydrophobic groups that remove water (cluster) structures from the surface of the protein is controlled by the interactions among charged groups and polar ones and each of them with water molecules.

When a protein is in aqueous solution, it is possible to identify three different type of solute-water interactions [120]. They are ion hydration (water interacting with charged groups), hydrogen bonding between polar groups and water (also known as hydrophilic hydration), and the already defined hydrophobic hydration, which describes the response of water to chemically inert residues. In such a frame, we can distinguish two different categories of water molecules close to the protein depending on the nature of their hydrogen bonding: the "confined" or "interfacial" water that is attached to some substrates or filling small cavities inside the protein, also defined as "bound" water because this form of water is difficult to remove, and the "free" water that is unrestrained to move around the protein [1, 5, 15]. In particular, interfacial water located on the outer surface of the protein is also called "hydration" water [15]. Therefore, essentially, when a protein is in solution, it is possible to classify two types of H_2O molecule in close proximity to it, (i) internal bound molecules and (ii) hydration water molecules. Protein hydration is very important for determining the corresponding biological activity [7, 15, 123]. Hydration can be considered as a process that consists in the continuous addition of water to the protein in its dry state until a hydration level h, i.e., the grams of H_2O per grams of dry protein, is reached beyond which an additional addition of water does not produce any variation on the essential properties of the protein by contributing only to its dilution [123]. The *first shell of hydration* looks like a single layer coating on the surface of the protein. In this frame, it is important to state that a protein cannot function properly without water, but, indeed, this first hydration shell activates its biological function strictly linked to the residual flexibility driven by water dynamics. So, the protein activity depends on a delicate interplay between its environment and the protein itself. Many proteins use bound water molecules as functional units, e.g., to mediate interactions with substrate molecules or with other proteins [1]. Referring to hydration water, Ebbinghaus et al. [124] observed by means of Terahertz spectroscopy that the structure of water around proteins extends for at least one nanometer from their surface or for 2 nm between neighboring proteins. Surface water molecules (hydration water) are strongly bonded with positive charged amino acids. In particular, the flexibility of the system depends on the surface water exchange that is controlled by the exposure of the protein to water, that is greater exposure means greater flexibility, hence a wider chain protein movement [125].

In the frame of the dynamics of water-protein systems, HB interactions drive the structure, stability, and functioning of biological macromolecules [4]. In fact, the physical and chemical properties of proteins depend on the attribute of HBs formed between the protein residuals and its hydration water.

In particular, Oleinikova et al. [126, 127] showed that the biological activity of proteins depends on the formation of a 2D network of HBs that is extended to most of the surface of a protein and combines all clusters of surface water molecules. This water

network is capable to convey information around the protein and to control its dynamics [128]. Many vital activities, however, recover well at about 310 K. As stated by Brovchenko et al. [129], at this temperature, the two-dimensional hydrogen bond network is almost ready to break for any further temperature increase.

The molecular motions within the protein, essential for its biological activity, are highly dependent on the plasticity which is determined by the hydration level [130]. Thus, internal water allows protein folding and is only expelled from the hydrophobic core by cooperative interactions between the chains of the protein itself [131].

When the peptidic filaments fold, the hydrophobic side chains tend to group within the protein leaving the hydrophilic polar and ionized side chains in contact with the solvent on the external surface. So, minimizing the number of hydrophobic side chains exposed to water is the principal driving force behind the folding process. However, many water molecules remain trapped inside the protein, forming an important structural adhesive held together by HBs. In fact, the HB strength (the hydrophilicity) governs the secondary structure and folding specificity [132] of the biomolecule. The role of temperature is extremely important in determining the local density of surface water structures: high-density aqueous structures give greater flexibility to the biosystem than the low-density aqueous structures that make it more rigid. The first layer of hydration water (the already cited "first hydration shell") around a protein (equivalent to about 0.3 grams of water per gram of protein) is ordered and the hydrogen bonds that hold the water molecules forming this layer on the surface of the protein are stronger and have a longer lifetime than those of free water [133]. Rowe et al. [134] suggest that the first hydration shell is also a 10-20% more dense than free water, which allows to keep the molecules sufficiently separated so that they remain in solution (the solutions are kinetically stable but often thermodynamically unstable). As already mentioned, the existence of the first layer of hydration water is the minimum condition for a protein to perform its biological activity. Without water, the fast conformational fluctuations necessary for the functionality can not occur. Thus, proteins do not exhibit any biological activity when they are not subject to conformational variations, i.e. when they are too rigid and immobile because they are mainly surrounded by low-density water structures. The transition to such a dynamical arrest state was commonly referred to as a "glass transition" of a protein taking place at about 220 K [135]. A similar transition has also been highlighted for protein hydration water at the same temperature. By means of infrared absorption measurements, Doster et al. [122] proposed that this transition can be described by amorphous ice fusion and that the solvent network is composed of water clusters characterized by relatively strong internal bonds. Chen et al. [136] suggested that this dynamic transition in hydration water is the result of a transition from LDL water form at the lowest temperatures to a predominantly HDL form at the highest temperatures. In particular, they stated that this low-T dynamic transition of protein is triggered by a *fragile-to-strong dynamic crossover* (FSDC) at $T_L \approx 220$ K which occurs in hydration water of these biopolymers.

The protein folding corresponds to that complex of phenomena through which the amino acid chain (peptide) comes to assume the native state of the protein. Therefore proteins have very peculiar properties, especially in relation to folding. First of all, in spite of their complexity, real proteins have a well-defined native status and "fold" in it through a fast and secure folding process. This is to say that for real proteins the folding process is generally reversible.

Anyway, not all proteins fold to the best. In fact, there are cases where the folding kinetics may have anomalies. The alteration of a protein's folding characterizes some neurodegenerative illness such as Alzheimer's and Parkinson's diseases, in which conformational variations of proteins (from α-helix or random coil to β-sheets) cause aggregation and, subsequently, formation of insoluble fibrils.

Another important process that characterizes protein is denaturation. The denaturing process occurs when the protein loses its native conformation to return to the state of a simple linear polypeptide chain. Denatured protein naturally also loses its physiological function. Note that protein denaturation may occur because of an increase in temperature or under other stress conditions, such as a strong variation in saline concentration or high concentrations of certain substances (i.e., denaturants) such as urea and SDS (Sodium Dodecyl Sulfate). With the loss of the 3D structure of the protein, hydrophobic amino acids, which are normally within the protein or at the interface with the membranes, are exposed and immersed in a hydrophilic environment. When these hydrophobic residues meet other hydrophobic residues of the same or other molecules, e.g., denatured proteins, they form aggregates. In many cases, denaturation is an irreversible process, however, under certain conditions, it is possible to restore the original structure by a "refolding" process [12, 137].

The importance of the role played by hydration water during both folding and protein denaturation has emerged predominantly after the introduction of the concept of hydrophobicity, linked for the first time by Kauzmann to protein stability [91]. Since then, a protein was simply defined as a peptide + water system because the simple biomolecule is not capable of carrying out its biological activity without at least a minimum hydration shell surrounding it [138]. In particular, the conformational flexibility of a protein (and hence its functionality) is extremely sensitive to the characteristics of HBs with its hydration water. This last experimental evidence is understandable considering that proteins have evolved since the beginning from an aqueous environment.

In particular, we focus our studies on lysozyme, a small globular protein consisting of 129 residues of amino acids (see figure 1.12). It is an antimicrobial enzyme known for its unique ability to degrade the polysaccharide architecture of many kinds of cell walls, normally for the purpose of protection against bacterial infection. Lysozyme, binding to the bacterial surface, reduces the surface of negative electrical charge, making the phagocytosis of the bacterium easier before the opsonines of the immune system intervene. It is abundant in numerous animal tissues and human secretions such as tears and saliva and, in particular, it is also found in high concentrations in egg whites. We converge our experimental investigations on this kind of lysozyme, also known as hen egg-white lysozyme (see figure 1.12).

Its effects were first noticed by Laschtschenko in 1909, but it was officially characterized in 1922 by Alexander Fleming, the Scottish bacteriologist that had discovered penicillin. Fleming recognized lysozyme almost by accident during his research to discover new antibiotic drugs. One day, as he had a strong cold, he incidentally added a drop of his mucus into a bacterial culture and with his astonishment he noticed that the bacteria died: he had discovered one of our natural defenses against infections. Fleming's intent was to find new drugs, but lysozyme is not usable as a medicine because it is too big to move between cells and can only be applied locally. It was also discouraged by the fact that lysozyme had no effect on the most dangerous bacterial types.

The molecule structure was later described by David Chilton Phillips in 1965, which was able to obtain an image with a resolution of 2 Å by means of X-Ray cristallography. His work then led him to explain how the catalytic activity of enzymes can be correlated with their structure. Currently lysozyme is often used as a preservative in the food industry, while in the field of ophthalmology it is used as anti-inflammatory and antibacterial.

The nature of the amino acids present in lysozyme leads to regions of varying hydrophobicities and polarities of the enzyme structure. As already mentioned, whereas the presence of certain regions of hydrophilicity and hydrophobicity is a driving force in determining protein structure when folding, the varying polarities of the side chains
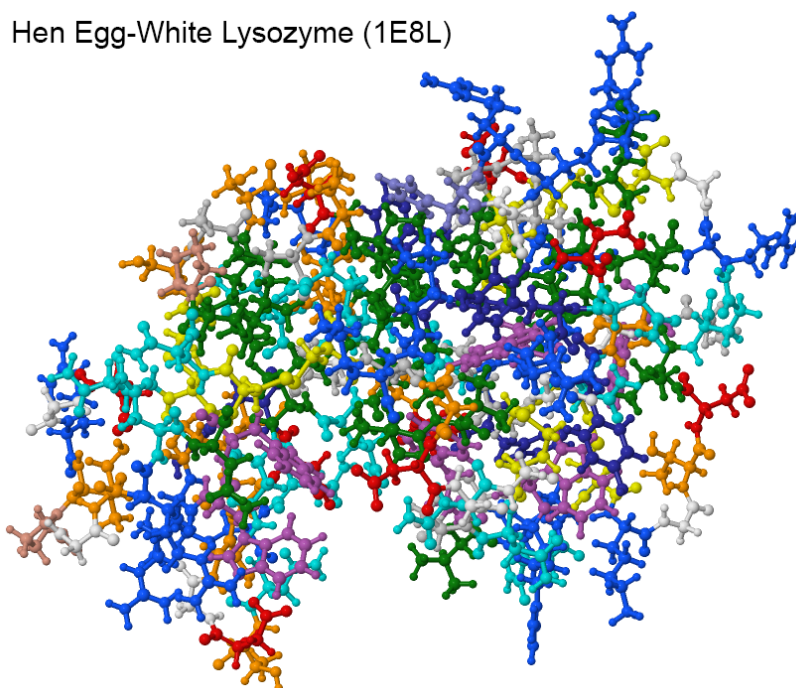
FIGURE 1.12: 1E8L lysozyme macromolecule structure deposited by
Schwalbe et al. in the RCSB Protein Data Bank (PDB) [139].

influence the locations of residues in the enzyme structure. Nonpolar residues will display hydrophobic tendencies occurring mostly on the interior of the enzyme while polar residues will increase in abundance on the surface of the protein in order to increase contact with the aqueous solvent so as to satisfy their hydrophilic nature. The presence of water interacting with the various hydrophilic residues is depicted to further display how polarity affects structure.

Lysozyme has been and still is the subject of several studies using various techniques in different thermodynamical conditions that confirm the importance of water and, in particular, the role of HBs, hydration and temperature in these kinds of systems.

In 1975, Hsi and Bryant [140] performed relaxation NMR experiments for frozen lysozyme solutions. They found that the non-freezing water consisted of two components with different spin-lattice relaxation time[17] values. They were able to quantify the amount of the slower component as 0.06 g, and the amount of the faster component as 0.28 g of water per g of protein (i.e., the hydration level).

Cavatorta et al. [141] studied, by means of Raman spectroscopy, the CH and OH stretching for aqueous solutions of lysozyme at different concentrations, They explained the obtained results in terms of a water model with three water species, each with different Raman intensities: (i) iceberg-like structured water; (2) protein bound water; (3) bulk water.

Few years later, Hilton et al. [142] examined the relaxation of water as a function of temperature in powders of varied hydration level. They suggested that the dependence of the water proton relaxation rates on water content and temperature indicate that H_2O molecule motion on the protein surface becomes slower with decreasing water content and temperature.

---

[17]See paragraph 2.1.2

The dependence of the denaturation process on hydration level has been studied by differential scanning calorimetry for lysozyme by Fujita and Noda [143]. Below an hydration level of 0.3, water molecules are probably bound by HBs to the polar amino acids on the surface of the protein. Above this level, the lysozyme-water interaction was weaker on respect the other case. In particular, between 0.3 and 0.75 h, some water molecules seem interact not only with the water strongly bounded to the protein by HBs, but also with the bulk water.

In 1978, Samanta and Walrafen [144] have repeated and extended the study of Cavatorta et al. [141], but their findings were somewhat different. So, they offered an interpretation involving only a single interaction, hydrogen bonding between lysozyme and water.

Using a drop calorimeter, Yang and Rupley [145] measured the heat capacity isotherm for water-lysozyme system at 25°C. They stated that heat capacity results indicates that, if the configuration changes with the hydration level, the conformation states are distinguishable and thus should be describable, improving the analysis of the solvent-protein interactions. Furthermore, they identified the activation of the enzymatic function of lysozyme at $0.2h$.

Aliotta et al. [146], referring to previous works [141, 144], improved the Raman technique by using isotopic substitution and depolarization. They suggested that lysozyme does not perturb the OH stretching of water.

Furthermore, Poole and Finney [147], by means of IR and Raman spectroscopy, studied the hydration of lysozyme. On the basis of their findings, they proposed that there are configurational changes just below the hydration level for the onset of enzyme activity (i.e., 0.2-0.25h).

Bourret and Parello [148] estimated, from ^{1}H NMR measurements, that 110 water molecules are bound to polar surface sites of lysozyme.

In 1985, Schinkel et al. [149] showed that the rate of hydrogen exchange in powders of lysozyme is the same at 0.2 h as in dilute solution. Hydrogen exchange depends strongly on pH, and the effective pH in protein powders is controlled by ionization of the protein.

It is noteworthy that, in 1991, Rupley and Careri [123] presented a complete summary about protein hydration and function.

In 2002, Salvetti et al. [150] focused their study on the thermodynamics of lysozyme denaturation by measuring the heat capacity c_P of lysozyme-water system in the range $293 < T < 368$ K by means of Differential Scanning Calorimety (DSC)[18] and Temperature Modulated Scanning Calorimetry (TMSC)[19]. As shown in the plot at the top of figure 1.13 that reported two different 12% solution of lysozyme and the 1-heating scan and 2-cooling scan, the heat capacity c'_P, calculated with the TMSC technique and indicated with circled and crossed symbols, displays a peak similar to that observed in the heat capacity data obtained from DSC measurements, $c_{P,DSC}$, shown in the figure as continuous solid line. The authors stated that the peak of $c_{P,DSC}$ at $T \approx 346$ K is attributed to endothermic heat absorption on reversible and irreversible unfolding processes and irreversible thermal denaturation. In particular, they showed that the temperature of the peak and the area under it is not affected by the concentration of lysozyme solution. Furthermore, they found that the thermal denaturation of lysozyme occur according to a scheme, native state ↔ unfolded (intermediate) state → denatured state, in which the first step of

---

[18]The DSC technique furnishes the sum of both the reversible and irreversible contributions in the apparent heat capacity value.

[19]In the TMSC technique, the thermally reversible enthalpy variations are measured separately and simultaneously with the thermally irreversible enthalpy changes.

denaturation of lysozyme is a reversible conformational (unfolding) transition, and the second step is irreversible denaturation.

Mallamace et al. [152] performed NMR measurements and they have demonstrated the existence of two dynamic transitions in protein hydration water. The first transition occurs at $T \approx 220$ K $= T_L$ where the hydration water shows a loss of flexibility of the protein activated by the FSDC introduced by Chen et al. [136]. Above the second transition at about $T \approx 346$ K $= T_D$, where the protein denatures and undergoes towards the folding-unfolding process, the dynamics of hydration water appears dominated by the fraction of water molecules not involved in hydrogen bonds.

In 2008, Sokolov et al. [151] presented an overview of neutron scattering studies of the dynamics in hydrated and dry lysozyme demonstrating that hydration water enhances the activity and dynamics of the protein. Their results suggest that the appearance of a slow relaxation process is the principal reason of the sharp increase of the atomic mean-squared displacements (MSD)[20], shown in the middle part of figure 1.13, that represents a "dynamic transition" taking place in hydrated biomolecules at $T \approx 220$ K.

In the same year, Lagi et al. [153] observed a super-Arrhenius-to-Arrhenius dynamic crossover phenomenon for the protein hydration water both experimentally and by MD simulations in the temperature range of $T = 223 \pm 2$ K. The authors show how the convergence of NMR and Neutron Scattering as well as MD simulations sustains the interpretation that this crossover is a result of the gradual evolution of the structure of hydration water from a HDL to a LDL form upon crossing of the Widom line above the possible LLCP of water (see [136]). Furthermore, when the protein is hydrated, by increasing T, there is an onset at ≈ 220 K from a linear to an anharmonic liquid-like motion in which the MSD sharply increases[21] [154].

Recently, Mallamace et al. [137] performed NMR measurements to analyze the thermal folding of hydrated lysozyme (with hydration level $h = 0.3$). They studied several characteristic properties of the investigated system, such as the inverse of the NMR self-diffusion coefficient D reported in the bottom of figure 1.13 as a function of $1000/T$, by means of proper T changes with heating and cooling cycles that explore the reversible and the irreversible denaturation starting from the protein in its native state. The authors confirmed that water is a "local probe" in the biological and structural changes in the proteins behaviors and, their findings showed that the denaturation process is related to the average number of bonds in which the water molecules are involved.

Finally, Mallamace et al. [155], by means of infrared bending vibrational mode, studied the microscopic mechanisms that are at the base of protein irreversible denaturation. In particular, in that work, it has been stated that the thermal changes of the coupling, by means of the HB, between hydration water molecules and the different chemical groups of the protein are the main microscopic mechanisms underlying the unfolding process. In 2015, the same authors [156] investigated the role that the solvent plays in determining the biological activity of protein by means of Fourier Transform Infrared spectroscopy. In particular, the thermal limit of biological activity characterizing hydrated lysozyme has been observed.

From the arguments made here, it is evident that the role of water and, in particular, the local structure of hydration water is crucial both in triggering biological activity at low temperature and in initiating and regulating the folding/unfolding and possible denaturation of proteins. So, in the next chapters, we will enter into new details about the

---

[20]The mean-squared displacement (also known as mean square displacement, average squared displacement, or mean square fluctuation) is defined as the deviation time between the position of a particle and some reference position. It is a well-known measurement of the spatial length of the random motion, and can be considered as measuring the portion of the system "explored" by the random walker.

[21]Note that this transition is solvent dependent and thus does not occur in dry biomolecules.
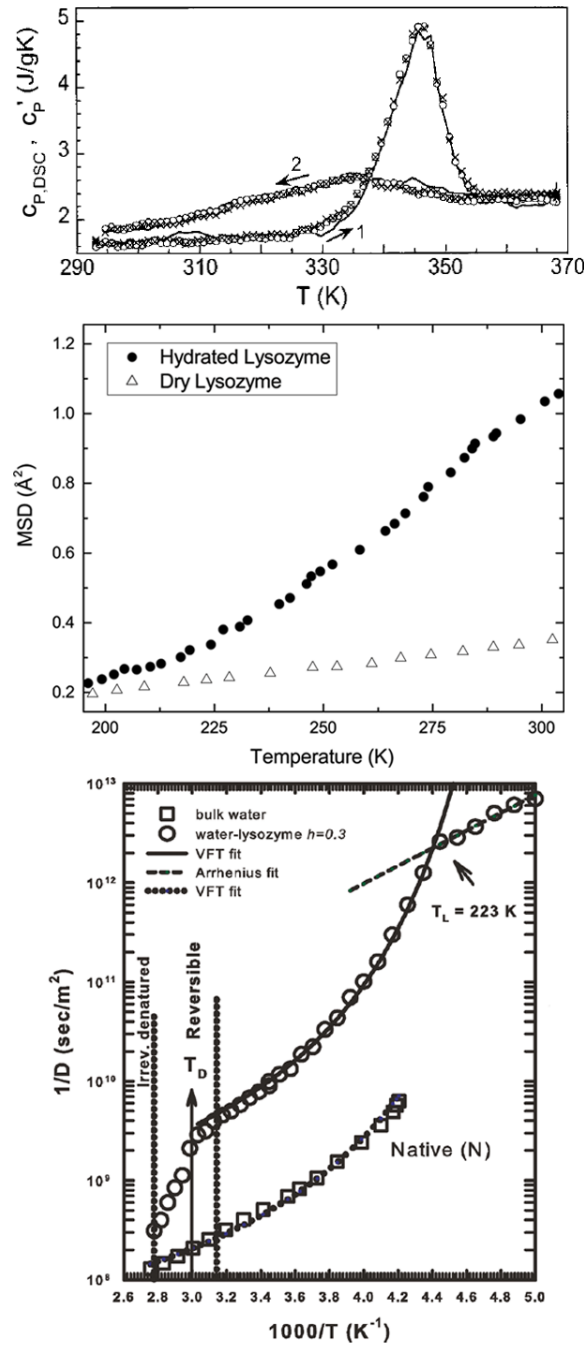
FIGURE 1.13: (Top) The measured c'_P of two distinct 12% lysozyme solutions, one shown by circles and another by crosses, are plotted against T. Data for $c_{P,DSC}$ are displayed by continuous line. Arrows indicate heating (1) or cooling (2) scans of measurements. Figure adapted from [150]. (Middle) Atomic mean-squared displacements (MSD) in dry and wet lysozyme. The rise displayed of hydrated biomolecules at T above 200 K is the dynamic transition. Data taken from [151]. (Bottom) The inverse of the NMR diffusion coefficient D of lysozyme hydration water as a function of 1000/T, for an hydration level of 0.3, compared with that of bulk water. Figure adapted from [137].

fundamental role played by water in the dynamic transitions and in the configurational stability of lysozyme [12, 13, 156–158]. This will be done by means of NMR spectroscopy that, as already mentioned, allows to follow the individual molecular group of the molecules within the system.

Chapter 2

Nuclear Magnetic Resonance

The theory on Nuclear Magnetic Resonance (NMR) has its origin in 1896, when the dutch physicist Pieter Zeeman noticed the splitting of a spectral line of an emitting atom into different components when it is immersed in a magnetic field [159]. Thereafter, the separation of atomic energy levels proportional to an external magnetic field has been recognized as "Zeeman splitting". In 1922, Stern and Gerlach discovered the spin nature of the proton [160] and later, in 1934, Rabi et al. [161] examined the interaction between a magnetic field and the proton spin. Lastly, in December 1945, Purcell et al. [162] detected weak radio-frequency signals generated by the nuclei of atoms. Almost simultaneously, Bloch and coworkers [163] performed a different experiment in which they observed radio signals from the atomic nuclei in water. These two experiments introduced the field we now know as Nuclear Magnetic Resonance. For their discovery of NMR and their theoretical and experimental works, Purcell and Bloch shared the Nobel prize for physics in 1952.

In the early days, NMR was used just to do an accurate measurement of nuclear magnetic moment. However, after the discovery of the chemical shift effect, this technique caused a strong interest in the chemical community [164]. Furthermore, the formation of other techniques like pulse NMR and spin echo, together with the implementation of pulse sequences, increased the number of possible applications, not only in chemistry. The most recent development has been that of magnetic resonance imaging (MRI) [165], which uses spatial encoding of the NMR signal to produce images on the micron scale of the samples under study.

After a brief introduction to the operating principles of the NMR spectroscopy, the most well-known techniques and the instrumentation used in our experiments will be investigated [165–170].

2.1   Principles of NMR

All microscopical particles like electrons, protons and neutrons possess an intrinsic angular magnetic moment called *spin*. This is independent of the history of the elementary particle, being simply a characteristic of its "nature" [166]. Furthermore, it is quantized and can take values $(\pm 1/2)\hbar$, where $\hbar$ is the reduced Planck's constant[22]. In the absence of an external magnetic field, this property is not observable.

Atomic nuclei consist of neutrons and protons (known collectively as nucleons), so they possess a total angular momentum $\vec{J}$.

It appears evident that different isotopes[23] have distinct values of nuclear spin and that some nuclei may have a zero nuclear spin. Furthermore, as stated by Pauli's exclusion principle, in a quantum state there are no fermions with the same values of quantum

---

[22]$\hbar$ is defined as the Planck's constant ($h = 6.626$ x 10^{-34} J · s) divided by 2π.

[23]Nuclei with the same atomic number Z (that specifies the number of protons inside the nucleus), but different mass number (i.e., the number of nucleons in the nucleus) are called isotopes.

numbers. This is why in nucleus quantum states, nucleons tend to pair with another one characterized by an anti-parallel spin. So a nucleus having even numbers of both protons and neutrons (being all paired) has zero total spin. Moreover, nuclei with non-zero spin have an asymmetric positive charge distribution which causes a rotation around the spin axes with angular frequency $\omega = 2\pi\nu$. Anything that is charged and moves has a magnetic moment $\vec{\mu}$, thus produces (and can interact with) a magnetic field. Therefore, a spinning nucleus acts as a tiny bar magnet oriented along the spin rotation axis (figure 2.1).
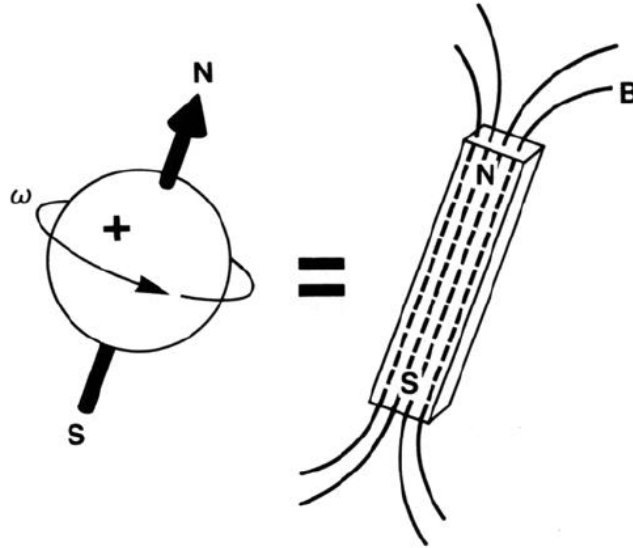

FIGURE 2.1: The charged nucleus (e.g., ^{1}H) rotating with angular frequency ω creates a magnetic field B and is equivalent to a small bar magnet whose axis is coincident with the spin rotation axis.

The vectorial relation between the magnetic moment and the corresponding angular momentum is:

$$\vec{\mu} = \gamma \vec{J} \tag{2.1}$$

where γ is the so-called gyromagnetic ratio[24] (also known as magnetogyric ratio), a constant for each type of nucleus. For the hydrogen atom nucleus (^{1}H), which is simply a proton, it is

$$\gamma = 2.675 \times 10^8 \text{ rad/(s·T)} \tag{2.2}$$

or, equivalently, the "reduced" gyromagnetic ratio $\not{\gamma}$ is

$$\not{\gamma} = \frac{\gamma}{2\pi} = 42.58 \text{ MHz/T} \tag{2.3}$$

where T (Tesla) is the SI unit of magnetic field.

Another quantity that plays a relevant role in NMR is the nuclear magneton. It defines the unit of nuclear magnetic moment:

---

[24]The gyromagnetic ratio may have either sign. Seeing equation 2.1, it is possible to notice that for particles with a negative value of γ (including the electron and a few atomic nuclei), the magnetic moment is opposite in direction to the angular momentum. Vice versa, particles with a positive value of γ (including most atomic nuclei) have a magnetic moment parallel to the angular momentum.

$$\mu_n = \frac{|e|\,\hbar}{2m_p} = 5.05 \times 10^{-27} \text{A} \cdot \text{m}^2 \tag{2.4}$$

where m_p is the proton mass and e the elementary charge.

As it can be seen from table 2.1 the nucleus most sensitive to the presence of an external magnetic field (having the highest value of μ_n) is the hydrogen nucleus.

TABLE 2.1: List of selected nuclear species with their properties relevant for NMR. A complete listing of nuclear spins, gyromagnetic ratio, etc. may be found on the website `https://www.webelements.com`.

Nucleus	Spin	Magnetic moment (μ/μ_n)	γ (MHz/T)	Natural Abund. (%)
Hydrogen (^{1}H)	1/2	2.793	42.58	99.989
Deuterium (^{2}H)	1	0.857	6.53	0.012
Carbon (^{13}C)	1/2	0.702	10.71	1.07
Oxygen (^{17}O)	5/2	-1.893	-5.77	0.038
Fluorine (^{19}F)	1/2	2.627	40.08	100
Sodium (^{23}Na)	3/2	2.217	11.27	100
Phosphorus (^{31}P)	1/2	1.131	17.25	100

2.1.1 The Larmor frequency

The angular momentum of a particle with spin is a vector pointing in any possible direction in space. When a nucleus with an odd number of protons and/or neutrons is placed in a external magnetic field $\vec{B}$, its total angular momentum vector $\vec{J}$ and/or its magnetic moment vector $\vec{\mu}$ (as showed in equation 2.1) aligns with the direction of the field. In particular, the actual response of these vectors is to move around the field producing a cone and keeping a constant angle with the field. This motion is called *precession* [170].

The following fundamental equation of motion

$$\frac{d\vec{\mu}}{dt} = \gamma \vec{\mu} \times \vec{B} \tag{2.5}$$

shows that the time derivative of the magnetic moment vector $\vec{\mu}$ is proportional to a cross product concerning the same vector. This conduces to the fact that its direction changes whereas its magnitude does not. The direct change in the orientation of $\vec{\mu}$ is equal to an instantaneous left-handed rotation about the other vector in the cross product, i.e., the magnetic field $\vec{B}$. The differential change in the moment with respect of the time dt is orthogonal to the plane defined by $\vec{\mu}$ and $\vec{B}$, being $d\vec{\mu} = (\gamma \vec{\mu} \times \vec{B})dt$. This leads to a clockwise precession of $\vec{\mu}$ around $\vec{B}$ direction, and the circular path remains constant if $\vec{B}$ is time independent (figure 2.2).

Denoting with θ the angle between $\vec{\mu}$ and $\vec{B}$ and with $d\phi$ the angle subtended by $d\vec{\mu}$, it is:

$$|d\vec{\mu}| = \mu \sin\theta \, |d\phi| \tag{2.6}$$

but, at the same time, from equation 2.5, it is:

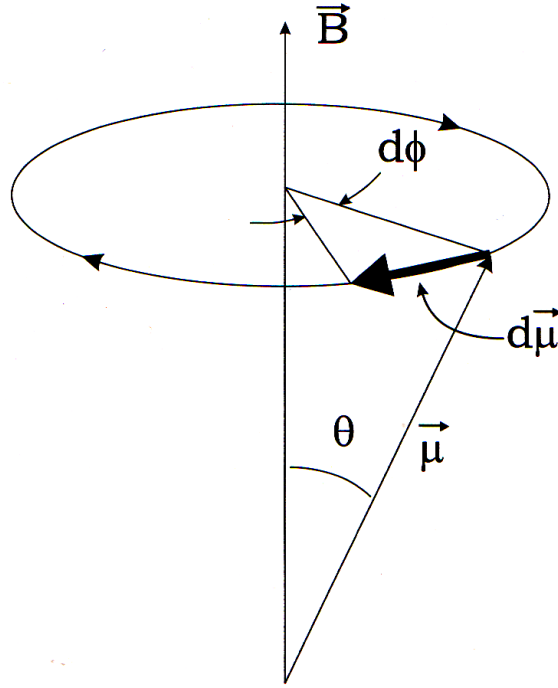$$|d\vec{\mu}| = \gamma \mu B \sin\theta \, |dt| \tag{2.7}$$

FIGURE 2.2: The clockwise precession of the magnetic moment vector $\vec{\mu}$, which is proportional to the spin vector, about a static magnetic field. Figure adapted from [165].

so, it must be $\gamma B \, |dt| = |d\phi|$ with $B \equiv \left| \vec{B} \right|$. It follows the well-known Larmor precession formula:

$$\omega \equiv \left| \frac{d\phi}{dt} \right| = \gamma B \tag{2.8}$$

which relates the precession frequency to the magnitude of the magnetic field. In particular, if the field is along the z-axis and constant in time (i.e., static), it results that $\vec{B} = B_0 \hat{z}$, where B_0 is the magnitude of the static magnetic field. In this frame, the solution of the differential equation 2.8 along a direct axis defined by a left-handed rotation around $\vec{B}$, holds:

$$\phi = -\omega_0 t + \phi_0 \tag{2.9}$$

where ϕ_0 is the initial angle. Consequently, in the case of static field, the Larmor frequency remains constant in time and, substituting the equation 2.9 in equation 2.8 and doing the first derivative, it can thus be defined as:

$$\omega_0 \equiv \gamma B_0 \tag{2.10}$$

and this explains why the value of the resonance frequency is present more often than the magnetic field magnitude referring to NMR experiments.

Note that the Larmor frequency in equation 2.10 is expressed in modulus, but it has a defined sign that indicates the sense of the spin precession around the applied field. In fact, most nuclei have positive γ, in which case the Larmor frequency is negative. This means that the precession is in the clockwise direction, as seen when looking "upstream"

with respect to the direction of the magnetic field. Vice versa, a few nuclei are characterized by negative values of γ and the Larmor frequency is positive. This indicates the precession in the anticlockwise direction, as seen when looking "upstream" with respect to the direction of the magnetic field [166].

2.1.2 Magnetization and relaxation times

Considering the static field along z-axis, the differential equation 2.5 may be decomposed into three Cartesian equations:

$$
\begin{aligned}
\frac{d\mu_x}{dt} &= \gamma \mu_y B_0 = \omega_0 \mu_y \\
\frac{d\mu_y}{dt} &= -\gamma \mu_x B_0 = -\omega_0 \mu_x \\
\frac{d\mu_z}{dt} &= 0
\end{aligned}
\tag{2.11}
$$

Furthermore, taking additional derivatives the coupling between the first two equations can be removed:

$$
\begin{aligned}
\frac{d^2\mu_x}{dt^2} &= -\omega_0^2 \mu_x \\
\frac{d^2\mu_y}{dt^2} &= -\omega_0^2 \mu_y
\end{aligned}
\tag{2.12}
$$

These second-order differential equations have known solutions of the general form $C_1 \cos \omega_0 t + C_2 \sin \omega_0 t$. By assuming the initial conditions (at $t = 0$) the time dependent components of the magnetic moment vector are

$$
\begin{aligned}
\mu_x(t) &= \mu_x(0) \cos \omega_0 t + \mu_y(0) \sin \omega_0 t \\
\mu_y(t) &= \mu_y(0) \cos \omega_0 t - \mu_x(0) \sin \omega_0 t \\
\mu_z(t) &= \mu_z(0)
\end{aligned}
\tag{2.13}
$$

being $\vec{\mu}(t) = \mu_x(t)\hat{x} + \mu_y(t)\hat{y} + \mu_z(t)\hat{z}$.

Until now it has been considered only the case of a single spin, but of course one cannot deal with a single atom. The actual observable is the macroscopic magnetization $\vec{M}$, which corresponds to the sum of all the individual nuclear magnetic moments:

$$
\vec{M} = \sum_i \vec{\mu}_i.
\tag{2.14}
$$

When an ensemble of nuclei is immersed in a static magnetic field, there will be a slight excess of nuclei whose spin aligns with the magnetic field, because this is the lowest energy state. So $\vec{M}$ is oriented along the positive z-axis. As a matter of fact, the NMR signal is determined by the total magnetization of the system and not by the magnetic moment of an individual nucleus.

A sum over the equations of motions for the individual spins (equation 2.5), without considering spins interactions with their environment, yields:

$$\sum_i \frac{d\vec{\mu}_i}{dt} = \gamma \sum_i \vec{\mu}_i \times \vec{B} \tag{2.15}$$

or, substituting equation 2.14

$$\frac{d\vec{M}}{dt} = \gamma \vec{M} \times \vec{B} \tag{2.16}$$

that unquestionably has the same functional dependence compared to equation 2.5.

It is useful to analyse the magnetization in terms of its parallel and perpendicular components, thus distinguishing between longitudinal

$$M_{\parallel} = M_z \tag{2.17}$$

and transversal components

$$\vec{M}_{\perp} = M_x \hat{x} + M_y \hat{y} \tag{2.18}$$

Solving the cross product (equation 2.16) in terms of these components leads to the following decoupled equations (always in the case of non-interacting spins):

$$\frac{dM_{\parallel}}{dt} = \frac{dM_z}{dt} = 0 \tag{2.19}$$

and

$$\frac{d\vec{M}_{\perp}}{dt} = \gamma \vec{M}_{\perp} \times \vec{B} \tag{2.20}$$

In both equations, we have neglected terms that consider how the magnetization approaches its equilibrium value (M_0) after a perturbation. For instance, the application of a Radio-Frequency (RF) magnetic field $\vec{B}_1$ having components in the x or y direction makes $\vec{M}$ to tilt away from its equilibrium direction (assume the z-axis).

To understand the energy exchange between the spins and the environment, it is important to introduce the classical energy associated with a magnetic moment immersed in a magnetic field:

$$E = -\vec{\mu} \cdot \vec{B} \tag{2.21}$$

The moment tends to align parallel to the field in order to reach its minimum energy state, being able to give up the energy excess. Since the spins are in thermal contact with the lattice of nearby atoms, it is possible that a spin can exchange a quantum of energy with the lattice. This causes that longitudinal magnetization reaches its equilibrium value M_0 whereas the transverse magnetization vanishes. Therefore, the rate of change of the longitudinal magnetization (dM_z/dt) is proportional to the difference $M_0 - M_z$:

$$\frac{dM_z}{dt} = \frac{1}{T_1}\left(M_0 - M_z\right) \tag{2.22}$$

where T_1 is the *spin-lattice relaxation time*, which takes into account the interactions between the spins and their environments. Its value ranges from tens to thousands of milliseconds for protons in compounds with H atoms. By solving equation 2.22, one can obtain the time dependence of the longitudinal magnetization:

$$M_z(t) = M_z(0)\, e^{-t/T_1} + M_0 \left(1 - e^{-t/T_1}\right) \tag{2.23}$$

This relation is displayed in figure 2.3 showing the evolution from the initial value of the longitudinal magnetization $M_z(0)$ to its equilibrium value M_0.
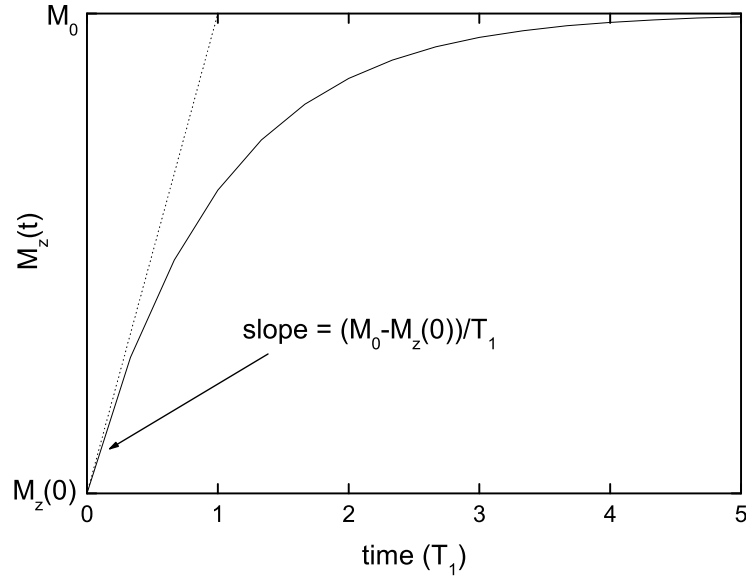

FIGURE 2.3: Time dependence of the longitudinal magnetization. It is clear its regrowth from the initial value $M_z(0)$ to the equilibrium value M_0. The time axis is expressed in units of T_1. Data taken from [165].

The disappearance of $\vec{M}_\perp$ is due to a spin "dephasing" mechanism. Every spin experiences a local field which is the union of the external macroscopic field and the local microscopic fields of their neighbours. Since variations in the local fields lead to different local precessional frequencies, individual spins dephase in time (equation 2.9) decreasing the net magnetization vector. Indeed, the rate of change of the transverse magnetization (equation 2.20) has an additional negative term which accounts for spin dephasing mechanisms.

$$\frac{d\vec{M}_\perp}{dt} = \gamma \vec{M}_\perp \times \vec{B} - \frac{1}{T_2} \vec{M}_\perp \tag{2.24}$$

where T_2 is the *spin-spin relaxation time*, which considers the reduction in transverse magnetization due to differences between the local field felt by different spins.

Considering a reference system $(x'y'z')$ rotating at the Larmor precession frequency, the spin axis is not moving. In general, with respect to the laboratory frame, the time rate of change of a vector (e.g., $\vec{M}$) instantaneously rotated by an angular speed vector $\vec{\Omega}$ may be written as

$$\frac{d\vec{M}}{dt} = \vec{\Omega} \times \vec{M} \tag{2.25}$$

The total time derivative of $\vec{M}$ is

$$\frac{d\vec{M}}{dt} = \left(\frac{d\vec{M}}{dt}\right)' + \vec{\Omega} \times \vec{M} \tag{2.26}$$

where the primed derivative quantity is estimated as the rate of change of $\vec{M}$ with respect to the rotating frame. Substituting equation 2.16, one obtains

$$\left(\frac{d\vec{M}}{dt}\right)' = \gamma\,\vec{M} \times \vec{B}_{\text{eff}} \tag{2.27}$$

where

$$\vec{B}_{\text{eff}} = \vec{B} + \frac{\vec{\Omega}}{\gamma} \tag{2.28}$$

is an effective magnetic field equal to the superposition of the external magnetic field and an additional magnetic field having the same direction of $\vec{\Omega}$.

Coming back to equation 2.24, it is possible to write the time derivative of $\vec{M}_\perp$ with respect to the rotating reference frame as

$$\left(\frac{d\vec{M}_\perp}{dt}\right)' = -\frac{1}{T_2}\,d\vec{M}_\perp \tag{2.29}$$

that has solution

$$\vec{M}_\perp(t) = \vec{M}_\perp(0)\mathrm{e}^{-t/T_2} \tag{2.30}$$

which describes an exponential decay of the magnitude of the transverse magnetization from its initial value $\vec{M}_\perp(0)$ to zero.
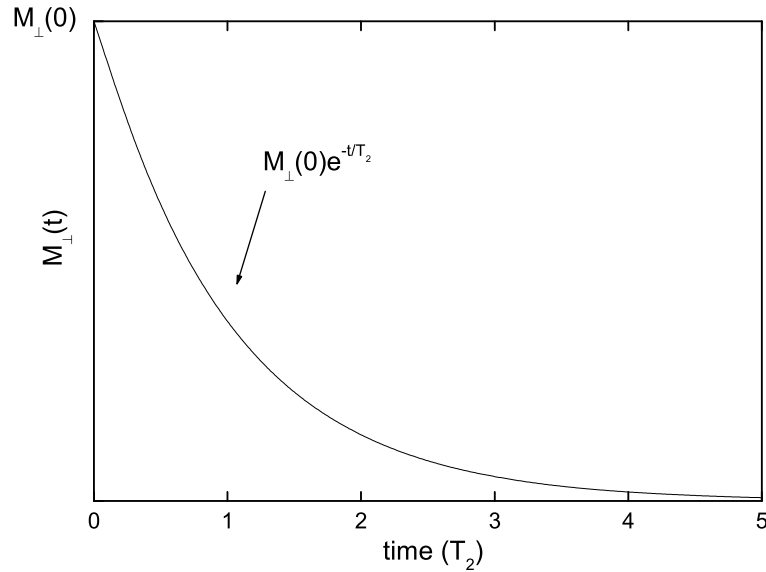

FIGURE 2.4: Time dependence of the transverse magnetization. It is evident the exponential decay of its magnitude from an initial value. The time axis is expressed in units of T_2. Data taken from [165].

This solution is valid both in the laboratory and rotating reference frames and is plotted in figure 2.4. The value of T_2 ranges from microseconds (for solids) to seconds (for liquids) and it is generally less than the T_1 of the same species. The difference of six orders in the magnitude between the values of T_2 in the case of solids and in that of liquids

is due to the dissimilar strength of intermolecular interactions. Of course, in solids, the spin-dephasing mechanism is quicker than in liquids thanks to stronger intermolecular interactions, thus a more intense local field.

If the external magnetic field possesses spatial inhomogeneities, the magnetization has an additional dephasing characterized by a separate decay time T_2'. This leads to an effective decay time T_2^* for the transverse magnetization

$$\frac{1}{T_2^*} = \frac{1}{T_2} + \frac{1}{T_2'} \tag{2.31}$$

However, it will be shown that the effect of spatial dissimilarities is recoverable by using an appropriate *pulse sequence*.

2.1.3 The Bloch equation

Taking into account the differential equations 2.22 and 2.24 for magnetization, equation 2.16 can be rewritten obtaining the following empirical vector equation

$$\frac{d\vec{M}}{dt} = \gamma \vec{M} \times \vec{B} + \frac{1}{T_1}\left(M_0 - M_z\right)\hat{z} - \frac{1}{T_2}\vec{M}_\perp \tag{2.32}$$

known as the *Bloch equation*. Precisely, remembering that it is $\vec{B} = B_0\hat{z}$, the Bloch equations are a set of three coupled differential equations for the components of the magnetization vector

$$\begin{aligned}
\frac{dM_z}{dt} &= \frac{M_o - M_z}{T_1} \\
\frac{dM_x}{dt} &= \omega_o M_y - \frac{M_x}{T_2} \\
\frac{dM_y}{dt} &= -\omega_o M_x - \frac{M_y}{T_2}
\end{aligned} \tag{2.33}$$

whose solutions are

$$\begin{aligned}
M_x(t) &= e^{-t/T_2}\left(M_x(0)\cos\omega_0 t + M_y(0)\sin\omega_0 t\right) \\
M_y(t) &= e^{-t/T_2}\left(M_y(0)\cos\omega_0 t - M_x(0)\sin\omega_0 t\right) \\
M_z(t) &= M_z(0)e^{-t/T_1} + M_0\left(1 - e^{-t/T_1}\right)
\end{aligned} \tag{2.34}$$

For $t \rightarrow \infty$, the equilibrium solutions can be obtained:

$$M_x(\infty) = M_y(\infty) = 0, \quad M_z(\infty) = M_0 \tag{2.35}$$

So, after the application of a RF field along the x-axis, when the magnetization lies in the (x,y) plane, the longitudinal component decays exponentially (from its initial value $(M_z(0) = 0)$ to its equilibrium value $(M_z(\infty) = M_0)$) with a $1/T_1$ time rate, whereas the transverse component rotates clockwise in decaying exponentially and vanishes with a $1/T_2$ time rate.

The equilibrium value M_0 for the longitudinal magnetization obeys Curie's law as for its dependence on the absolute temperature T and the external field:

$$M_0 = C\frac{B_0}{T} \tag{2.36}$$

where C is a constant depending on the considered nucleus.

2.1.4 Resonance condition and flip-angle

When a RF field $\vec{B}_1$ is overlapped to the static field B_0, all spins experience a total magnetic field which is the vectorial sum of the two fields. For simplicity, let us consider this case in the rotating reference frame whose angular frequency is ω. Here $\vec{B}_1$ is at rest and assumed to be directed along x'-axis. Therefore the total external field is

$$\vec{B} = B_0\hat{z} + B_1\hat{x}' \tag{2.37}$$

and the effective field in the rotating frame is

$$\vec{B}_{\text{eff}} = \left(B_0 - \frac{\omega}{\gamma}\hat{z} + B_1\hat{x}' \right) \tag{2.38}$$

If $\omega_1 = \gamma B_1$ is the spin-precession frequency generated by the RF field, equation 2.38 becomes:

$$\vec{B}_{\text{eff}} = \left[(\omega_0 - \omega)\hat{z} + \omega_1\hat{x}' \right] / \gamma \tag{2.39}$$
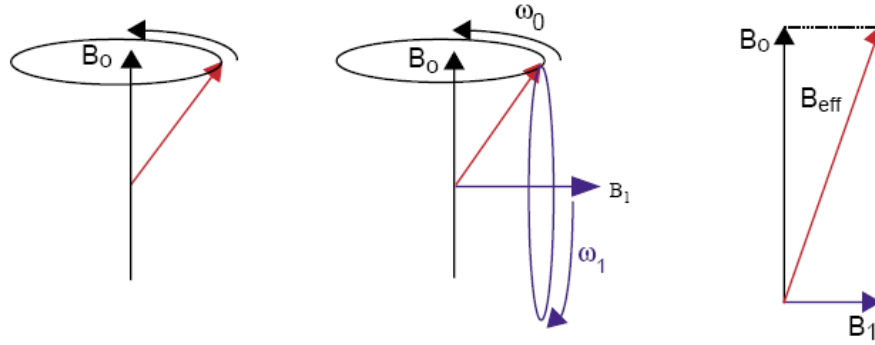

FIGURE 2.5: Movement of spins in the presence of only the B_0 field (left), B_0 and B_1 field (middle) and vector addition to calculate the effective field B_{eff} formed by B_0 and B_1.

When the applied RF frequency ω matches the Larmor frequency ω_0, there is only a precession of the spins about the $\hat{x}'$-axis with frequency ω_1. Therefore, in this resonance condition the B_1 field is maximally synchronized to make the spin (so the magnetization) precess around the $\hat{x}'$-axis (figure 2.5).

When a B_1 field is applied on-resonance for a finite time τ (i.e., with an RF pulse) the spin rotates around $\hat{x}'$ with an angle

$$\Delta\theta = \gamma B_1 \tau \tag{2.40}$$

The angle in 2.40 is the so-called *flip-angle*, a very important quantity in NMR applications, because it denotes the angle of which the magnetization is projected with respect to its equilibrium direction. Usually, the pulse lengths τ are chosen so that the flip-angle $\Delta\theta$ is either 90 or 180 degrees. The effect of the B_1 field is to create phase coherence amongst the spins. The coherent spins sum up to give the macroscopic transverse magnetization (figure 2.6). In fact, the application of an RF field perpendicular to the magnetic

field (e.g., along the *x*- or *y*-axis), creates a state in which the phases of the spins are partially correlated. This condition is called *coherence*. When projecting the vectors onto the (*x*,*y*) plane the resulting transverse magnetization is non-vanishing giving rise to an RF signal. When the motions of spins are described in vector diagrams most frequently only the vector sum of the spins is shown in order to simplify it.
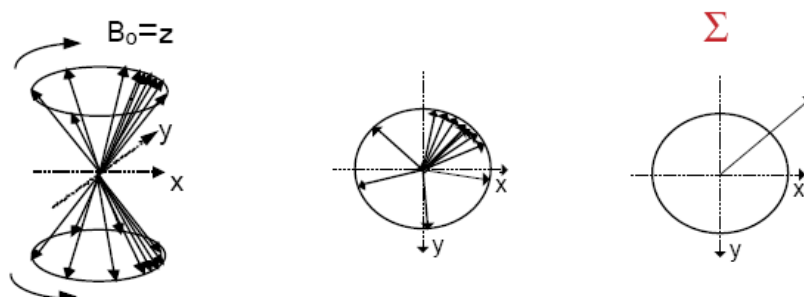

FIGURE 2.6: Coherent state of spins (left) states and the projection onto the (*x*,*y*) plane (middle) and sum vector of the (*x*,*y*) component.

The magnitude and direction of the magnetization vector can be calculated by vectorial addition of the separate dipole moments. This is shown in the following figure (figure 2.7) in which the vector sum of longitudinal (blue) and transverse (yellow) magnetization of uncorrelated spins which are all aligned with respect to B_0 direction (A) or in both possible orientations (B) is displayed as well as for correlated states (C and D): it is evident that only for correlated states transverse magnetization is observed. Only transverse magnetization leads to a detectable NMR signal. Therefore, only the vector sum of the transverse component is shown to describe the relevant part of the spins:
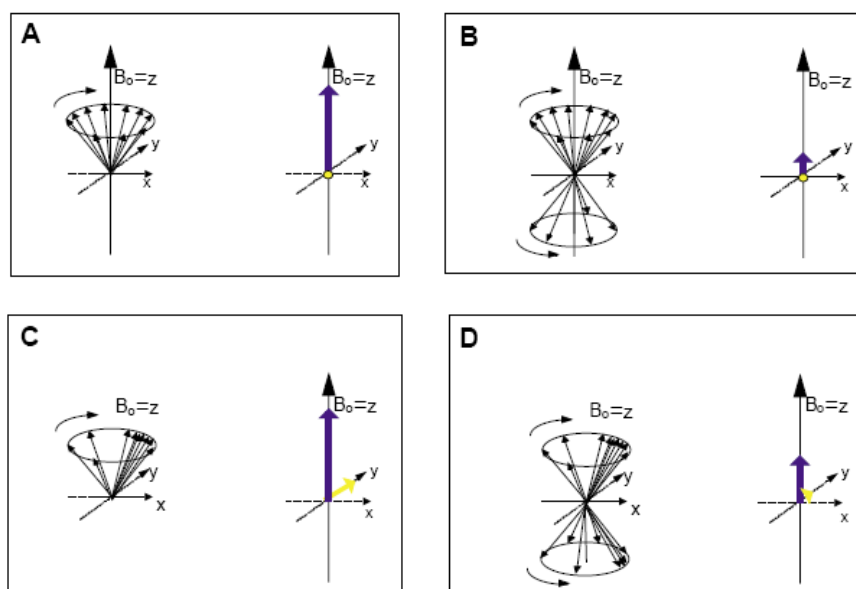

FIGURE 2.7: Different states of the spin system.

2.1.5 Quantum-mechanical approach

Until now, we have used a classical approach to determine the behaviour of an ensemble of spins immersed in a static magnetic field. As stated before, nuclei consist of nucleons, so they possess a total angular momentum $\vec{J}$

$$\vec{J} = \vec{S} + \vec{L} \tag{2.41}$$

in which $\vec{S}$ is the spin angular momentum and $\vec{L}$ is the orbital angular momentum. This physical quantity is quantized by two quantum numbers j and m_j as

$$|\vec{J}| = \hbar\sqrt{j(j+1)} \tag{2.42}$$

$$J_z \equiv |\vec{J}_z| = m_j \hbar \tag{2.43}$$

in which J_z represents the z-axis component of the total angular momentum. In particular, j is the main total angular momentum quantum number and it takes the values

$$|l - s| < j < l + s \tag{2.44}$$

where l is the azimuthal quantum number (parameterizing the orbital angular momentum, $l = 0, 1, 2, \ldots$) and s is the spin quantum number (parameterizing the spin, $s = 0, \frac{1}{2}, 1, \frac{3}{2}, \ldots$). Lastly, m_j is the secondary total angular momentum quantum number (ora magnetic quantum number) that ranges from $-j$ to $+j$ in steps of one.

The spin angular momentum and orbital angular momentum vectors have analogous quantum numbers and quantization rules. For $\vec{L}$, it holds

$$|\vec{L}| = \hbar\sqrt{l(l+1)} \tag{2.45}$$

and

$$L_z \equiv |\vec{L}_z| = m_l \hbar \tag{2.46}$$

where m_l is the angular quantum number, which can assume $2l + 1$ values, ranging from $-l$ to l. On the other hand, for $\vec{S}$ it holds

$$|\vec{S}| = \hbar\sqrt{s(s+1)} \tag{2.47}$$

and

$$S_z \equiv |\vec{S}_z| = m_s \hbar \tag{2.48}$$

where m_s is the spin quantum number, which can assume $2s + 1$ values, ranging from $-s$ to s.

If we do not care about orbital angular momentum, thinking only of systems where $l = 0$ (spherically symmetric nuclei), we can assume that $\vec{J}$ equals $\vec{S}$ thus j equals m_s. This is of course true for a single proton which, being a fermion such as electrons and neutrons, possesses a half-integer spin, i.e. a spin-1/2 or $s = 1/2$. The corresponding two values of m_s are just $m_s = -1/2$ and $m_s = 1/2$. The energy discrimination of these states is only possible when nuclei are immersed in a magnetic field. In fact, in this configuration nuclear energy levels split in a number of different energy levels corresponding to the number of possible m_s (Zeeman splitting, [159]). This follows from the expression of magnetic energy (equation 2.21):

$$E = -\vec{\mu} \cdot \vec{B} = -\mu_z B_0 = -\gamma m_s \hbar B_0 \tag{2.49}$$

having considered the magnetic field $\vec{B} = B\hat{z}$ directed along the z-axis and equation 2.1 and equation 2.48 (remembering that here $\vec{J} = \vec{S}$). Thus for each value of m_s, there is a corresponding energy level available when a magnetic field is applied. In the case of the proton, when $m_s = 1/2$, the spin will orient parallel to the field (the most favourable situation because magnetic energy is minimum). Instead when $m_s = -1/2$, the proton spin will be anti-parallel to the field. Having in mind that quantum selection rules state that only transitions with $\Delta m = \pm 1$ are allowed, let us calculate the energy corresponding to a transition between the two spin states of the proton:

$$\Delta E = E\left(m_s = -\frac{1}{2}\right) - E\left(m_s = \frac{1}{2}\right) = \frac{1}{2}\gamma\hbar B_0 - \left(-\frac{1}{2}\gamma\hbar B_0\right) = \hbar\omega_0 \qquad (2.50)$$

where the frequency ω_0 associated with the emission (or absorption) of a quantum of energy (photon) is just the same as the Larmor precession frequency, the classical precession frequency of a magnetic moment.

All the classical theories can be formulated as a limit of a quantum-mechanical approach. However, we will use quantum formalism only when explicitly needed.

2.1.6 Fourier Transform NMR

Consider an ensemble of protons immersed in a static magnetic field $|\vec{B}| = |B_0\hat{z}| = \omega_0/\gamma$. Their distribution between the two possible energy states, under conditions in which the nuclear spin system is not perturbed by application of any RF field, is given by the Boltzmann equation:

$$\frac{N_+}{N_-} = e^{-\Delta E/k_B T} = e^{-\hbar\omega_0/k_B T} = e^{-\hbar\gamma B_0/k_B T} \qquad (2.51)$$

where N_+ and N_- represent the population of protons in highest and lowest energy states, respectively, $\Delta E = E_+ - E_-$, k_B is the Boltzmann constant, and T is the absolute temperature expressed in K. The use of stronger magnetic fields will increase the population ratio which determines the strength of NMR signal. In fact, after the application of an RF field, transitions between the two states take place and only the difference between populations can be detected. If $N_+ = N_-$ this would result in an overall zero contribution.

When the applied RF field is switched off, the magnetization starts to relax. The decay of the transverse magnetization produces an RF signal in the (x,y) plane (analogous to the applied one) which can be detected by an RF receiver.

This decay is known as the Free Induction Decay (FID), shown in figure 2.8, and can be converted using a Fourier transform (FT) into a frequency-dependent pattern of nuclear resonances, i.e., the nuclear magnetic resonance spectrum (figure 2.9).

As we have already mentioned, the spin precession frequency can change according to the local field experienced by the spin itself. It means that, even considering the same H nucleus in different molecular environments (like in CH_2, CH_3, etc), this will have marginally distinct resonance frequencies in each molecular configuration. The FID signal is indeed composed of all these contributions (figure 2.10) and can be decomposed by means of FT (figure 2.11).

In the spectrum shown in figure 2.11, all the individual frequencies are in principle observable. These frequency changes can be described in terms of *chemical shift*[25].

The chemical shift σ is an assumed linear response of the electronic structure to the external magnetic field and it is defined as

---

[25]The chemical shift is the resonant frequency of a nucleus relative to a standard in a magnetic field.
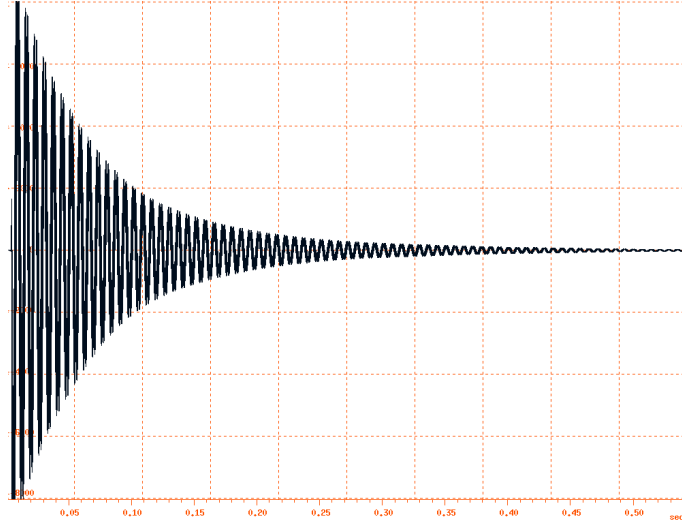
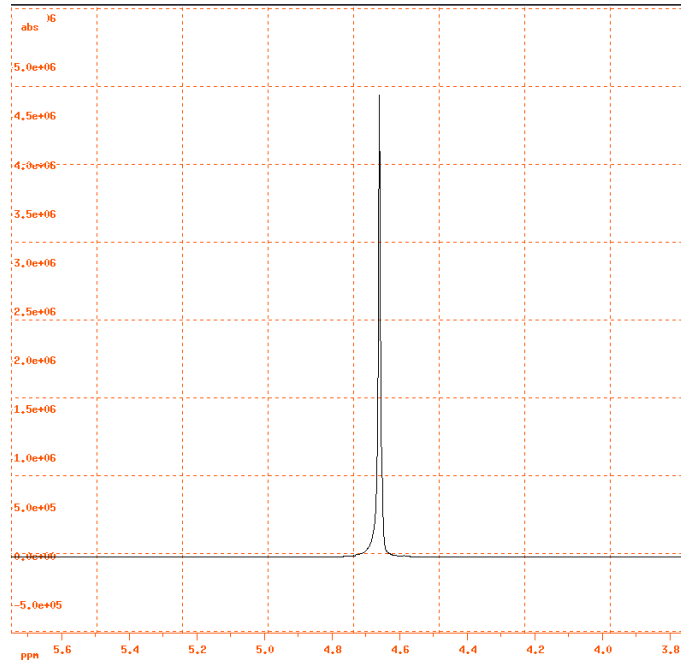FIGURE 2.8: Free Induction Decay for a water sample.

FIGURE 2.9: The spectrum for the water sample obtained after the Fourier transformation.

$$B_{\text{shifted}}(j) = (1 - \sigma_j)B_0 \tag{2.52}$$

where j is an index identifying the chemical environment. The FID contains information about the set of all nuclear species in the studied sample whose frequencies lie within the harmonic content of the RF pulse. An RF pulse is a polychromatic source of RFs covering a broad band of frequencies. The covered bandwidth is proportional to the inverse of the pulse duration. Short pulses are required for uniform excitation of large bandwidths, while long pulses lead to selective excitation.
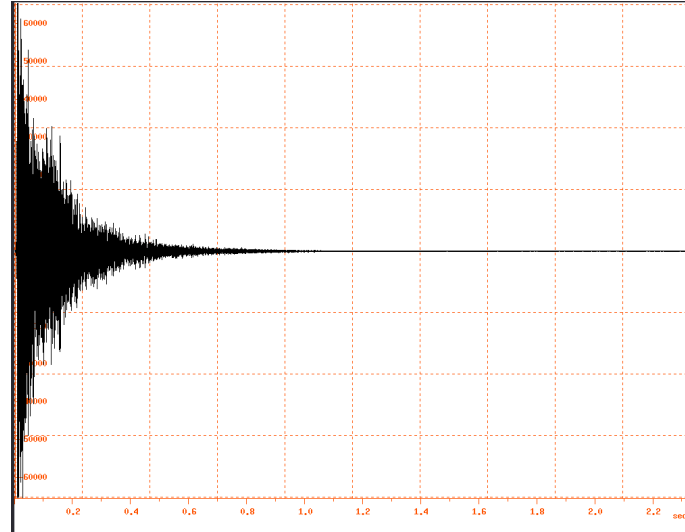
FIGURE 2.10: Free Induction Decay for a sample with multiple reso-
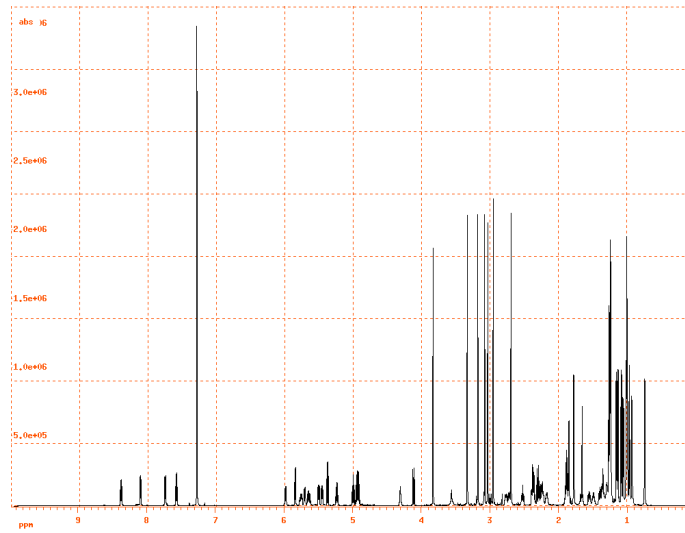nance frequencies.

FIGURE 2.11: Spectrum of the sample whose FID is reported in figure
2.10 displaying multiple resonance frequencies.

As an example, let us consider that the jth species contains $\mathcal{N}_j$ hydrogen nuclei with chemical shift σ_j. The time dependence of the phase of each nucleus is

$$\phi_j(t) = -\gamma B_0 (1 - \sigma_j) t \tag{2.53}$$

and the overall signal from this set of spins is given by

$$s(t) \propto \sum_j \mathcal{N}_j \, e^{i\gamma\sigma_j B_0 t} \tag{2.54}$$

For a continuous set of $\mathcal{N}_j$, the sum is replaced by an integral over a continuous distribution in σ:

$$s(t) \propto \int d\sigma \mathcal{N}(\sigma) \, e^{i\gamma\sigma B_0 t} \tag{2.55}$$

This signal is therefore the FT of the spin distribution $\mathcal{N}(\sigma)$. It is through inverse Fourier transforms that the signal can be processed in order to determine the original species profile. The chemical shift is a powerful tool used for example by chemists to obtain information on the chemical composition of the studied sample.

The obtained profile in the frequency domain (figure 2.11) generally represents the overlap of several Lorentzian peaks[26], whose characteristics are clearly and intimately related to the corresponding chemical species. The most relevant parameter, besides the peak position, is the Full-Width at Half-Maximum (FWHM), which is strictly related to the relaxation time T_2, so takes the strength of intramolecular interactions into account. As already said, the T_2 decay is quicker for solids than for liquids because of stronger interactions: this leads to a broader peak for a solid with respect to that of a liquid.

2.2 The instrument

Usually, the static magnetic field in an NMR instrument is produced by a superconducting magnet, an electromagnet that produces a magnetic field by means of an electric current. The magnet core consists of a large coil of current carrying wire in the shape of a solenoid. At the centre of the coil, a very intense static magnetic field exists, inside which the sample to be analysed is placed. When the magnet is first installed, a current is started in the main coil. This is referred to as "charging" the magnet. Once charged, the magnet should continue to operate for many years and the only maintenance required by the magnet is to ensure that the coil is kept at a sufficiently low temperature in order to maintain its superconducting condition. This is achieved by placing the main coil that produces the field in a liquid helium bath in turn surrounded by a liquid nitrogen dewar to reduce loss of helium. In particular, maintaining the superconducting state of the magnet is really important because a superconducting wire carries electricity without the need for any driving energy. So, since a current is started in a superconducting loop, it will continue forever. The scheme of the NMR spectrometer already described is shown in figure 2.12a.

The boiling point of helium is 4K (-269 ^{o}C), thus if the coil is kept immersed in liquid helium we can be sure that the temperature is at 4K or below. This is sufficiently cold to ensure that the magnet coil remains superconducting. However, if a large part of the superconducting coil is no longer covered with liquid He, the temperature of the superconducting coil will increase and at some stage will become non-superconducting. The resistance in the coil would then result in a sudden breakdown of the magnetic field accompanied with the generation of heat which would very quickly lead to the evaporation of large quantities of liquid helium and nitrogen. The magnet room may suddenly become filled with evaporated gas and the magnet is said to have "quenched".

Commercially, a range of magnets are available with different strengths. The strength of the magnet is graded according to the frequency of the NMR signals emitted by hydrogen atoms. The stronger the magnet the higher this hydrogen frequency. For example, the magnet used in our experiments and located at the Department of Mathematical and Informatics Sciences, Physical Sciences and Earth Sciences (MIFT) at University of Messina (Italy) is an Avance Bruker 700 MHz magnet (16.4 Tesla) (figure 2.12b), this means that when a chemical sample is placed in the magnet for analysis, the ^1H atoms in the sample will emit signals with a frequency very close to 700 MHz.

---

[26]The Fourier transform of a decaying exponential is exactly a Lorentzian.
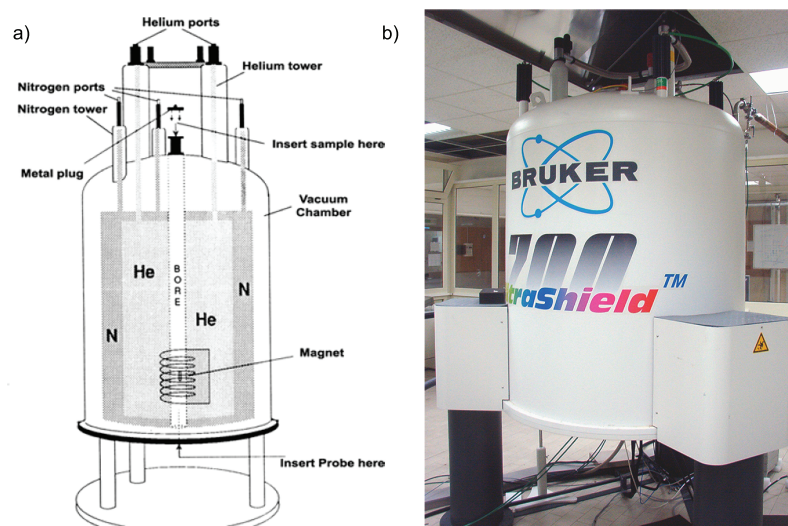
FIGURE 2.12: (a) Scheme of the NMR spectrometer used. Note that the "magnet" printed in the figure indicates a superconducting magnet. Figure taken from [171]. (b) Photography of the Avance Bruker NMR Spectrometer operating at 700 MHz.

Considering that the precession frequencies are proportional to the magnetic field strength, the latter has to be greatly homogeneous across the sample volume to observe small frequency differences. If the field was not highly homogeneous, the effective field strengths in different volume sections inside the sample would be distinct, so the spins would process at different rates among each other. This would lead to considerable line-broadening (inhomogeneous broadening), whereas improving the homogeneity will result in better spectral resolution. The operation to adjust the field homogeneity is called *shimming* and the device that corrects for locally slightly different magnetic fields is called shim-system. It consists of small coils with regulated currents which produce small additional magnetic fields used indeed to correct the inhomogeneous field created by the main coil. There are a number of such coils of varying geometry producing correction fields in different orientations. These have to be regulated by the user whenever a new sample is placed in the magnet or the temperature is changed. It is generally done with the keyboard called *BSMS keyboard* connected to one rack (the BSMS) of the spectrometer console. With this keyboard, displayed in figure 2.13, it is also possible to do many operations such as ejecting or inserting the sample, check the percentage of liquid helium in the inner dewar and so on.

The probehead (or simply *probe*) is designed to hold the sample, transmit radio frequency signals which excite the sample and receive the emitted response. The transmission and reception is achieved by using specially designed RF coils. The probe is inserted into the bottom of the magnet and sits inside the shims. Coaxial cables carry the excitation signals from the console amplifiers to the probe and the NMR signal back from the sample to the receiver. The cables are routed through a set of pre-amplifiers needed to boost the NMR signals which are typically very weak. All the electronics is managed by the spectrometer console where the signal amplifier and the signal generation unit are located, as well as many other apparatuses like the input and output of the dry nitrogen used to control the sample temperature.

The sensitivity of any probe will change with the frequency of the signal transmitted

FIGURE 2.13: BSMS Keyboard by means of that it is possible to do several operations such ejecting/inserting the sample, change the shim coils current and so on. Figure taken from [171].

and there exists a frequency at which the probe is most sensitive. This latter may be regulated over a certain range using tuning capacitors built into the probe circuitry, in order to adapt the frequency of highest sensitivity with the relevant transmission frequency. For broadband probes, the frequencies transmitted will vary considerably from nucleus to nucleus, so the probe will need to be tuned each time that a different nucleus is selected. Whenever a probe is tuned, it should also be matched and this involves the ensuring that the maximum amount of power arriving at the probe base be transmitted up to the topmost coil of the probe. This ensures that the minimum amount of the power arriving at the probe base is reflected back towards the amplifiers (and consequently wasted). The amplifiers we use have an output impedance of 50 Ohms, therefore optimal matching occurs when the probe impedance along all cables is also 50 Ohms. The routine that executes the probehead tuning is called *wobble*. It transmits a poor signal to the probe comparing the latter and the cable impedance with a 50 Ohm reference within the preamplifier. The transmitted frequency is centered at the observation frequency (the resonance frequency of the observed nucleus), but it "swept" over a range determined by the size of the parameter wobble-spectral-width. The resultant curve is the familiar response curve of a resonant circuit, simply a measure of the amplitude of the reflected signal (vertical axis) against frequency (horizontal axis).

Matching simply involves adjusting the probe, so that the minimum of the wobble curve is at the bottom of the display. This represents the minimum reflection of the transmitted signal. The tuning operation involves the confirming that this occurs at the frequency of transmission which will be at the center of the screen's horizontal scale. The adjustment is made using two screws labelled at the base of the probe with the special tool provided. When the wobble curve minimum is centred and at the base of the screen the probe has been optimally tuned and matched.

After tuning, matching and shimming operations, one is ready to record an optimal NMR signal. It is generally obtained with the application of a pulse sequence which
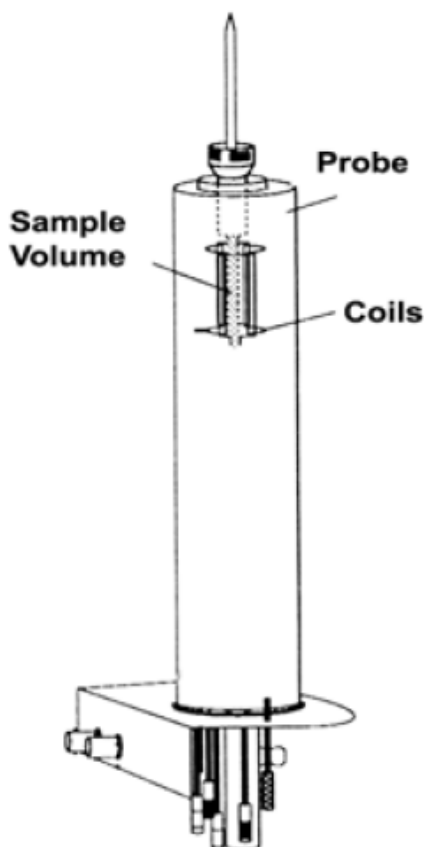
FIGURE 2.14: The scheme of a probehead and the sample position inside it. Figure taken from [171].

depends on the type of observation one is interested in. We now introduce some of the most important pulse sequences, that furthermore have been used in our experiments discussed in the next chapter.

2.3 Pulse sequences

The most important pulse sequence is the 90° ($\pi/2$) one, generally used as a first inspection of the sample. It consists of an RF pulse directed along the x-axis (with respect to the laboratory reference frame) which projects the macroscopic magnetization into the (x,y) plane. Note that, in thermal equilibrium, the magnetization is oriented parallel to the external magnetic field (z-direction). After the $\pi/2$ pulse there is no further magnetization in the z-direction and the phases of all rotating nuclear spins are the same as the phase of the incoming high frequency field. However, when the pulse ends, the magnetization relaxes to its equilibrium value (M_0), while rotating into the (x,y) plane and releasing the absorbed energy as an RF signal also directed along the x-axis and decaying exponentially in time. The energy carried by the pulse depends on the power and the duration time τ of the pulse itself. The pulse duration time τ is inversely proportional to the frequency range covered by the pulse.

This free induction (FID) or phase coherence of the spin decays with the apparent

transversal relaxation time T_2^*, which depends on the strength of the intermolecular interactions inside the sample and on the static field inhomogeneities. In order to neglect the field inhomogeneities and to measure the real T_2, we use the so-called spin-echo pulse sequence (figure 2.15).
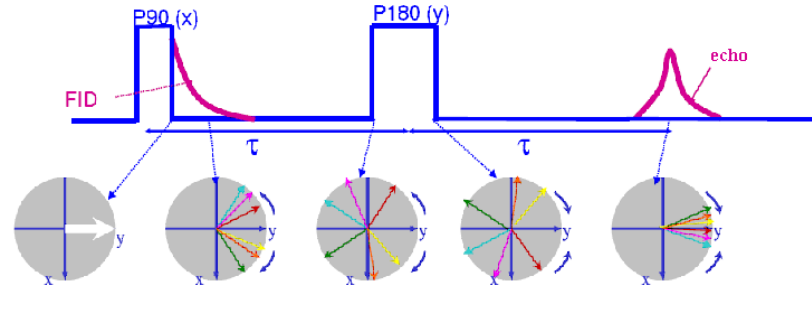

FIGURE 2.15: The timing diagram for the spin-echo pulse sequence.
Varying the delay between the two RF pulses, on e obtain a function
whose time decay is just T_2.

Here a 90° pulse is first applied to the spin system, then usually after a variable time delay, a 180° (π) pulse is applied, which has twice the duration (or the power) of a $\pi/2$ pulse. This pulse rotates the magnetization by 180 degrees about the x- (or the y-) axis. The 180° pulse causes the magnetization to rephase at least partially and produce a signal called *echo* (figure 2.15). By varying the so-called echo time (TE), i.e., the time between the $\pi/2$ RF pulses and the maximum amplitude in the echo, it is possible to evaluate the spin-spin relaxation time T_2. In fact the dependence of important parameters, such as the area or the intensity, of the obtained signals after being Fourier transformed (S_{FT}) is the following:

$$S_{FT} = S_0 \, e^{-\frac{TE}{T_2}} \tag{2.56}$$

where the constant S_0 is just an amplitude.

In order to measure the other relaxation time of the magnetization, i.e., the longitudinal spin-lattice relaxation time, it is used a pulse sequence called *inversion recovery*. Consider that when the magnetization is in equilibrium and a π pulse is applied, the magnetization tilts from the z-direction to its opposite. Since no observable coherences are created, we still need a further $\pi/2$ pulse to measure the T_1-relaxation after the π pulse. This pulse has the property that the population differences are converted into observable coherences. Taking phase relations into consideration, the application of a $\pi/2$ pulse directly after a π pulse results in a negative signal. This signal has the same magnitude as the positive signal that would have been created if we used a $\pi/2$ pulse alone. With increasing pulse delay, described by the variable delay parameter VD, the negative signal corresponding to the T_1 relaxation of the spin system is decreased. After time VD(0), the signal goes through zero since no further macroscopic population differences are observable. As VD further increases, the signal becomes positive and approaches the value that would have been observed after the sole application of a $\pi/2$ pulse.

By increasing the variable delay parameter VD, as the longitudinal component of the macroscopic magnetization passes from zero, one has $VD(0) = T_1 \ln 2$. From that we have a simple procedure to determine T_1, which, however, requires good adjustment of the pulses duration and a homogeneous high frequency field.
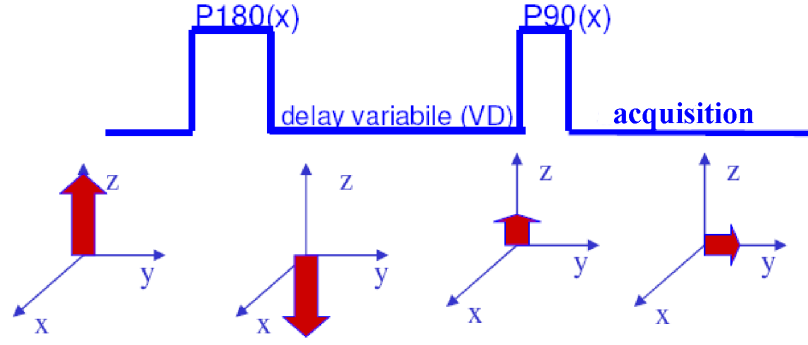
FIGURE 2.16: The timing diagram for the inversion recovery pulse sequence. Varying the delay between the two RF pulses, on e obtain a function whose time decay is just T_1 as shown in figure 2.17.
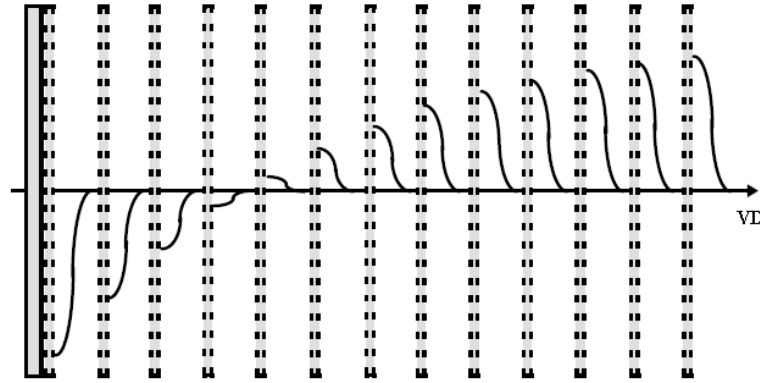

FIGURE 2.17: The inversion recovery experiment for the determination of T_1. As the time between the two RF pulses (VD) increases, the signal, initially negative, approaches the value that would have been observed after the sole application of a $\pi/2$ pulse.

2.4   Pulsed Field Gradient NMR and diffusion

The use of magnetic field gradients allows diffusion to be added to the standard NMR observables of chemical shifts and relaxation times (i.e., longitudinal or T_1; transverse or T_2) [168–170]. As an important application, gradient-based diffusion measurements have been found to have clinical utility in NMR imaging studies [165].

   If in addition to $\vec{B} = B_0\hat{z}$ there is a spatially dependent magnetic field gradient $\vec{g}$ (T·m^{-1}), the Larmor precession frequency ω_0 of the spin ensemble immersed in $\vec{B}$ becomes spatially dependent

$$\omega_{\text{eff}}(\vec{r}) = \omega_0 + \gamma(\vec{g} \cdot \vec{r}) \tag{2.57}$$

where $\vec{g}$ is defined as the *grad* of the field component parallel to $\vec{B}$, i.e.,

$$\vec{g} = \nabla\vec{B} = \frac{\partial B_z}{\partial x}\vec{i} + \frac{\partial B_z}{\partial y}\vec{j} + \frac{\partial B_z}{\partial z}\vec{k} \tag{2.58}$$

where $\vec{i}$, $\vec{j}$, and $\vec{k}$ are unit vectors of the laboratory frame of reference. The important point is that if a homogeneous gradient of known magnitude is imposed throughout the sample, the Larmor frequency becomes a spatial label with respect to the direction of the gradient.

A very used approach to measure diffusion with magnetic field gradients is to use a simple modification [172] of the Hahn spin-echo pulse sequence [173, 174], in which equal rectangular gradient pulses of duration δ are inserted into each τ period (the "Stejskal and Tanner sequence" or " Pulsed Field Gradient (PFG) sequence") [169, 170].
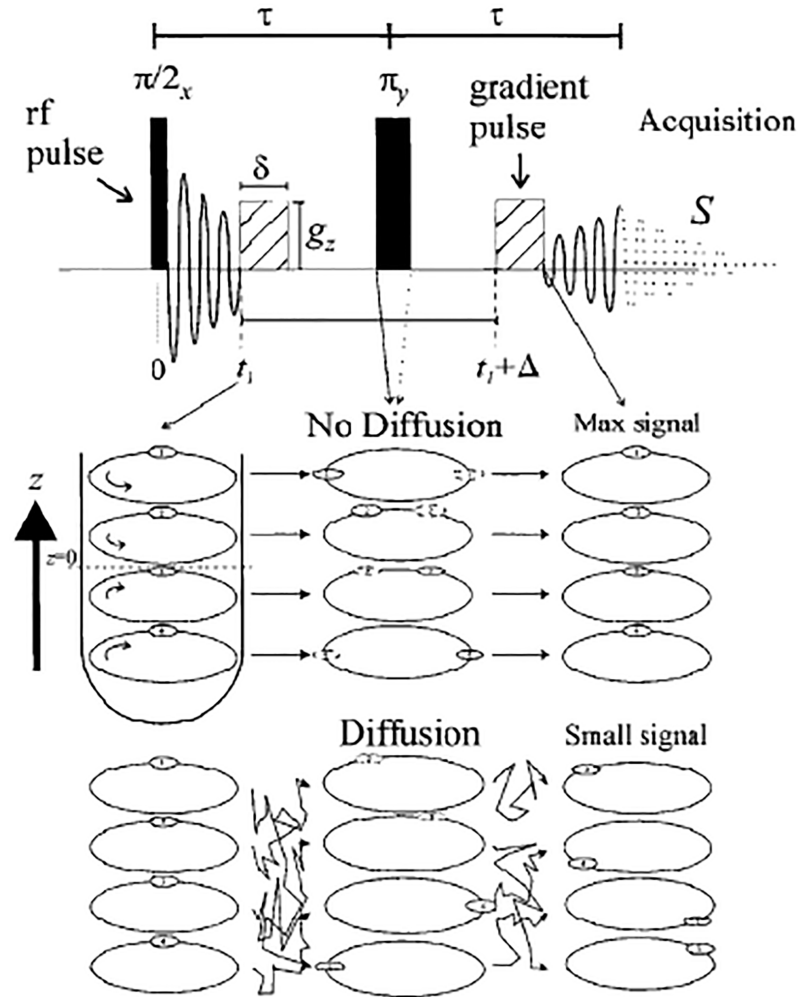

FIGURE 2.18: Hahn spin-echo pulse sequence with a rectangular gradient pulse of duration δ and magnitude g inserted into each τ delay. The separation between the leading edges of the gradient pulses is denoted by Δ. The second half of the echo is digitized (denoted by dots) and used as the free induction decay (FID). Figure adapted from [175].

In detail, a $\pi/2$ RF pulse is applied which projects the macroscopic magnetization from the z-axis onto the (x,y) plane (i.e., perpendicular to the static field). In the absence of diffusion, the effect of the first gradient pulse, denoted by the curved arrows in the first phase diagram, is to create a magnetization helix (i.e., the solid ellipses in the center phase diagram) with a pitch of $2\pi(\gamma\delta g)$. The π pulse reverses the sign of the phase angle (i.e., the dotted ellipses in the centre phase diagram), and thus, after the second

gradient pulse, the helix is unwound and all spins are in phase, which gives a maximum echo signal. In the presence of diffusion, the winding and unwinding of the helix are scrambled by the diffusion process, resulting in a distribution of phases. Larger diffusion would be reflected by poorer refocusing of the spins, and consequently by a smaller echo signal.

As shown in [175], during the first τ period at time t_1, a gradient pulse of duration δ and magnitude g is applied so that at the end of the first τ period, spin i experiences a phase shift,

$$\phi_i(\tau) = \underbrace{\gamma B_0 \tau}_{static\ field} + \underbrace{\gamma g \int_{t_1}^{t_1+\delta} z_i(t)dt}_{applied\ gradient} \tag{2.59}$$

where the first term is the phase shift due to the main field, and the second one is due to the applied gradient with a constant amplitude g. At the end of the first τ period, a π RF pulse is applied that has the effect of reversing the sign of the precession (i.e., the sign of the phase angle) or, equivalently, the sign of the applied gradients and static field[27]. At time $t_1 + \Delta$, a second gradient pulse of equal magnitude and duration is applied (the π pulse has the effect of changing the sign of the first gradient pulse; this leads to the idea of an "effective" field gradient). If the spins have not undergone any translational motion with respect to the z-axis, the effects of the two applied gradient pulses cancel and all spins refocus. However, if the spins have moved, the degree of dephasing due to the applied gradient is proportional to the displacement in the direction of the gradient (i.e., the z-direction) in the interval Δ (i.e., the duration between the leading edges of the gradient pulses, also known as "observation" or "diffusion" time). Thus, at the end of the echo sequence, the total phase shift of spin i relative to $z = 0$ is given by

$$\phi_i(2\tau) = \underbrace{\left\{ \gamma B_0 \tau + \gamma g \int_{t_1}^{t_1+\delta} z_i(t)dt \right\}}_{first\ \tau\ period} - \underbrace{\left\{ \gamma B_0 \tau + \gamma g \int_{t_1+\Delta}^{t_1+\Delta+\delta} z_i(t')dt' \right\}}_{second\ \tau\ period} =$$

$$= \gamma g \left\{ \int_{t_1}^{t_1+\delta} z_i(t)dt - \int_{t_1+\Delta}^{t_1+\Delta+\delta} z_i(t')dt' \right\} \tag{2.60}$$

Dealing with an ensemble of nuclei (with different initial and final positions), the normalized intensity (i.e., an attenuation) of the echo signal at $t = 2\tau$, that is $S_{FT}(2\tau)$, is given by

$$S_{FT}(2\tau) = S_{FT}(2\tau)_{g=0} \int_{-\infty}^{\infty} P_{phase}(\phi, 2\tau) \exp(i\phi)d\phi \tag{2.61}$$

where $S_{FT}(2\tau)_{g=0}$ is the signal (i.e., resultant magnetic moment) in the absence of a field gradient and $P_{phase}(\phi, 2\tau)$ is the (relative) phase-distribution function [174].

In the absence of diffusion and/or gradients, we would have the signal at $t = 2\tau$ equal to

$$S_{FT}(2\tau)_{g=0} = S_{FT}(0) \exp\left(-\frac{2\pi}{T_2}\right) \tag{2.62}$$

---

[27]The π pulse applied after the $\pi/2$ one, has the property of refocusing chemical shifts and the frequency dispersion due to the residual B_0 inhomogeneity and susceptibility effects in heterogeneous samples (e.g., the magnetic susceptibility changes with spin position).

where $S(0)$ is the signal without attenuation due to relaxation that would be observed immediately after the $\pi/2$ pulse. In the presence of diffusion and gradient pulses, the attenuation due to relaxation and the attenuation due to diffusion and the applied gradient pulses are independent, so we can write

$$S_{FT}(2\tau) = S_{FT}(0) \underbrace{\exp\left(-\frac{2\pi}{T_2}\right)}_{relaxation\ attenuation} \underbrace{\Psi(\delta, g, \Delta, D)}_{diffusion\ attenuation} \tag{2.63}$$

where $\Psi(\delta, g, \Delta, D)$ is a function that represents the attenuation due to diffusion (e.g., compare equation 2.63 with equation 2.61). Thus, if the PFG measurement is performed whilst keeping τ constant, it is possible to separate the two contributions. Hence, by dividing equation 2.63 by equation 2.62, we normalize out the attenuation due to relaxation, leaving only the attenuation due to diffusion,

$$E = \frac{S_{FT}(2\tau)}{S_{FT}(2\tau)_{g=0}} = \Psi(\delta, g, \Delta, D) \tag{2.64}$$

Starting from the Bloch equation including the effect of isotropic diffusion for the magnetization, for the echo attenuation one can easily obtain

$$E = \Psi(\delta, g, \Delta, D) = \exp\left[-\gamma^2 g^2 \delta^2 D(\Delta - \delta/3)\right] \tag{2.65}$$

The term $\delta/3$ accounts for the finite width of the gradient pulse. Equation 2.65 is not a function of t_1, thus the placement of the gradient pulses in the sequence has no consequence; for example, there is no requirement that the gradient pulses be symmetrically placed around the π pulse. It is evident that increasing any of three parameters (δ, g, Δ) will lead to increased signal attenuation, thus this is a means of measuring diffusion.

The Pulsed Field Gradient Stimulated Echo technique (PFGSTE) is a modified version of the PFG sequence previously described [169, 170]. This procedure permits the study of the time evolution of the diffusion coefficient and it is often used in macromolecular systems, such as proteins. Figure 2.19 displays a diagram of the sequence. Here, the refocusing π RF-pulse, shown in figure 2.18, is replaced by two $\pi/2$ RF-pulses separated by a time interval Δ. In details, a first 90° pulse excites the magnetization, that is then phase dispersed by a magnetic field gradient pulse. Therefore, a second 90° RF pulse is applied that moves half of the dispersed magnetization onto the z-axis. After a delay that allows diffusion to occur, a third 90° radiofrequency pulse returns the dispersed magnetization to the (x,y) plane where a final magnetic field gradient pulse refocuses it to yield a signal whose intensity is dependent on the diffusion rate [169, 170, 176].

Other methods to relate diffusion to the attenuation of the echo signal and to the experimental parameters in the PFG NMR experiment consist in using the Gaussian phase distribution (GPD) approximation and the short gradient pulse (SGP) approximation (described in details in [175] and/or [168]). Note that the use of these approaches allows to solve the diffusion equation subject to the correct boundary conditions that otherwise has mathematically intractable solutions . The difference in the GPD and SGP methods consists in the comparison between experimental parameters, e.g., δ and Δ. For example, the SGP approximation is strictly valid for infinitely small δ with respect Δ such that motion during the gradient pulse can be neglected, in contrast to the GPD approach.

In homogeneous system, the diffusion propagator [168, 169, 175, 177] can be assumed Gaussian and the echo attenuation, obtained from the PFGSTE technique within the Short Gradient Pulse (SGP) limit [168, 175, 178], can be described using the following equation
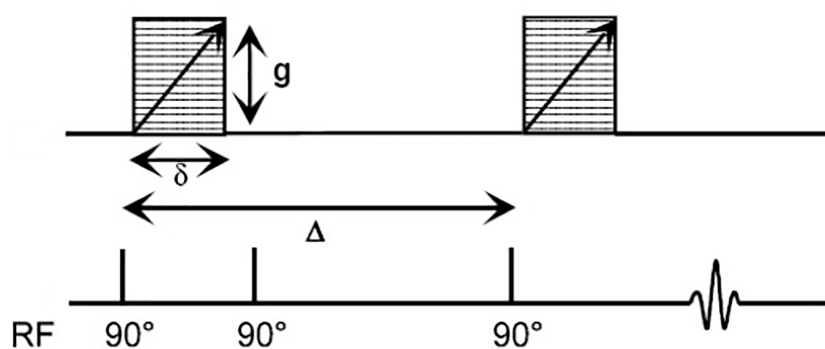
FIGURE 2.19: Diagram of the PFGSTE pulse sequence. RF indicates the radiofrequency, Δ is the distance between two gradient pulses, or the diffusion time, δ and g are the duration and the magnitude of the gradient pulse, respectively.

$$\Psi(\Delta) = \Psi_0 \, exp[-(2\pi q)^2 \langle z^2(\Delta)\rangle /2] = \Psi_0 \, exp[-(\gamma \delta g)^2 D\Delta)] \qquad (2.66)$$

in which the quantity $\gamma \delta g$ is the "NMR generalized" scattering vector q and $\langle z^2(\Delta)\rangle = 2D\Delta$ is the mean-squared displacement (MSD) along the z-axis.

Instead, in heterogeneous media, the diffusion propagator can no longer be considered Gaussian and the echo can be characterized, for example, by a stretched exponential [54, 178]. In general, higher order moments will then have to be considered in equation 2.66, and this will make complicate to achieve informations about the studied sample. However, to be able to analyze the PFG NMR data from heterogeneous systems, it is possible to consider the second cumulant approximation [169]. Using this approach, the initial decay of equation 2.66 is most dependent on the lowest order of g (g^2 for a Gaussian propagator). As the contribution due to higher orders of g is much smaller than the contribution obtained from the second order, the initial decay should reflect a Gaussian distribution [177]. In this situation, as reported in ref. [179], the spin echo attenuation is a polynomial of even powers in q multiplied by even cumulants and, precisely, Ψ is the second power in q multiplied by the mean squared deviations from the mean displacement.

2.5 High-Resolution Magic Angle Spinning

High-resolution NMR is extensively used in structural study of organic molecules, in fact it is one of the methods required for the characterization of any organic compound, such as biological macromolecules [167, 170].

An essential requirement to obtain HR NMR spectra is the sufficient molecular mobility. This condition is usually satisfied in non viscous liquids, therefore all liquids can be analyzed without any treatment. Semi-solid samples with sufficient molecular mobility can be studied without any treatment by high-resolution magic angle spinning (HR-MAS) spectroscopy. In fact, not liquid samples are characterized by strong anisotropic interactions that provoke line-broadening effects also at high magnetic fields, limiting the NMR spectral resolution and sensitivity. These phenomena are mainly due to (i) a non-uniform magnetization, (ii) the spins dipolar coupling, and (iii) the chemical-shift anisotropy (CSA) effect. In this frames, the HR-MAS technique has been developed to

reduce the two main line-broadening mechanisms that are important in acquiring spectra of a tissue or cell sample, namely dipolar coupling and heterogeneous isotropic susceptibility [180]. The local magnetic field created by these latter effects mentioned above changes from position to position as well as the resonance frequency. This causes a frequency distribution for each resonance frequency that depends on the intensity of the two effects inducing the line-broadening of NMR peaks. To bypass this situation, in HR-MAS technique, the sample is put in a rotor (see figure 2.20a), and spun at the magic angle of about 54.74° by few thousands of Hertz resulting in highly resolved NMR spectra [181, 182]. Today, rotors can spin at frequencies between about 1 and 100 kHz: at higher frequencies the signal results more enhanced and with higher resolution. To prove what has just been said, for example, figure 2.20b shows the HR-MAS spectra of a plant leaf acquired on a 400 MHz spectrometer with spinning frequencies ranging from 6 to 19 kHz: it is well evident that the resolution and the intensity of the signal increases with the spinning frequency.
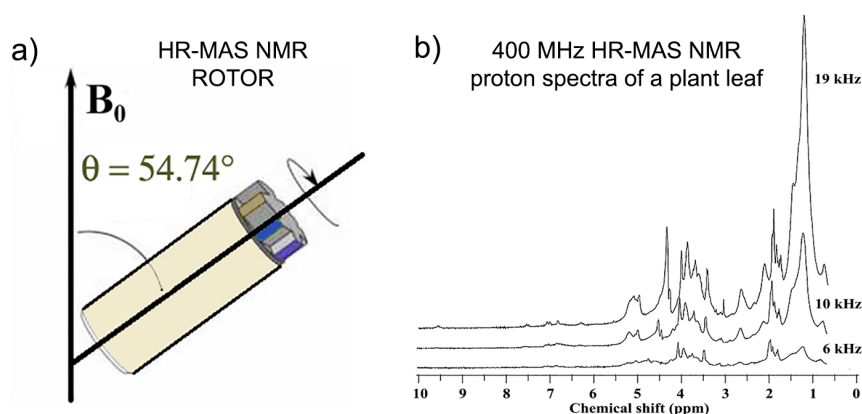

FIGURE 2.20: (a) The rotor used for the HR-MAS spectroscopy measurements in which the sample is inserted and spun at the magic angle of about 54.74° allowing to achieve an highly resolved NMR spectrum. In fact, in this way, dipolar coupling and heterogeneous isotropic susceptibility effects inducing the line-broadening of NMR peaks are avoided. (b) HR-MAS NMR spectra of a plant leaf obtained for different spinning frequency of the rotor. Note that at higher frequencies the signal results more enhanced and with higher resolution. Figure adapted from [183]

Therefore, HR-MAS maintains, even for semi-solid samples, the high instrumental sensitivity and precision of liquid state NMR, permitting to obtain a large number of information on the investigated sample by means of a single experiment. In addition, HR-MAS allows to perform measurements with a minimal quantity of sample (a few μl) that are sufficient to acquire high-resolution spectra of heterogeneous samples such as cells and/or tissues, obtaining a very good signal/noise ratio. Figure 2.21 shows a comparison between a standard NMR spectrum and an HR-MAS one.

Therefore, HR-MAS NMR can be considered a composite technique between solid-state NMR and standar solution state NMR. In fact, it uses the magic angle spinning approach [181] including bidimensional pulse sequences that characterize the classical solution NMR experiments.

As a matter of fact, HR-MAS quickly provides a broad range of information directly from the material under investigation and it has received great attention in several field,
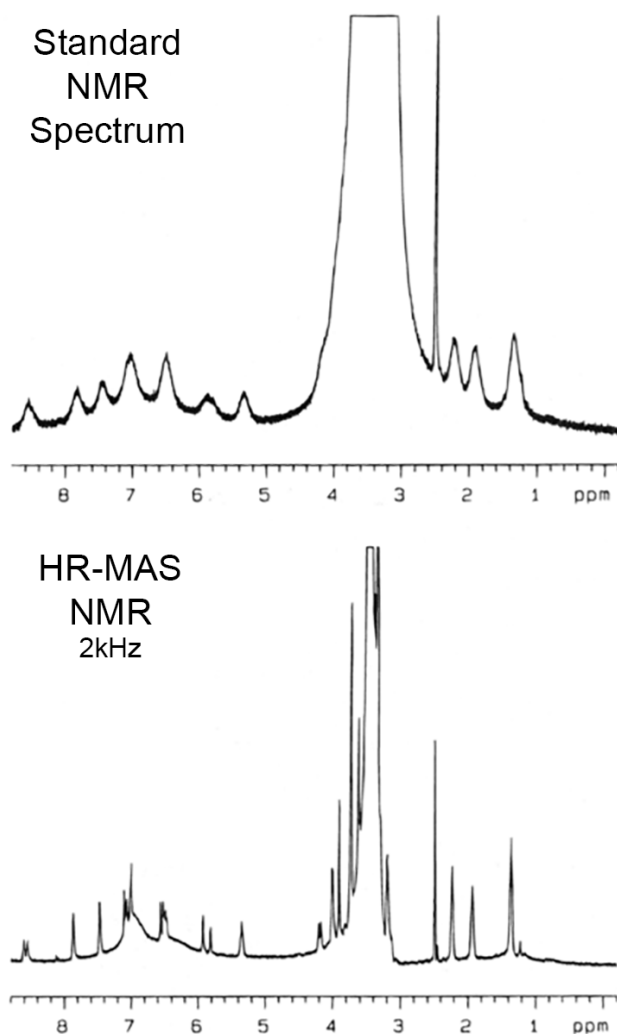
FIGURE 2.21: A comparison between standard NMR and HR-MAS measurements on leaf plants. Note that how the use of HR-MAS technique improves the signal furnishing a more enhanced and with higher resolution spectrum (bottom) with respect of the standard NMR one (top). Figure adapted from [184]

e.g, the biomedical area, demonstrating for example the ability of this technique to discriminate between malignant and benign disease [185, 186], or in the food science and metabolomics [187].

Chapter 3

Results and discussion

3.1 Water-methanol Solution

The dynamics of the water-methanol mixture have been studied by means of a Bruker AVANCE NMR spectrometer operating at 700MHz ^{1}H resonance frequency (see Section 2.2). In these experiments, we have measured the NMR self-diffusion coefficient D and, so, the relaxation time t_α as functions of the water molar fraction X_W and temperature in the range $160 < T < 335$ K. In particular, in our study, we compared our results with data from the literature, examining the evolution of the indicated transport parameters at a fixed T as a function of X_W and evaluating how they differ from those in an ideal mixture in which there are no interacting molecules.

3.1.1 Relaxation time

Taking advantage of the high magnetic field of our instrument, we were able to perform very accurate measurements of the self-diffusion coefficient D.

In particular, we calculate the corresponding relaxation time using the Debye-Stokes-Einstein (DSE) equation that relates the diffusion with the relaxation time.

Figure 3.1 shows an Arrhenius plot of the relaxation times t_α versus $1000/T$ in pure bulk water and methanol, and of many solutions in the range $0.1 < X_W < 0.7$.
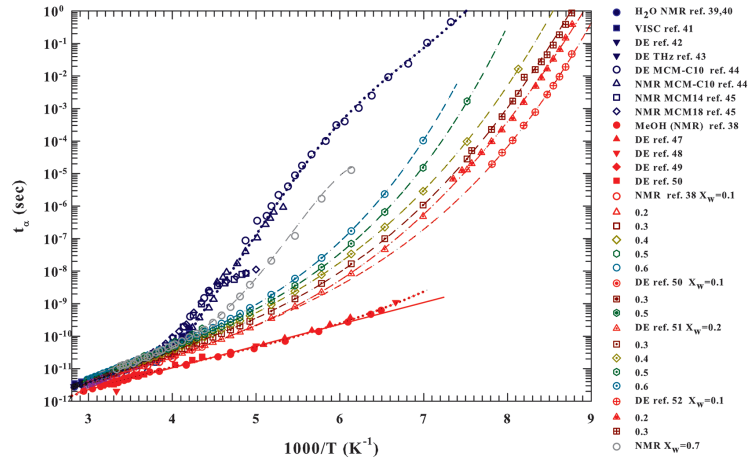

FIGURE 3.1: The relaxation time t_α for water-methanol solution in the range $0 < X_W < 1$ illustrated in an Arrhenius plot. The data come out from our own experiments and from the literature considering mostly DE and NMR experiments. Figure taken with permission from [84]. Note that all the references indicated in the legend refer to the original work.

The reported data come out from our experiments and literature. Note that all the references indicated in the legend of the figure refer to the original work [84]. In particular, we show (i) bulk and confined water data, including NMR, viscosity, DE relaxation and THz experiments; (ii) pure methanol from NMR and DE measurements; and (iii) the water-methanol mixture indicated in terms of X_W. In the latter case, for NMR, we have $X_W = 0.1, 0.2, 0.3, 0.4, 0.5$, and 0.6. The NMR data measured at $X_W = 0.7$ are acquired by means of the Pulsed Field Gradient Stimulated Echo technique (^{1}H-PFGSTE), already described in 2.4..

The red straight line that crosses the pure methanol data in figure 3.1 displays that this liquid is a strong glass-former over a very wide T range, a marked different behavior from that in pure bulk water as already stated in 1.2.1. Furthermore, figure 3.1 shows that the relaxation time for water t_α^W goes beyond the values of methanol t_α^{MeOH} for all considered temperatures. In particular, at the different investigated concentrations of solutions, t_α exhibits a fragile glass-forming behavior that is reproduced using a scaling law fitting of the corresponding data (dashed curves). For water and methanol, it is obtained using simple data smoothing (dotted lines). For the scaling law, we use the ideal Mode-Coupling-Theory (MCT)

$$t_\alpha \propto \left| \frac{T - T_c}{T_c} \right|^\varphi \tag{3.1}$$

where T_c denotes the "critical" MCT temperature and the exponent φ is not universal [188]. Anyway, although the MCT scaling law is used to investigate the behavior of glass-forming materials, all the obtained curves are shown in the figure only as a guide for the eye.

Figure 3.2 displays that there is a superposition between data of many different molar fractions in the high temperature region ($T \gtrsim 238$ K).
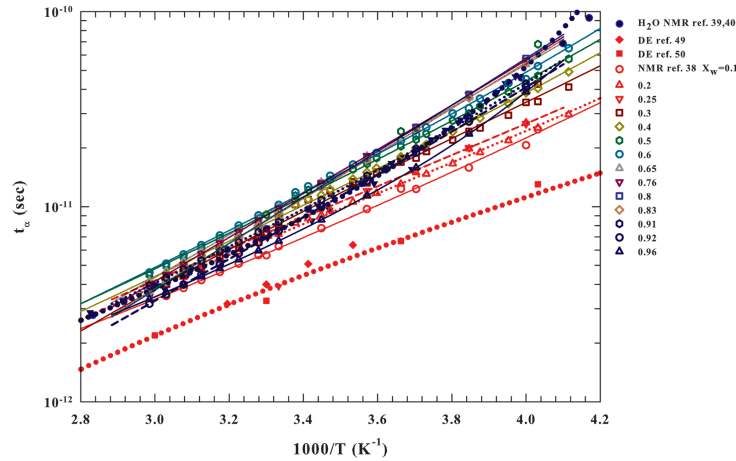
FIGURE 3.2: In the high temperature region, $1000/T \lesssim 4.2$ ($T \gtrsim 238$ K), the t_α of many different molar fractions exceeds that of water. More NMR data with respect of figure 3.1 are reported to highlight such a situation. Figure taken with permission from [84]. Note that all the references indicated in the legend refer to the original work.

The curves interpolating the pure water and methanol relaxation time data are symbolized as dots. In this way, it is well evident that the solution data often exceed the bulk water data, in contrast with the low T regime (see figure 3.1) in which t_α^W always exceeds the values of the relaxation time of pure methanol and solutions. Furthermore,

even though figure 3.2 showed more NMR data than figure 3.1, there is a change in the data-spread (t_α^W - t_α^{MeOH}) at fixed temperature. At $T \simeq 300$ K, the change is less than an order of magnitude, but at $T \simeq 150$ K, it is seven orders of magnitude, indicating a dramatic change in the solution dynamics. To further examine this, we plot the relaxation time t_α at a fixed temperature as a function of X_W.

Figure 3.3a shows t_α versus X_W in a log-linear scale for temperatures $163 < T < 300$ K, bringing to light two distinct behaviors at high and low temperatures.
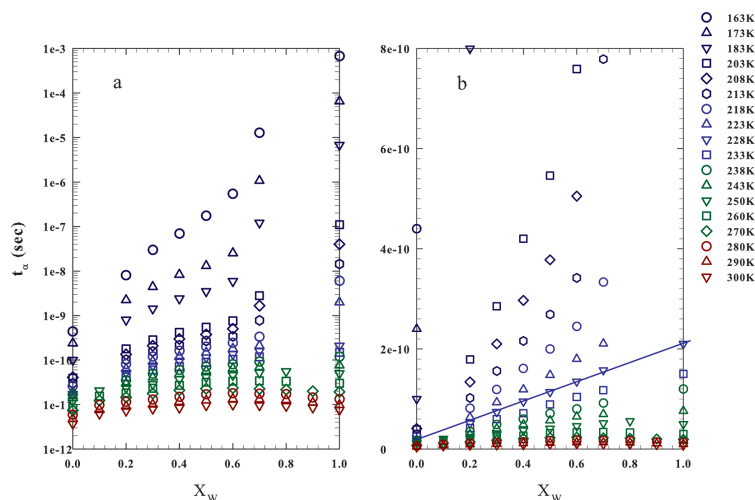

FIGURE 3.3: The relaxation times of the water-methanol solutions, t_α, at a fixed temperature, as a function of the water molar fraction X_W. Data are reported (left) in a log-lin scale and (right) in a lin-lin representation for the temperatures in the range $163 < T < 300$ K. Two different behaviors in the low and high T regimes are evident from the data in the log-lin scale; whereas the low-T region is characterized by a marked concavity in the t_α data, conversely in the high-T regime, the data show a maximum around $X_W \simeq 0.5$. This is more clear in the lin-lin data representation, where a change in the data curvature, from concave to convex, takes place just near $T = 228$ K, where, within the experimental error, a nearly linear behavior (typical of an ideal mixture) can be observed. Figure taken with permission from [84].

In particular, the low-T region exhibits a marked concavity in the t_α data and the relaxation time data show a maximum at the high-T around $X_W \simeq 0.5$. Figure 3.3b displays a linear-linear graph in which the curvature of the data changes from concave to convex near $T = 228$ K. At this temperature, the relaxation time behavior is approximately linear within the error, so the solution acts as an ideal mixture in which molecular interactions have a minimal effect on the system dynamics.

We investigate the t_α peculiarities in water-methanol solutions by weighing them with the linear behavior of an ideal mixture at all the studied temperatures and at different water molar fractions. To do this, we compare the measured values of t_α^W and t_α^{MeOH} with a rectilinear line at a fixed T and then subtract the mixture values at the different concentrations from the straight line ones at the same t_α^W. This produces the Δt_α values[28]. In particular, we can obtain useful informations by a simple consideration, derived by a care inspection of the data of figure 3.3a, on the distinct behaviors shown by the relaxation

---

[28]This procedure is the one traditionally used to reveal the interaction effects among the solution molecules with different structures and hydrophilic and hydrophobic moieties [89, 92, 94, 114, 118].

time of the two opposite composition phases. In fact, whereas t_α changes regularly for $X_W < 0.6$, it presents a more complex behavior when we have a greater amount of water.

Figure 3.4 reports three separate panels in which Δt_α is a linear function of X_W, (a) $T = 163$ K and 173 K, (b) $T = 193$ K and 203 K, and (c) $T = 208$ K, 213 K, and 218 K. Note that the Δt_α values are negative for all T, but their maximum value decreases as T increases. From 163 K to 218 K, the Δt_α values vary by four orders of magnitude.
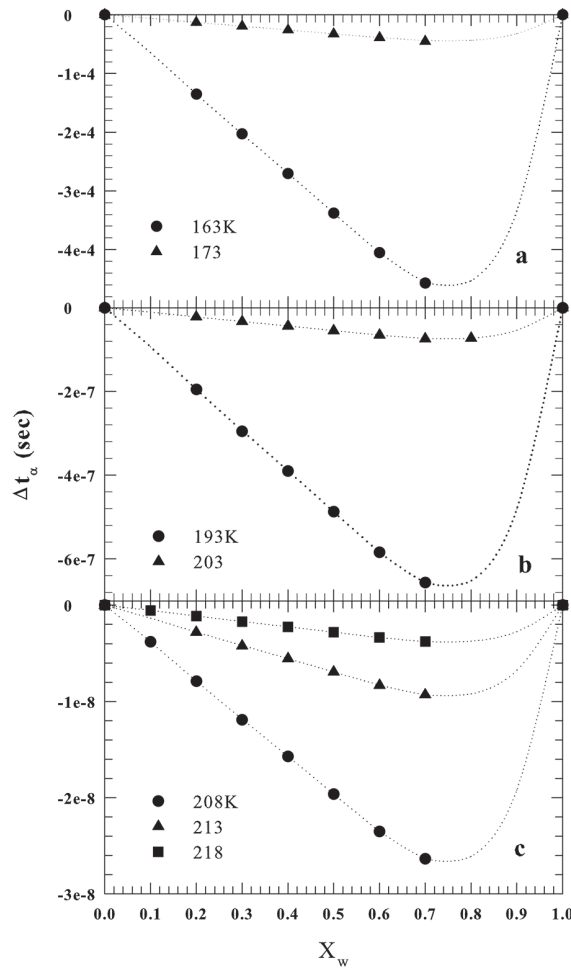

FIGURE 3.4: The differences Δt_α between the experimental relaxation time data and those of the ideal mixture are displayed in three linear-scale graphs as a function of X_W, (top,a) $T = 163$ K and 173 K, (middle,b) $T = 193$ K and 203 K, and (bottom,c) $T = 208$ K, 213 K, and 218 K. From the figure, it can be noticed that the achieved Δt_α are negative for all the considered T, but their maximum value decreases on increasing the temperature; the overall variation in Δt_α is from 163 to 218 K more than four orders of magnitude. Figure taken with permission from [84].

Figure 3.5 illustrates a linear plot with respect of X_W of the results in the range 296 $< T <$ 335 K. Here, the Δt_α values are positive, i.e., the solution relaxation time $t_\alpha > t_\alpha^W$ value raises as T decreases.

Thus, the dynamics of the system slow down, and in the low temperature regime inside the "No Man's Land", the situation is overturned, i.e., the water–methanol interactions accelerate in comparison with the case of an ideal solution. Note that figures 3.4
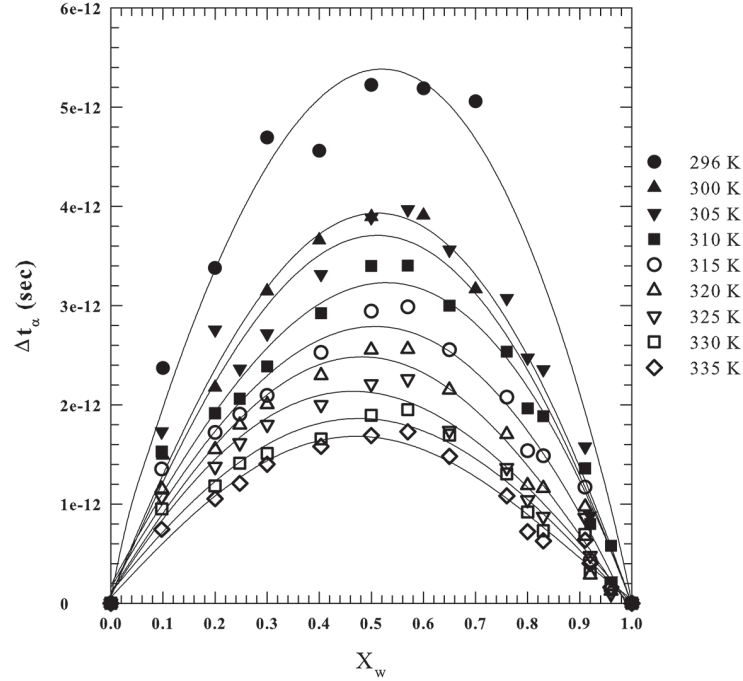
FIGURE 3.5: A linear plot of the obtained Δt_α in the range $296 < T <$ 335 K. As it can be noticed, the Δt_α values are positive and increase by decreasing temperature. Figure taken with permission from [84].

and 3.5 evidence that the positive excess Δt_α for all T is located in the range $0.5 < X_W <$ 0.6 and the trend increases as T decreases. On the contrary, in the low-T regime, the negative excess is located at $X_W \simeq 0.75$.

The results for $T > 223$ K are consistent with the water-methanol structural behavior studied bye means of soft X-ray absorption spectroscopy [119]. As stated previously (see paragraph 1.2.1), this XAS experiment reveals that, at ambient temperature, the local structure is produced by the hydrophobic interaction of the methyl group, as shown in our high-T region data. Furthermore, this situation can be also seen studying the proton spin-lattice relaxation times T_1 measured using NMR in the range $250 < T < 300$ K [116] (note that $T_1 \propto$ D[189]). In particular, the T_1 data show the same decreasing behavior seen in the t_α data when T is reduced (see figure 3.3).

As previously shown in paragraph 1.1.5, $T_L \simeq 225$ K is both the temperature of the fragile-to-strong dynamic crossover and the Widom line temperature, which has maxima in the thermodynamic response functions in the (P,T) plane [4, 78] (at 1 bar, $T_L = T_W$), and, at the same time, it is the locus where the relative populations of the LDL and HDL species become the same reducing the temperature. Note that the domains at higher T are dominated by HDL and the deep water supercooled regime by the LDL. In particular, if we decrease T in the HDL phase, when we reach the temperature of 320 K, identified as T^*, an HB network begins to form [190], the HDL population decreases, and the LDL population increases up to T_L becoming dominant [191]. At the "magic" temperature T^*, the bulk water compressibility $\kappa_T(T)$ has a minimum unaffected by the pressure and all the curves referring to the coefficient of thermal expansion $\alpha_P(T)$ measured at different pressures cross [190]. These structural observations obtained by means of the XAS experiment at ambient temperature show that the HB tetrahedral structure plays an important role in water-methanol mixtures. When the number of water molecules exceeds those of methanol in the concentration, i.e., $0.7 < X_W < 0.95$, the molecules

of MeOH are separately embedded in dominant 3D HB water networks, and reducing T increases the HB relaxation time by many orders of magnitude, similarly to that observed in H_2O (see figure 3.1). This is the cause of (i) the Δt_α behavior observed in the low temperature regime, and (ii) the hypothetical concentration dependence of the Widom line temperature (T_W). Anyway, in the high-T regime, methyl hydrophobicity is the dominant interaction.

3.2 Water-lysozyme system

As already stated, the role that water plays in determining the structure, the dynamics and the biological activity of proteins is of primary importance. In our studies, we investigate several aspects and peculiarities of the interaction between water and lysozyme by means of a Bruker AVANCE NMR spectrometer operating at 700MHz ^{1}H resonance frequency (see Section 2.2). For example, the performed experiments show that (i) the properties of water and the effect of its HB coupling with the hydrophilic moieties of lysozyme govern the regime of protein activity [156]; (ii) the measured fragile-to-strong dynamic crossover temperature is unaffected by the hydration level and that the first hydration shell remains liquid at all hydrations, even at the lowest temperature [13]; (iii) the kinetics of the lysozyme folding-unfolding process is controlled by the dynamics of the water molecules in the first hydration shell [157] and (iv) this process can be described by using the free-energy-landscape model that explains the important role of water in the protein configurational stability, as well as hydrogen bonding [12]; (v) the temperature T^* represents the "border" for water behavior from a normal fluid to an anomalous, complex liquid, changing its interaction with lysozyme and, so, the dynamics of the system from a sub-diffusive state ($T < T^*$) to a super-diffusive one ($T > T^*$) [158].

3.2.1 Chemical shift

We focus on the region of thermal denaturation of hydrated lysozyme by studying the chemical shift σ and following the evolution of the NMR spectra for 298 K $< T <$ 366 K.

Detailed proton NMR experiments were performed to get precise insight of the unfolding process of lysozyme at atmospheric pressure by using a 700 MHz Bruker Avance spectrometer equipped with the High-Resolution Magic Angle Spinning (HR-MAS) probe (see section 2.5 for further details). The investigated samples were placed in a 50 μl rotor and spun at 4000 Hz at the magic angle to amplify the spectral resolution. In our experimental setup, the temperature of the sample was regulated by a cold N_2 flow and a heating element, calibrated by using the frequency shift between ethylene glycol peaks. The duration of the hard pulse was of 8 μs with a relative attenuation of 3 dB; the spectral width was 10 kHz, the acquisition time 2.9 s, the points in the time domain 64k, the number of transient 128 and the relaxation time 2 s for a total time of about 10 min per experiment. All the acquired spectra were processed by using the Bruker software Xwinnmr version 3.5.

The obtained NMR spectra of hydrated proteins allow to separate the different chemical groups of protein and water studying them separately. The pile of HR-MAS NMR spectra plot for hydrated lysozyme (hydration level: $h = 0.3$) achieved in the high-T regime are reported in figure 3.6. We focused on the unfolding process starting the measurement at 298 K and reaching 366 K with steps of 2 K.

The intense signal at the center of the spectra refers to hydration water protons and is more than four orders of magnitude larger than the other contributions. Note that all the peaks linked to the protons of lysozyme appear at $\approx$ 320 K with the exception of the peak
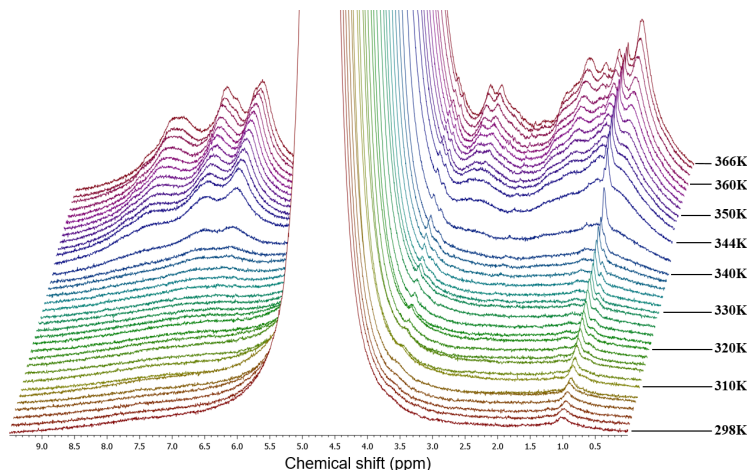
FIGURE 3.6: NMR spectra for hydrated lysozyme ($h = 0.3$) in the high-T region measured by means of the HR-MAS set-up. Figure used with permission from [156].

at 1.0 ppm (assigned to the methyl functional group). This is a well-evident indication that the protons of lysozyme are rigid (side chains of the protein are not flexible) on the NMR timescale at this hydration level up to ≈ 320 K becoming increasingly mobile with T. This temperature is on the border between the native state and the intermediate region where the unfolding process starts [137]. In particular, as shown in figure 3.6, the temperature of ≈ 344 K indicates the point at which the unfolding process is no longer reversible and all protein contributions are clearly visible with an abruptly increasing of the magnetization signal. Furthermore, the decreasing of their peak width reflects the increasing protein mobility due to the almost complete hydrogen bonding breakage. In the frame of HB, our data suggest that the HB coupling between hydration water and protein hydrophilic groups is crucial in triggering the main mechanisms that define the enzymatic activity of proteins.

3.2.2 Diffusion and relaxation time

As discussed in the first chapter (see 1.2.2) and shown in 3.2.1, the reversible folding-unfolding process and the irreversible denaturation for lysozyme occur at $T_D \approx 346$ K [137, 153, 192], but to clarify the importance of hydration water in protein activity, an investigation inside the supercooled region is also really important [136, 154]. Therefore, we study the self-diffusion $D(T)$ of hydration water by means of ^{1}H-PFGSTE NMR technique using a 700 MHz Bruker Avance NMR spectrometer at ambient pressure across a very large T range, i.e., from the stable water liquid phase to the deeply supercooled regime. In our experiments, we use a powder of lysozyme hydrated at values of h (i.e., the hydration level) in the range between 0.32 and 0.65 according to a precise procedure [136]. As long as the samples reach the desired hydration level h, the dried protein powder is hydrated at 5°C by exposing it to water vapor in a closed chamber. During the measurements, the samples are cooled slowly maintaining a T stability of 0.1 K.

Figure 3.7 displays the measured proton self-diffusion of $D(T)$ data in Arrhenius plots (log D vs $1000/T$) for all the considered hydrations ($h = 0.3, 0.32, 0.37, 0.48, 0.52, 0.61$, and 0.65) and for the bulk water data [58]. Note that the hydration levels of $h = 0.3$, and 0.32 [15] have been studied in the interval $200 < T < 360$ K, instead, the others levels, 0.37, 0.48, 0.52, 0.61 and 0.65 [13] in the T range between 200 and 293 K.
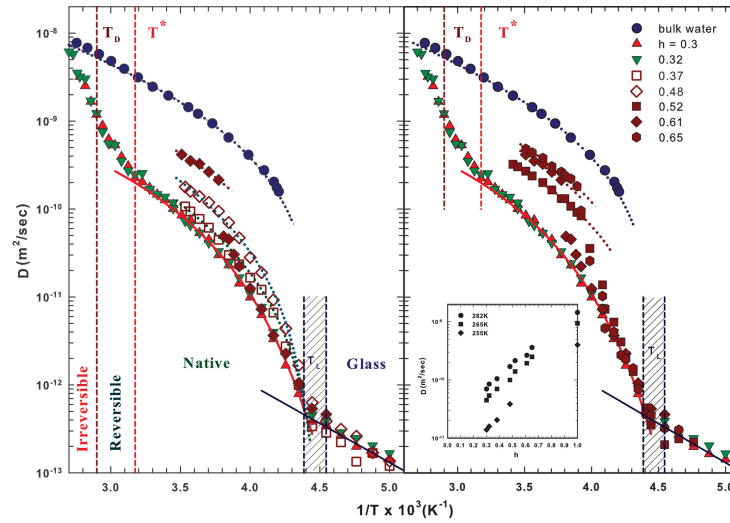
FIGURE 3.7: The measured proton $D(T)$ data are reported in an Arrhenius plot (log D vs $1/T$) for several hydration levels with the data of pure bulk water [58] (blue filled dots). The three protein significant temperatures are indicated: the crossover one T_L, T_D that identifies the folding-unfolding process and T^* that marks the water transition from a normal fluid to the anomalous and complex liquid. The reported curves are the data fits with the ideal mode-coupling-theory scaling law [193, 194]. Finally, the $D(T)$ behavior at $h = 0.61$ shows a marked jump at $T \approx 265$ K as well as the proton self-diffusion data for $h = 0.52$ and 0.65. The inset in the right panel illustrates the hydration dependence of D in the T region where all the protein hydration water remains liquid. Figure used with permission from [13].

Figure 3.7 also shows the already mentioned significant temperatures for water and proteins, T_D, T^* and T_L, including all the important protein phases, i.e., the glass, the native, and the reversible and irreversible unfolding-folding processes.

The data in the left panel of the figure, where the hydration levels of $h = 0.37$, 0.48, and 0.61 are shown, exhibit a peculiar $D(T)$ behavior of the water-lysozyme system for $h = 0.61$ at $1000/T \approx 3.8$ K^{-1} ($T \approx 265$ K) described by a marked "jump" that is dissimilar to that of the remaining hydrations shown in the left panel of the figure. Note that, below the jump temperature, the corresponding D has the same behavior as the hydration water monolayer ($h = 0.3$ and 0.32). This fact indicates that in the lowest T-regime where the "excess" protein hydration water freezes, the first hydration shell remains liquid[29] confirming the findings of calorimetric studies on lysozyme and other proteins that stated that, at the highest hydrations, the excess water can freeze without affecting the liquid water remaining in the first hydration shell [195]. Furthermore, the proton self-diffusion data for $h = 0.52$ and 0.65 in the right side of figure 3.7 also exhibit a similar behavior of the $h = 0.61$ one. The other hydration levels, in contrast, show a super-Arrhenius (SA) or VFT trend similar to that in bulk water; their diffusion data are a function of T in the region of moderate supercooling and are all described using the ideal MCT scaling law $D^{id} \approx |T - T_L|^{\varphi}$ (as a reference, see equation 3.1) [193, 194]

---

[29]Experimentally, the NMR set-up used detects liquid water only, i.e., ice is outside the instrument's resolution. When the liquid water protons are present at the experimental temperature, they are detected and contribute to the NMR spectra, but ice protons only contribute to the spectral background.

(the reported curves in the figure are fits of the data). In particular, the φ values obtained are, for example, 1.8 for bulk H_2O, 2.1 for $h = 0.3$ and 0.32.

The measured T_L values for bulk water and for lysozyme at the several hydrations are, within the error bars, the same $T_L = 225 \pm 5$ K value (e.g., 228 K for the bulk water value [52], 220 K for $h = 0.3$ and 0.32, 222 K for $h = 0.37$, and 224 K for $h = 0.48$). In particular, our results are (within the experimental error) in agreement with neutron scattering experiments [196, 197]. Therefore, for samples of moderate hydrations ($h = 0.3$, 0.32, 0.37, and 0.48) shown in the left side of figure 3.7, T_L is independent of the protein hydration, but, for values obtained for φ, the observed protein hydration water dynamics are the result of HB interactions between water and the protein side-chains [15, 137]. Note that for $T > T^*$ a continuous evolution is evident for $D(T)$ because of the denaturation process at T_D. This is the case from values of the hydration water to that of pure bulk water, and this indicates a decoupling between the water and the protein [15, 137]. In this frame, if we consider the extended mode-coupling-theory (EMCT) for activated hopping processes [194, 198], where T_L represents the MCT critical T below which the system dynamics are governed by extended clusters, we can explain the observed characteristics of lysozyme hydration water. Figure 3.7 shows that samples with different hydration levels have a single hopping mechanism. This is indicated not only by the same crossover temperature, but also by almost the same Arrhenius activation energy for all hydration levels. To confirmed what it has just been said in the first chapter (see 1.2.2), the results obtained by means of several experiments that study confined water in nanostructures and proteins [76, 136, 152, 154, 191, 196] allow us to suppose that the FSDC in water is caused by an evolution of the HDL to LDL, which supports the hypothesis that the "dynamic" transition in proteins is triggered by their strong HB coupling with the hydration water. The influence of the HBs on the properties of protein hydration water is confirmed even in the right panel of figure 3.7. Here, the inset shows the hydration dependence of the self-diffusion coefficient $D(h)$ at fixed temperatures $T = 255$ K, 265 K, and 282 K on a log-linear scale. The behavior of $D(h)$ in both the normal and supercooled T regions denotes that all the protein hydration water remains liquid. Note that the evolution is approximately T-independent, which reveals that the dynamics of bulk and protein hydration water are closely similar and supports the hypothesis that the physical properties of hydrated proteins are due to the coupling of the hydrophilic side chains with the dynamics of the hydration water.

Another interesting topic to investigate regards the origin of the delay of the dynamics of water within the first hydration shell around the protein surface with respect of those of bulk water [199–201]. Perticaroli et al. [201] measured the retardation coefficient (i.e., the ratio between the relaxation time of hydration water and the relaxation time of bulk water) by means of dielectric spectroscopy obtaining a value of 6–8 at ambient temperature. We performed NMR measurements to evaluate the proton self-diffusion coefficient of lysozyme hydration water at one atmosphere by using the PFGSTE technique with a field gradient value of 1200 Gauss/cm. Figure 3.8 displays the ratio between the self-diffusion coefficient measured in bulk water, D_{bulk}, [58, 59] and in hydrated lysozyme with $h = 0.3$, $D_{\text{hydration}}$, in a log-linear (Arrhenius) plot versus $1000/T$. The ratio was calculated at the same T by interpolating the individual data reported in figure 3.7.

This Arrhenius plot indicates that three variations occur at approximately $T = 277$ K, 316 K, and 342 K. By comparing the behavior of the data reported in figure 3.7, it can be noticed that the observed kink in the ratio derives from changes in the T evolution of the hydration water. Note that the value obtained at ambient conditions is higher than that found by Perticaroli et al. [201].

Increasing the temperature, the first change occurs at $T = 277$ K ($1000/T \approx 3.6$
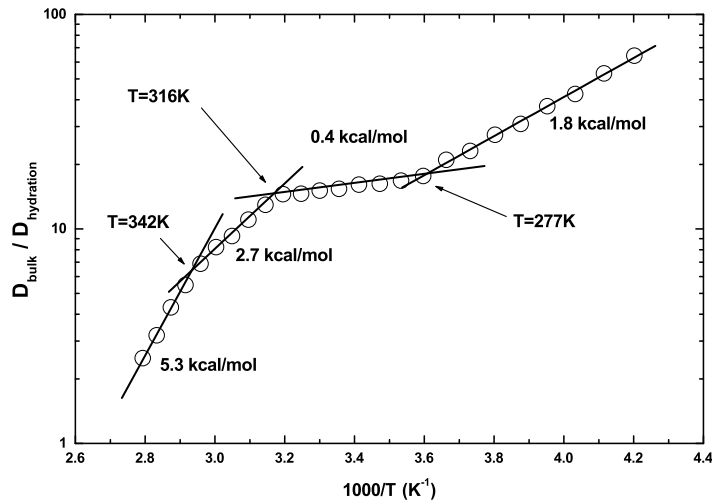
FIGURE 3.8: The ratio between the self-diffusion coefficient measured in bulk water [58, 59] and that measured in hydrated lysozyme ($h = 0.3$) [137] as a function of T, calculated from the interpolation of the data reported in figure 3.7. Three changes are clearly visible in the obtained ratio. Figure used with permission from [157].

K^{-1}) that corresponds to the temperature at which bulk water shows its maximum density anomaly (see the paragraph 1.1.4). When $T < 277$ K, the activation energy is $\approx$ 1.8 kcal/mol which is a typical HB value. In this region, the hydrogen bond network on the protein surface becomes progressively strong and stable. The region between 277 K and 316 K (at which the second change occurs) displays a smaller activation energy ($\approx$ 0.4 kcal/mol). The temperature of $\approx$ 315 K is the already mentioned T^*, the magic temperature above which the HB interaction weakens and water is no longer able to keep the protein in a folded state [190]. In fact, for $T \gtrsim 316$ K, water is no longer a good solvent and the hydrogen bonded network of the first hydration shell begins to crumble and triggers the protein unfolding process. In the next region between 316 K and 342 K, the activation energy is 2.7 kcal/mol and the unfolding process is reversible [137]. For temperature above 342 K, the HB network is disrupted and the structure of the protein is similar to a linear chain of amino acids. So, at the highest activation energy ($\approx$ 5.3 kcal/mol), the unfolding process is irreversible. A complete scheme of these phase regions was already shown in figure 3.7. Note that the ratio between D_{bulk} and $D_{\text{hydration}}$ aims to 1 as happens in bulk water for temperatures approaching the boiling point of the bulk. This denotes that all H_2O molecules are in a bulk condition and free to move.

Considering the proton spin-lattice relaxation time, T_1, calculated in the thermal region of the denaturation ($280 < T < 360$ K) [15, 152], we fit the data with a modified version of equation 2.23, i.e., a weighted double exponential form

$$\frac{M}{M_0} = 1 - 2 \left[P \exp\left(-\frac{t}{T_{1s}}\right) + (1 - P) \exp\left(-\frac{t}{T_{1f}}\right) \right], \quad (3.2)$$

where P is the weight, t the interpulse delay variable, and T_{1s} and T_{1f} are the two relaxing contributions.

The slowest relaxing component T_{1s} has an order of magnitude of seconds and is connected to water protons in the lysozyme hydration shell, instead the fastest component T_{1f} belongs to strongly-bonded protons, e.g., those of internal (or crystallization) water

[15, 152]. Note that the fastest contribution gets progressively smaller at the highest T and it is characterized by a weight less than 10% due to the fact that, when the protein unfolds, the internal water exchanges with the hydration water.

Although protein protons usually contribute to the NMR signal, they are basically static on the NMR observation time scale at low and ambient temperatures, and in particular with low hydration. In fact, even with very HR NMR techniques, protein protons peaks are appreciable only for temperatures higher than the unfolding threshold at low hydration. Furthermore, the magnitude of their intensity is about four orders smaller than that of the water peak [137], so, in this condition, in order to avoid the protein protons contribution, it is possible to consider only the relaxation corresponding just to the water peak.

We study the rotational dynamics to understand the dynamical changes that are responsible of driving protein denaturation. This kind of investigation can be done by estimating the reorientational correlation time using the measured spin-lattice relaxation times and self-diffusion. Assuming that the spin-rotation contribution to the proton relaxation rate is in the order of milliseconds at 360 K [202], and even shorter when below that temperature, only dipolar interactions can be considered for water relaxation and the observed proton relaxation can be written as the sum of inter- and intra-molecular contributions [189, 203] as shown in the following equation

$$\left(\frac{1}{T_1}\right)_{\text{obs}} = \left(\frac{1}{T_1}\right)_{\text{inter}} + \left(\frac{1}{T_1}\right)_{\text{intra}}. \tag{3.3}$$

The intermolecular term can be estimated by using the self-diffusion coefficient D [189, 204] as

$$\left(\frac{1}{T_1}\right)_{\text{inter}} = \frac{\rho_N \pi \gamma^4 \hbar^2}{5aD} \left[1 + 0.233 \left(\frac{b}{a}\right)^2 + 0.15 \left(\frac{b}{a}\right)^4 + \ldots\right] \tag{3.4}$$

where ρ_N is the number density of nuclei, a the molecular hydrodynamic radius, and b the distance of the proton from the center of the molecule. Note that γ and $\hbar$ are the already defined proton gyromagnetic ratio and reduced Planck constant, respectively.

The intra-molecular dipolar contribution is furnished by [164, 203]

$$\left(\frac{1}{T_1}\right)_{\text{intra}} = \frac{3}{10} \frac{\gamma^4 \hbar^2}{r^6} \left[\frac{\tau_\theta}{1 + \omega_0^2 \tau_\theta^2} + \frac{4\tau_\theta}{1 + 4\omega_0^2 \tau_\theta^2}\right] \tag{3.5}$$

where r is the distance between the two protons (hydrogens) in a water molecule, and τ_θ is the reorientational correlation time.

As mentioned by Bloembergen, Purcell, and Pound in their model [205], for small time windows, the correlation function of protein hydration water can be expressed as an exponential. Therefore, in the extreme narrowing limit, i.e., when the product of the resonance frequency of the proton (ω_0) and the reorientational correlation time (τ_θ) is much less than one ($\omega_0 \tau_\theta \ll 1$), equation 3.5 can be written as [189, 203]

$$\left(\frac{1}{T_1}\right)_{\text{intra}} = \frac{3}{2} \frac{\gamma^4 \hbar^2}{r^6} \tau_\theta. \tag{3.6}$$

From this equation, it is well evident that, if we know D and T_1, we can calculate the intra-molecular term and the reorientational correlation time τ_θ. Since we are focusing our investigation on hydration water, we evaluate τ_θ by considering the T_{1s} values (obtained from equation 3.2) and by assuming the constant values $a = 1.38$ Å, $b = 0.92$ Å, and $r = 1.52$ Å[189].

In figure 3.9, we compare τ_θ of lysozyme hydration water measured by NMR ($h = 0.3$, full up-pointing triangles), dielectric spectroscopy ($h = 0.37$, empty squares) [206], and neutron scattering ($h = 0.4$, full squares) [207], with that of emulsified water at 2 kbar (full circles) [203] and bulk water at ambient pressure (empty circles) [59], in a log-lin plot vs the temperature. Note that when T decreases below the temperature of irreversible denaturation, the reorientational correlation time in hydration water is slower than in bulk water, but when $T > 346$ K, the rotational dynamic values raise quickly and look alike those of bulk water. This confirms the previous findings that when $T > 346$ K the network of HBs breaks down and water molecules move freely.
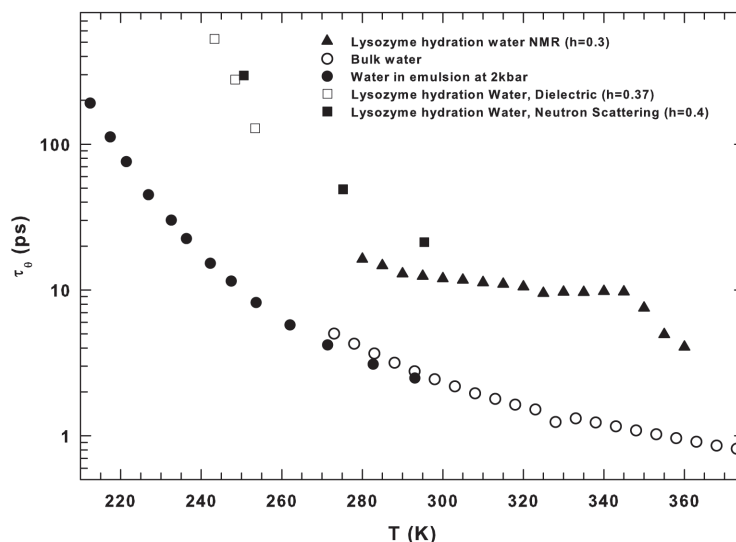

FIGURE 3.9: The reorientational correlation time, τ_θ, of lysozyme hydration water measured by NMR ($h = 0.3$, full up-pointing triangles), dielectric spectroscopy ($h = 0.37$, empty squares) [206], and neutron scattering ($h = 0.4$, full squares) [207], compared with that of bulk water at ambient pressure (empty circles) [59] and to emulsified water at 2 kbar (full circles) [203]. Figure used with permission from [157].

Furthermore, our study can be used to discriminate two different dynamical degrees of freedom of hydration water. The intra-molecular dynamics is connected with the self-rotation of a single molecule around its own axis, instead the inter-molecular dynamics depends on the water interaction with protein molecules. H_2O molecules on the protein surface are highly mobile because the reorientational correlation time is in the order of picoseconds (see figure 3.9), but, their diffusion is slowed down by their interaction with protein amino acids. By applying the Stokes–Einstein (SE) relation (equation 1.10) [208] we can estimate the hydrodynamic radius ξ of the diffusing particles and we reported the obtained values as the temperature changes in figure 3.10. Although the density of the first hydration shell of water around the protein surface is up to 20% higher than that of bulk water, the viscosity remains essentially the same [208]. So, we calculate ξ by using the viscosity data of bulk water from the NIST database [37].

Note that when T is low, the value of the hydrodynamic radius ξ (~ 1.8 nm) coincides with that of lysozyme [209] proving that the first hydration shell of water is hydrogen bonded with the hydrophilic groups of the protein surface. However, for $T > 320$ K, ξ swiftly reduces, the water molecules are no longer tightly bonded to the protein surface forming local and transient aggregates whose dimension decreases as T increases. This
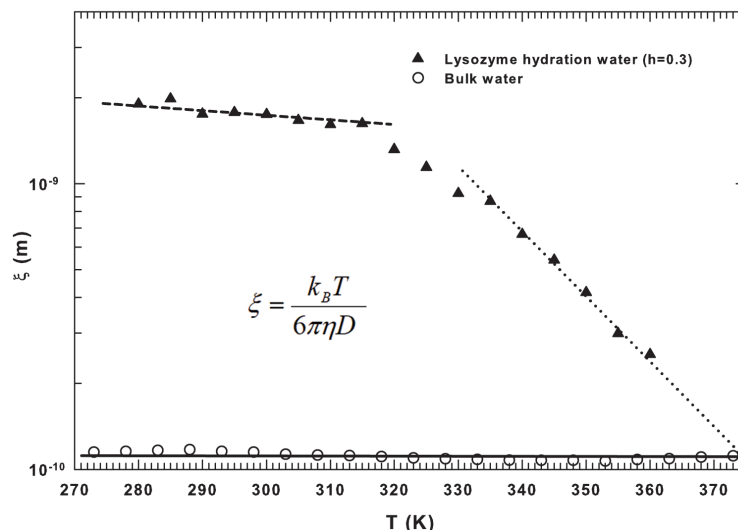
FIGURE 3.10: The hydrodynamic radius ξ obtained using the Stokes–Einstein relation (equation 1.10) for bulk water and lysozyme hydration water. Lines are guides for the eye. Figure taken with permission from [157].

was confirmed by the fact that the ξ values of hydration water approach those of bulk water (dotted line in figure 3.10) for $T \gtrsim 345$ K (when the protein unfolds completely).

3.2.3 Magnetization

As already mentioned, water can influence both the hydrophobic and hydrophilic groups of a biomolecule. Since surface water deeply conditions the function and the stability of proteins, studying how the "hydrophilic hydration" (see the paragraph 1.2.2) [120], i.e. the HB strength, rules their secondary structure and folding specificity is a very important topic [12].

During the folding process, the protein experiences numerous conformational changes and there is a significant reduction in the system configurational entropy as the native state is reached. We focus on how proteins explore the conformational space to understand the folding mechanism. In particular, this process is governed by many microscopic reactions, the nature of which is determined by the peculiarities of the energy surface. Therefore, protein folding is a complex process and we can use a well-known thermodynamic potential to describe it at constant pressure and temperature, the Gibbs free-energy, that is a function of the configuration of the protein to describe the protein-solvent system [210, 211]. Even if the degrees of freedom of a polypeptide chain permit the protein to have a very large number of possible configurations, the energy "constraints" reduce the configurations visited in the folding reaction to a limited number [212]. So, the comprehension of the free-energy surface ("landscape") allows us to understand the folding process. The *free-energy landscape model* is nowadays the most used one to describe several phenomena and especially the aging of the protein folding mechanism [210, 213, 214], i.e., the way in which proteins fold to their native state and then unfold (protein denaturation)[192, 213]. This model is based on the fact that, in complex materials and systems, there are many thermodynamical configurations in which the free-energy surface exhibits a number of local minima separated by barriers. Note that most of these

minima are related to small excitation energies linked with individual local conformational changes, e.g., rotations of individual side chains [210]. The energies involved in these small conformational transformations are typically on the order of $k_B T$, i.e., the size of the thermal energies of the atoms in the protein. As the system explores its phase space, the trajectory of its evolution is an alternating sequence of local energy minima and saddle points (transition states), which are associated with the positions of all the system particles. A trajectory thus specifies the path of the system as it evolves by moving across its energy landscape. In particular, the free-energy can be considered as the sum of the potential energy, which decreases as the native state is approached and therefore favors folding, and the unfavorable contribution of the decrease in the configuration entropy [192]. A balance between the potential energy and the configurational entropy leads to a free energy barrier that generates the two-state folding behavior usually observed in small proteins[30]. The potential energy decreases as the native state is approached and favors folding, but decreasing the entropy of the configuration is unfavorable to folding.

In this frame, NMR spectroscopy can be used to investigate folding (or unfolding) processes by probing interactions as they form at the level of individual residues. So, we investigate the thermal behavior of the amide NH, methyl CH_3 and methine CH chemical groups of hydrated lysozyme ($h = 0.3$) at ambient pressure in heating-cooling cycles within the $290 < T < 370$ K range[31] by means of the HR-MAS NMR technique (see paragraph 2.5) [185] with an accuracy of $\pm$ 0.1 K by using the T-dependence of the chemical shift of ethylene glycol as a T standard. We focused on the ^{1}H NMR spectra obtained from free-induction decay (FID). As shown in the chapter 2, the NMR signal intensity M is directly related to the system equilibrium magnetization M_0, which is connected to the susceptibility that depends linearly on the total number of mobile spins per unit volume, on the mean square value of the nuclear magnetic moment, and on $1/T$ (the Curie law, equation 2.36).

In our experiments, we used different heating and cooling cycles to explore, completely or partially, the thermal folding-unfolding process of lysozyme by following the scheme introduced by Salvetti et al. [150]: native (N) state $\rightleftarrows$ reversible unfolded (RU) intermediate state $\rightarrow$ irreversible unfolded (IU) or denatured state (see the paragraph 1.2.2). In cycles A and B, lysozyme is in its N state and we examined the entire process up to the complete denaturation of the protein (IU state). In particular, cycle A is performed by heating hydrated lysozyme from 295 to 365 K and then cooling it down to 297 K, whereas, in cycle B, we heat the sample from 296 to 366 K and then we cool it down to 298 K. In both the warming and the cooling cycles, the spectra were measured using steps of $\Delta T = 2$ K. Cycle C operates inside the native N state, instead, cycle D is executed inside the N $\rightleftarrows$ RU $\rightarrow$ IU region and cycle E within the N $\rightleftarrows$ RU region. We initiated these latter cycles at the sample heating temperature (310 K), but cycle D was reversed instantly above T_D at $T = 349$ K and the cooling in cycle E was started at 343 K (4 K below T_D). Note that heating and cooling steps were performed softly ($\Delta T = 1$ K) in a time period of approximately 20 minutes to prevent unwanted abrupt T changes.

The hydrogens coupled with the amide N atoms of the peptide via HB [215–217] quickly exchange with solvent H atoms in unfolded states, however they are often "defended" from exchange when the protein folding is the result of the connection of amides

---

[30]For small proteins, at most two states are observed on the longest time scales under physiological solvent conditions: (i) a high entropy high energy disordered phase corresponding to the unfolded protein, and (ii) a lower entropy low energy phase describing the folded protein [210].

[31]See the paragraph 1.2.2 and, in particular, the study of Salvetti et al. [150], performed in a similar T range, that has revealed that the observed $c_P(T)$ peak is caused by heat absorption when the equilibrium constant between the native lysozyme state and a conformational different intermediate state increases with T [137].

in the HBs and burial in the protein core. It is well known that the HBs of water molecules trigger the biomolecular activity of the protein peptides with the carbonyl oxygen (C=O) and an amide N–H molecular group. In particular, the most stable water-protein configuration is characterized by (i) a water proton donor bond to the carbonyl oxygen, and (ii) an amide N–H proton donor bond to the oxygen of H_2O [215–217]. In protein folding, water acts as a HB "glue" between the carbonylic and amidic groups [215], and during the folding phase the formation of hydrophobic clusters compensates for the loss of system configurational entropy. Hence, the protein stability will results strongly dependent on the HB strength (or lifetime) that decreases by increasing temperature. It is just this change in the HB strength that determines the thermodynamic properties of the hydrated protein.

In this context, starting from NMR spectra (see, for example, figure 3.6), we performed a spectral deconvolution of the Lorentzian contributions of the hydrophilic (the amide NH) and hydrophobic (methyl CH_3 and methine CH) groups to obtain their thermal behavior studying the properties of protein metabolites (hydrophilic and hydrophobic) in different thermal cycles as an experimental proof of the folding funnel (free-energy landscape). For all the measured spectra in the heating and cooling cycles, we analyze the magnetization M of the three groups centered at chemical shifts NH $\simeq 6.7$ ppm, $CH_3 \simeq$ 0.8 ppm, and CH $\simeq 0.94$ ppm. The results in figures 3.11, 3.12 and 3.13 are shown in an Arrhenius plot (the log of the measured magnetization vs. the reduced temperature $1000/T$) within the same intervals, providing a detailed analysis of the different energetic behaviors of the investigated protein groups.The heating and cooling steps for all the studied cycles are denoted with red and blue (full and empty) symbols, respectively. Furthermore, all figures display the region of the N, RU and IU states of lysozyme with the T_D and T^* temperatures. In particular, T^* signals the limit of the protein native state [13, 15] and the breakdown of the tetrahedral structure of water [59].

In figure 3.11, the Arrhenius representation of the measured magnetization values ($M(T)$) of the hydrophilic amide NH groups has been reported for all the performed thermal cycles (A, B, C, D, and E).

Note that there is a large $T-$interval in cycles A and B for which the complete protein denaturation can be investigated, and a smaller $T-$interval in C and D. The overall behavior of cycles A, B, and D is essentially the same. Furthermore, the figure shows the temperature region of the lysozyme-water configurational $c_P(T)$ peak (dotted line) [137, 150]. We notice that, increasing T, the magnetization exhibits a pure Arrhenius (AR) behavior (with an activation energy $E_A \simeq 4.58$ kcal/mol) up to the onset of the $c_P(T)$ peak. Above this point, it follows a super Arrhenius (SA) trend with a marked increase that stops at approximately T_D, after which it evolves again according to the AR law ($E_A \simeq$ 7.38 kcal/mol) up to 365 K, where the thermal cycle is inverted. Note that, during the cooling step, the energetic behavior of NH groups is about the same as the heating phase up to T_D. At the lowest T, $M(T)$ displays two other AR behaviors, (i) one that stops near T^* with $E_A \simeq 9.91$ kcal/mol, and (ii) one at $T < T^*$ that is dissimilar from that of the heating phase in the same temperature range. After the heating phase, the cycle D reverses in temperature and lysozyme denatures in the same way as in A and B. Cycle C shows complete reversibility and thus has the same activation energy as the other cycles during the early heating phase. Note that the energy behavior registered in cycle E turns back at $T = 343$ K, i.e., 4 K below T_D, but, in the heating phase, the magnetization $M(T)$ exhibits the same behavior as the corresponding one indicated in cycles A, B, and D, whereas, in the cooling phase, the cycle E differs completely from the others and this situation is due to the fact that the protein recovers its native condition as it nears T^*. So, all of this demonstrates the energetic behavior of the hydrophilic amide group in a cycle that operates reversibly between the N native state and the RU state (as we have in cycle
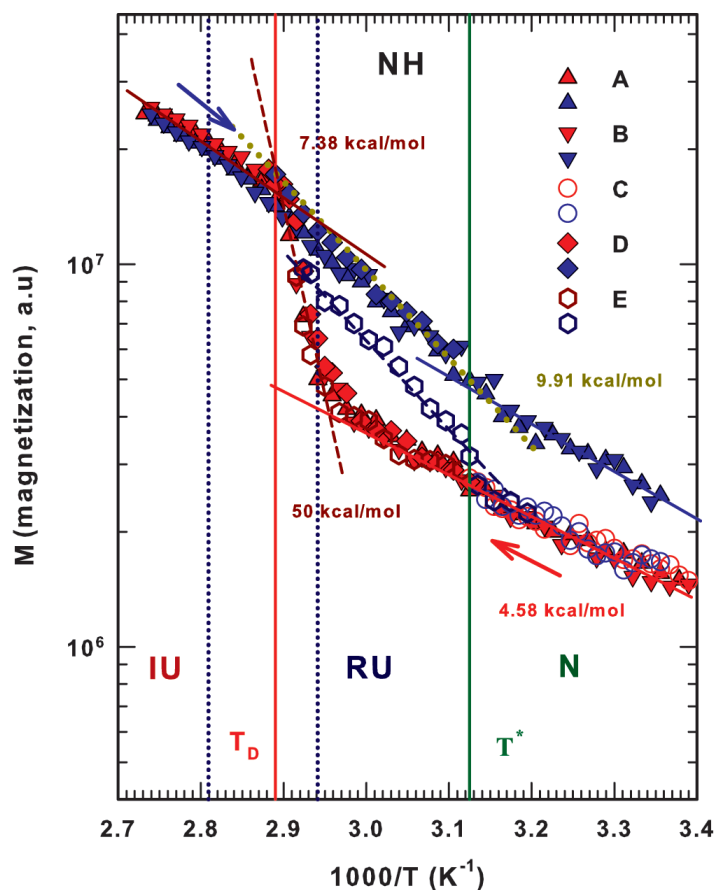
FIGURE 3.11: The Arrhenius representation of the measured magnetization M values of the hydrophilic amide groups (NH). Data for all the five distinct investigated thermal cycles (A, B, C, D, and E) are displayed distinguishing the heating and cooling cycles (red and blue symbols, respectively). The characteristic temperatures T^* and T_D are also reported. Lines represent Arrhenius behaviors; the corresponding activation energies E_A are indicated in kcal/mol. Cycles A, B and D deal with a complete denaturation; C operates in the native (N) protein state; E refers to the native (N) and intermediate (RU) states. See the text for further details. Figure used with permission from [12].

E). We evaluate the energy (E_A) and enthalpy difference between the native and unfolded state (in cycles A, B, and D) and the energy of the reversible unfolding (in cycle E). We find $\simeq 51$ kcal/mol for the first case and $\simeq 12$ kcal/mol for the second, values that agree with those calculated for lysozyme (58 kcal/mol and 14 kcal/mol) and for other globular proteins [211].

Figure 3.12 illustrates the thermal behavior of the methyl CH_3 lysozyme groups reporting all the studied cycles.

It is possible to notice that there are qualitative similarities with the amide groups (figure 3.11), however, the different energies mark a distinct pathway with respect of that one of the NH groups in both the reversible unfolding and the irreversible denaturation. In fact, in the heating phase, the N region is characterized by an activation energy $E_A \simeq$ 8.3 kcal/mol, but, differently from what evinced in the case of the hydrophilic amide groups, the AR behavior stops at T^*, and in the RU region a weak maximum appears at $\simeq 330$ K, after which we have the irreversible denatured phase and the magnetization
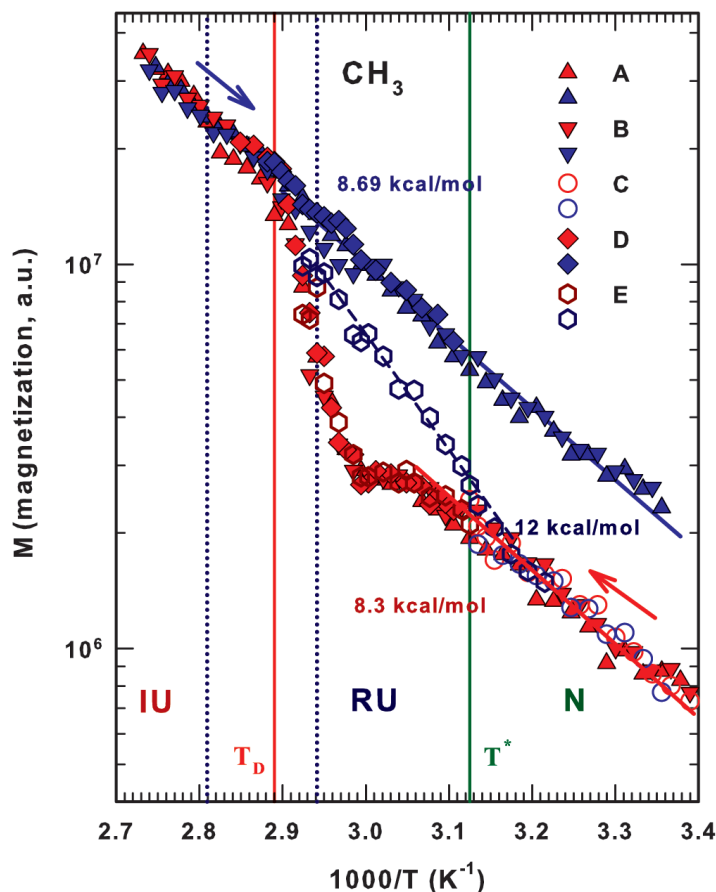
FIGURE 3.12: The protein methyl CH_3 magnetization M reported in an Arrhenius plot for all the considered thermal cycles. Lines and symbols are the same used in Figure 3.11. See the text for further details. Figure used with permission from [12].

rapidly increases to T_D with an SA trend. For $T > T_D$, it evolves again according to the AR law. Instead, the cooling phase of the methyl groups appears to be completely AR across the wide temperature range with $E_A \simeq 8.69$ kcal/mol. In the cooling side of cycle E in the RU region, the activation energy $E_A \simeq 12$ kcal/mol.

Figure 3.13 shows the magnetization $M(T)$ for the methine CH groups that in the heating phase is larger than that of the cooling phase. In the heating phase, within the N region, all the cycles are characterized by an AR evolution with $E_A \simeq 9.09$ kcal/mol that stops near T^*. After this temperature, the magnetization has a maximum at $T \simeq 330$ K and then decreases to a minimum at T_D and further evolves, exhibiting AR behavior. During the heating phase, the methine groups are more mobile in the RU region than in the fully denatured phase (IU) phase, unlike the NH and CH_3 groups. This confirms that the hydrophobic groups are buried during protein folding and that they are affected by the presence of solvent hydrogen atoms. Note that this fact is more evident in CH_3 than in CH. However, in cycles A, B, and C, the methine groups exhibit an AR behavior with $E_A \simeq 6.41$ kcal/mol in the cooling step. In cycle E the methine $M(T)$ recovers (from the RU phase) the thermal trend of the native state, which is an AR behavior with $E_A \simeq 5$ kcal/mol.

Figures 3.11, 3.12 and 3.13 show that our results confirm that is internal water, and specifically, the HB network formed by water, amidic proton (N–H), and carbonyl oxygen
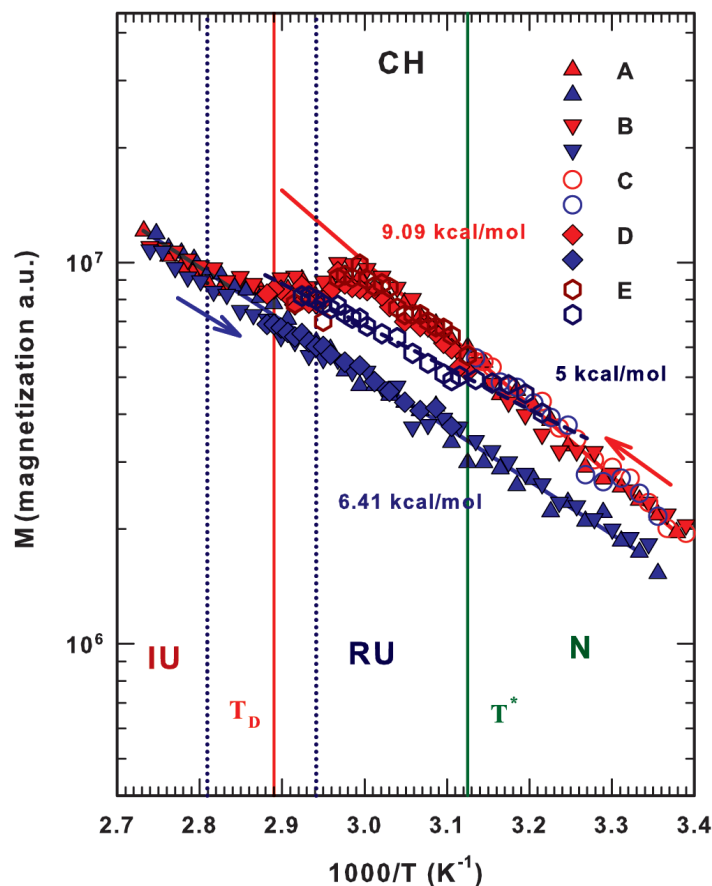
FIGURE 3.13: The thermal evolution of the magnetization M, illustrated in an Arrhenius plot, of the protein methine CH groups for all the studied thermal cycles. Lines and symbols are the same previously used in figures 3.11 and 3.12. See the text for further details. Figure used with permission from [12].

(C=O), that "drives" the protein structure from a state to another one. Furthermore, these figures display that above T^*, as T_D is approached, the role of hydration water becomes increasingly important and causes irreversible unfolding in the biopolymer. In the RU interval between T^* and T_D, the HB structure of the protein side chains allows the internal water to impose a perpetual folded structure. This aspect is confirmed by all the measured activation energies. Besides, after studying distinct thermal cycles, including the reversible ones and those involving complete denaturation, we find that protein properties during these processes are strongly affected by different energetic routes. So, our findings confirm the validity of the theoretical "energy landscape scenario", and also explain at molecular level the role of the protein water in the protein configuration stability.

Furthermore, a comparison between the behavior of the three considered peptide groups confirms that HBs play a role in protein folding. Evidence for this rests not only in the activation energy values that are of same order of magnitude as in the HBs, but also in the thermal behavior of the methine groups, specifically in their magnetization $M(T)$ behavior in the N and the RU phases. The higher molecular mobility is caused by the burial effect of the HBs on the hydrophobic groups, which is particularly strong in the case of the methyl groups. The two forms of protein water, hydration water and internal water, are essential in protein folding. Because all water in the unfolded state belongs

to the solvent, hydrogens in the amide groups with peptide bonds interact rapidly via HBs with water. When the protein folds these interactions involve only internal water, which is linked with amides and buries the protein interiors. Thus clusters of hydrophobic residues are formed in the folded protein and the methine groups are more mobile than the methyl groups.

3.2.4 Mean square displacement

As already stated, the translational diffusion is strictly linked to the characteristic timescale Δ (the "diffusion" time). For homogeneous solution in which there is not chemical exchange, we obtain the same result for free diffusion of the simple random Brownian motion or "Fickian" processes, i.e., the mean-squared displacement (MSD) scales linearly with time, because the value of Δ is not important [168, 175]. Instead, when a species diffuses within a confined space (known as "restricted diffusion"), the displacement of the diffusing particle will be a function of Δ and of the diffusion coefficient, and of the size and the shape of the restricting geometry. Therefore, gradient-based measurements are sensitive to the enclosing geometry in which the diffusion occurs and, in this case, we are in presence of the so-called "anomalous diffusion" [168, 218, 219]. In a water-protein system, the situation is rather more complex because H_2O molecules interact with the larger macromolecules (i.e., proteins) and these interactions act on a time scale much smaller than the smallest experimentally available Δ and, thus, they can be correctly averaged on the time scale of Δ [168]. As mentioned in paragraph 1.2.2, in a protein-water solution, the biochemical activity of the protein is strongly influenced by the hydration level h [220], and, for lysozyme, the enzymatic activity is very low up to $h \cong 0.2$, but when h is increased from 0.2 to 0.5, the activity increases sharply. We recall that the value $h = 0.3$ corresponds to a water monolayer covering the protein surface (the first hydration shell) [123]: in this situation, the protein functionality is activated.

By means of ^{1}H PFGSTE NMR technique, our aim is to study the dependence of MSD of lysozyme hydration water ($h = 0.3$)[32] on the diffusion time Δ at temperatures below and above the "magic" temperature T^* in order to check if we are in presence of anomalous diffusion. In particular, we measure the MSD for several values of diffusion time Δ to consider the fact that complex materials can exhibit generalized Brownian motion (i.e., Lévy flight or fractal diffusion) rather than simple Brownian motion [221]. In our measurements, we use the following experimental parameters: $3 < \Delta < 40$ ms, $\delta = 0.2$ ms, and $0 < g < 1200$ Gauss/cm. Furthermore, we set the duration of the 90° pulse to 22 μsec and the repetition time to 10 sec. With these conditions, i.e., by keeping $\delta \ll \Delta$, we can use the SGP approximation to study the dynamics of the system ignoring the effects of motion during the gradient pulse[33][168, 175].

Therefore, for inhomogeneous systems and anomalous diffusion, in the SGP limit, the MSD can be described by a power law [168, 178, 222, 223]

$$\langle z^2(\Delta) \rangle = 2D\Delta^\alpha \tag{3.7}$$

in which α is the so-called fractal diffusion exponent [224]. In a typical Brownian diffusion process, $\alpha = 1$. If $\alpha > 1$, the phenomenon is called super-diffusion and if $\alpha < 1$, the particle undergoes sub-diffusion [168, 223, 225–227].

Figure 3.14 displays the normalized spin-echo attenuation Ψ/Ψ_0 in a log-log plot with $q^2\Delta$ for hydrated lysozyme ($h = 0.3$) at 315 K and 335 K, below and above the magic

---

[32]The powder of lysozyme was hydrated with $h = 0.3$ by using the procedure indicated in [136]

[33]Rigorously, it can be assumed that the gradient pulse is like a delta function, that is, $\delta \to 0$ and $|\vec{g}| \to 0$, while their product remains finite [168]

temperature T^*, respectively. Note that each spin-echo attenuation data are obtained for different Δ's at a fixed $\delta = 0.2$ ms.
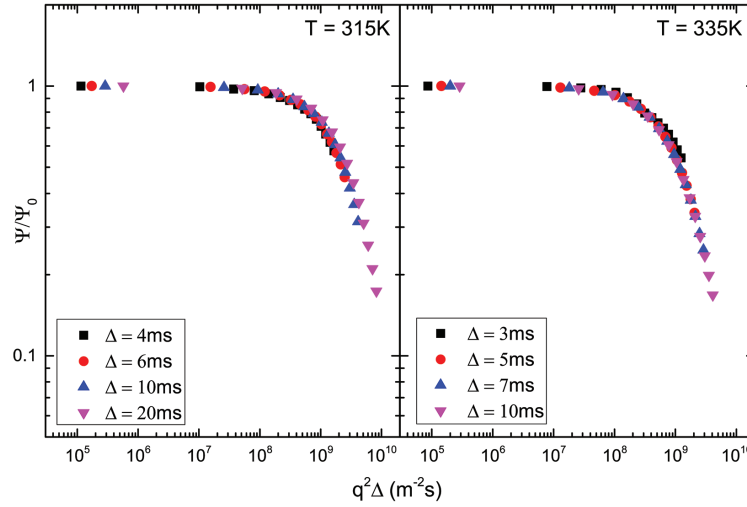

FIGURE 3.14: The normalized pulsed gradient spin-echo NMR attenuation Ψ/Ψ_0 vs the reduced variable $q^2\Delta$ (at different Δ values and same gradient pulse width δ), for hydrated lysozyme at the temperatures 315 K and 335 K, i.e., below and above T^*, respectively. Figure taken with permission from [158].

Note that all the data are superimposed to each other showing a not relevant dependence on Δ. As mentioned in section 2.4, a spin-echo attenuation signal can be defined at low q by an exponential with the form of equation 2.66, for the second cumulant approximation [169, 179],

Figure 3.15 shows the spin-echo attenuations as a function of q^2 in a log-lin plot for all the considered T. In particular, we compare data with a diffusion time Δ of 4 ms for T below T^* and $\Delta = 3$ ms for $T > T^*$. The solid lines represent fits of the data with a "modified" version of equation 2.66. We performed the best-fit procedure in a constant data range of $1 > \Psi/\Psi_0 > 0.8$. Note that the linear trend holds for all the q^2 range only for the lowest T. Furthermore, the deviation from linearity is strongly enhanced for the temperature above the denaturation threshold.

We relate this behavior with the continuous unfolding of lysozyme and the following "release" of the "internal water" that, mixing up with hydration water, now contributes to the dynamics [137]. In fact, as already stated, in hydrated proteins, two types of water can be identified: bound internal water and hydration water. The first one has molecules placed in internal cavities and fractures playing a structural role in the folded protein itself. Instead, hydration water is "confined" in the protein surface interacting deeply with it and controlling the biofunctionality of the macromolecule [13].

From the "initial" part of the fits displayed with a bold curve in figure 3.15, we obtain the MSD and we report the $\langle z^2(\Delta)\rangle$ values in figure 3.16 as a log-log plot at 295 K, 315 K, 335 K, and 355 K. Furthermore, we execute a linear fit of the MSD data using the equation $\ln\langle z^2(\Delta)\rangle = \ln(2D) + \alpha\ln\Delta$ obtained from the power law 3.7. These fits have been reported in figure 3.16 as solid lines.

It is well evident from figure 3.16 that the slope α of the linear fits increases with temperature, indicating the presence of anomalous diffusion. This situation can be explained in the frame of the hydrogen bond: in fact, increasing T, the HBs can be easily broken
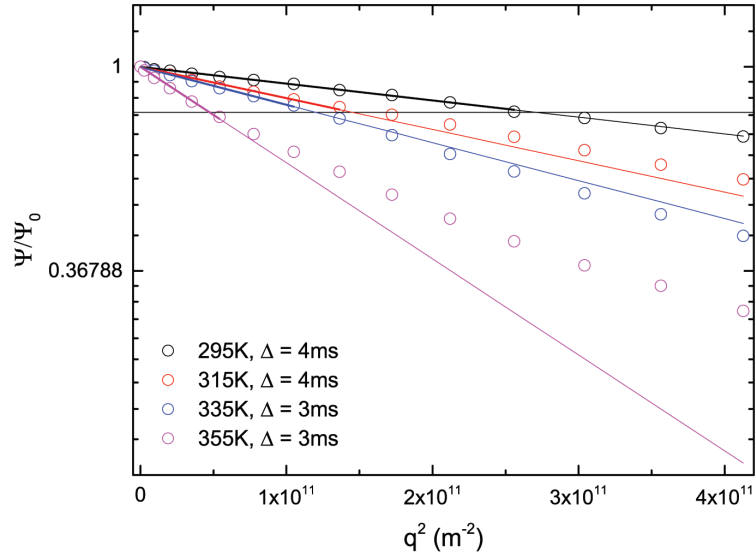
FIGURE 3.15: The normalized spin-echo amplitude Ψ/Ψ_0 vs q^2 for the investigated system at the indicated Δ and T. The solid curves represent fits of the experimental data with equation 2.66. Figure taken with permission from [158].
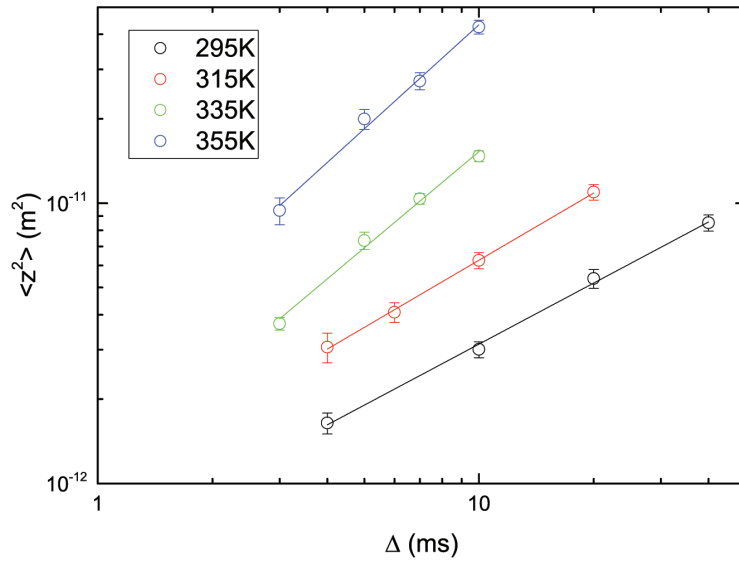
FIGURE 3.16: Mean square displacement as a function of observation time Δ reported in a log-log plot for hydrated lysozyme at 295 K, 315 K, 335 K, and 355 K. The solid lines represent the linear fits of the data obtained applying the logarithm at each member of equation 3.7. Figure taken with permission from [158].

causing a greater mobility to the protein side-chains. Therefore, at the highest temperatures, internal water changes from a "confined" state to an essentially free one diffusing and interacting with hydration water [137]. The values α for each fit of figure 3.16 have been reported in figure 3.17. Here, we show the dependence of the exponent α of anomalous diffusion with temperature: results prove that α increases as T increases, denoting,

as mentioned before, an enhancement of protein chain mobility as the system performs a transition from the folded to the unfolded state. In particular, the system undergoes from a condition in which $\alpha < 1$ (sub-diffusion dynamics) to $\alpha > 1$ (super-diffusion limit). In this frame, the onset of this change in the dynamics of the system can be identified in the magic temperature $T^* \approx 320$ K. In fact, for $T \approx T^*$, α is around 1 and the motion is Brownian.
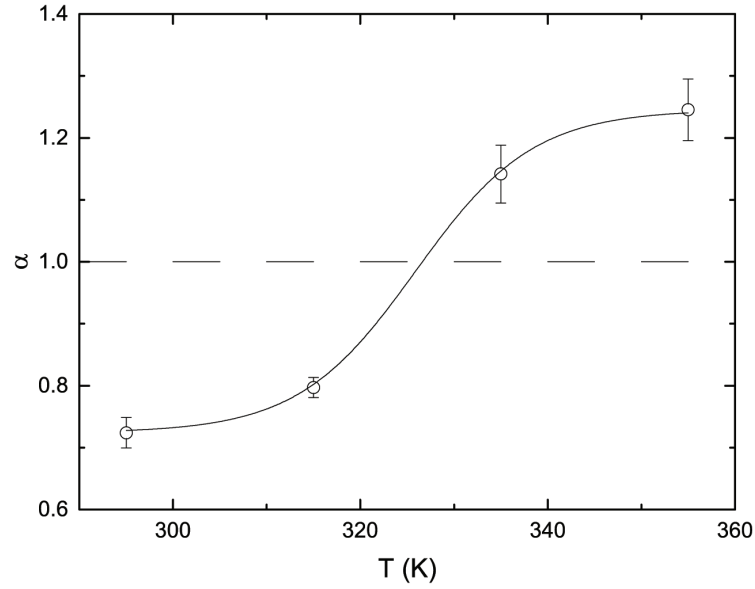

FIGURE 3.17: T dependence of the power law exponent α for hydrated lysozyme. The system passes from a sub-diffusive state ($\alpha < 1$) to a super-diffusive one ($\alpha > 1$) upon crossing the magic temperature T^*. Figure taken with permission from [158].

Chapter 4

Conclusions

We show how the thermal properties of water and, in particular, its anomalies influence the thermodynamic properties of aqueous systems.

In chapter 1, we highlight how water thermodynamics differs from that of other liquids. Indeed, as shown in paragraph 1.1.4 of the first chapter, in addition to the well-known density maximum at 277 K and atmospheric pressure (figure 1.5), the thermodynamic response functions of water show sharp variations on decreasing T until they diverge toward the supercooled regime. This anomalous thermal behavior in such quantities, e.g., the coefficient of thermal expansion, the isothermal compressibility, and the isobaric specific heat (see figure 1.6), may be interpreted considering that liquid water is a mixture of two different structures, characterized by a distinct density. The formation of these two structures depends on the competing effects of hydrogen bonding and van der Waals interactions (together with thermal energy). Since HB is a directional bond, it has a strong tendency to form locally favored structure with voids, the presence of which cause an increase of the volume, and, therefore, a reduction of the density. In particular, the strength of hydrogen bonding (i.e., the number of bonds of that kind and their mean life-time) increases on lowering T, when the Low Density Liquid (LDL) phase starts to grow with respect to High Density Liquid (HDL) phase. In this situation, fluctuations of both microscopic entropy and volume originate the sharp variation of the thermodynamic response functions of liquid water in its supercooled regime.

Just from a thermodynamic point of view, several theoretical scenario have been proposed to explain the anomalies of water (see paragraph 1.1.5). The most plausible interpretation relates the peculiar thermal behavior of the response functions to the existence of a second critical point in water. Such a point is predicted by several theoretical studies and simulations to be the end point of the coexistence line of a liquid-liquid phase transition (LLPT) between LDL and HDL phases and the starting point of the Widom line. The Widom line is the critical isochore in the one phase region, i.e. the asymptotic limit to which all thermodynamic response functions maxima tend on approaching the critical point. This is why these functions can be expressed in terms of correlation length that diverge approaching a critical point. In particular, by using the Adams-Gibbs theory, it was confirmed that crossing the Widom line corresponds also to a change in the dynamic behavior, associated to the fragile-to-strong transition (FST).

After this introduction on water, we focus on the essential role of biological water in its interaction with methanol and lysozyme. Note that the state-of-the-art of the just mentioned pure biosystems and their behavior in aqueous solution has been described in paragraphs 1.2.1 and 1.2.2.

In chapter 2, after presenting the operating principles of the NMR spectroscopy, we illustrate the instrumentation and the techniques used in our experiments. In particular, we used an Avance Bruker NMR Spectrometer operating at 700 MHz (^{1}H resonance frequency), and the Pulse Field Gradient Stimulated (Spin) Echo (PFGSTE) and High-Resolution Magic Angle Spinning (HR-MAS) techniques.

The dynamics of the water-methanol mixture have been investigated by measuring the ^{1}H-PFGSTE NMR self-diffusion coefficient D and, so, the relaxation time t_α as functions of the water molar fraction X_W and temperature in the range $160 < T < 335$ K. In particular, in our study, we compared our results with data from the literature, examining the evolution of the indicated transport parameters at a fixed T as a function of X_W and evaluating how they differ from those in an ideal mixture in which there are no interacting molecules.

Figure 4.1 displays the maxima variation of Δt_α (difference from ideal solutions) in absolute units as a function of T in an Arrhenius plot ($|\Delta t_{\alpha,m}|$ versus $1000/T$). This motif shows the impressive change in system dynamics near T_L, where $\Delta t_{\alpha,m}$ varies from negative to positive as T is raised (inset of figure 4.1). Note that there are large errors for $|\Delta t_{\alpha,m}|$ data in the $4.2 < 1000/T < 4.6$ K^{-1} range. Regardless of the shift in the sign of $\Delta t_{\alpha,m}$, the data show two distinct dynamical behaviors in the low and high temperature regimes. In particular, in the high-T region, the $\Delta t_{\alpha,m}$ is positive and there is a little thermal variation that ends in the $3.66 < 1000/T < 4.1$ K^{-1} range (i.e., from 273 K to 244 K) and then decreases dramatically and becomes negative. In the high temperature range, $\Delta t_{\alpha,m}$ slowly decreases by approximately one order of magnitude as T is increased until it reaches the maximum studied temperature of 335 K (see figure 3.5). XAS and MD studies [119] show that in this latter T-region the configuration of the system is formed by a large HB network involving both H_2O and MeOH molecules, and that the hydrophobic interaction of the methyl groups boosts the formation process. Note that the ratio of the hydrogen donating sites between water and methanol is 1/1 and the molar ratio $\geq 1/1$. The figure inset shows a zoom of the high-T data and we identify a crossover in which the rapidly evolving data slow to moderately evolving (behaviors represented by two straight lines) when T is decreased to approximately $1000/T = 3.16$ K^{-1} ($T \simeq$ 318 K). This temperature is almost coincident with T^*, i.e., the temperature above which the HB clustering stops [190] and the H_2O molecules are only influenced by methyl hydrophobicity.

The $|\Delta t_{\alpha,m}|$ values in the $1000/T = 4.3$ K^{-1} region are influence by large errors because they change from positive to negative near $T_L \simeq 225$ K (see figure 3.3). Further decreasing T causes $|\Delta t_{\alpha,m}|$ to increase by seven orders of magnitude when $220 > T >$ 165 K where the LDL network prevails over the HDL one. Note that in this supercooled region inside the "No Man's Land", these relaxation time surpluses are concentrated for all the temperatures considered at circa the same water molar fraction, $X_W \simeq 0.75$. Here water molecules overcome methanol molecules and develope hydrogen bonds networks. So, at low temperatures, the dynamics of the system are ruled by the LDL phase and by the increase in HB interactions when the concentration of water is high. This situation is reproduced in the pure water relaxation time values t_α^W, which for $T < T_L$ evolve from 10^{-9} sec to 10^{-3} sec, and water behaves as a strong glass-forming liquid (see figure 3.1). Here, MeOH molecules are blocked inside the LDL water network and affect the water dynamics by decreasing the relaxation time of the H_2O molecules in the HB network. This reduction is created by changes in the hydrogen bonding interactions forced by the methanol hydroxyl groups (OH) linked via HBs to the LDL water network. Note also that the differences in the relaxation times between H_2O and MeOH for $T \simeq T_L$ are of approximately three orders of magnitude and that they deeply increase as T reduces.

When $T > T_L$, the discrepancy between t_α^W and t_α^{MeOH} decreases fast and becomes less that one order of magnitude at ~ 250 K where the excess in the solution relaxation time $\Delta t_{\alpha,m}$ is positive. When the concentration of methanol and water molecules are equal, the surplus in the relaxation time is caused by the methyl hydrophobic component, which obligates water to join a dynamical cluster of both methanol and water molecules with a relaxation time at approximately $X_W \simeq 0.5$ that is larger than the relaxation times
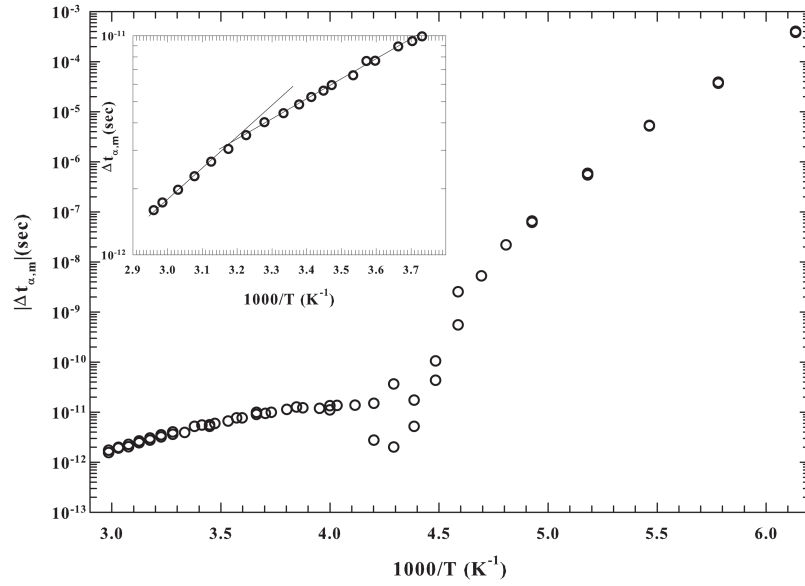
FIGURE 4.1: The maxima variation in the relaxation times are reported in absolute units $|\Delta t_{\alpha,m}|$ and illustrated in an Arrhenius plot ($|\Delta t_{\alpha,m}|$ versus $1000/T$). The inset displays the high temperature region data in an enlarged scale to see better the change of the data behavior (crossover) when the T^* temperature is reached. Figure taken with permission from [84].

of pure liquids, t_α^W and t_α^{MeOH}. In particular, the advancing loss of this excess by increasing T is also related to the reduction of t_α^W and t_α^{MeOH}, and, at 298 K, these quantities are $t_\alpha^W \simeq 8.8 \times 10^{-12}$ s and $t_\alpha^{MeOH} \simeq 4.1 \times 10^{-12}$ s.

We consider the maxima variation of the relaxation time expressed in absolute values, $|\Delta t_{\alpha,m}|$, in the two extreme T regions as an indirect measure of the bond strength and assume that both are characterized by clustering processes involving alcohol and water molecules. The difference is that the dynamic stability of H_2O is smaller at high T due to methyl hydrophobicity than that at low T, which is provided by the HBs and thus by the LDL water phase arranged in tetrahedral networks with comparatively long lifespans.

Lastly, in our study of methanol-water mixture, we consider that the solution dynamics vary with both concentration and temperature. This assertion was made just by calculating the distinct relaxation time behaviors in the rich water phase with respect to the opposite one, as previously stated. Hence, if our conjecture that at low T water drives the system dynamics and that the LLPT hypothesis is correct, T_L must depend on the system concentration. To highlight what has just been said, we drew lines connecting the relaxation time data points reported in figure 3.3a for each studied T generating the figure 4.2. These lines, achieved by a simple smoothing process, are a guide for the eyes, but well illustrate how the Widom line may be a function of X_W. Figure 4.2 also displays that for all the temperatures with $T > 238$ K, the $t_\alpha(X_W)$ behavior is regular, viceversa in the deep supercooled regime ($T < 228$ K) the relaxation time exhibits a more complex behavior. In fact, when the number of water molecules is higher than that of the alcohol ($X_W \gtrsim 0.6$), t_α abruptly increases. Anyway, this considerable increment cannot be singular (divergent), because the relaxation times must increase somewhat toward the limiting H_2O value at a certain concentration (as shown in figure 3.1). So, the water molar fraction X_W marking the crossover between these two regimes can be fairly related with the

Widom line. In addition, the t_α of this crossover concentration raises decreasing T from values of the order of nanosec up to values of seconds at the lowest temperatures. Note that the crossover concentration reduces its value with T. A situation this latter that is fully consistent with the hydrophobicity effects on the HB network, being the Widom line the locus in which the LDL phase (the water HB network) dominates over the remaining HDL.
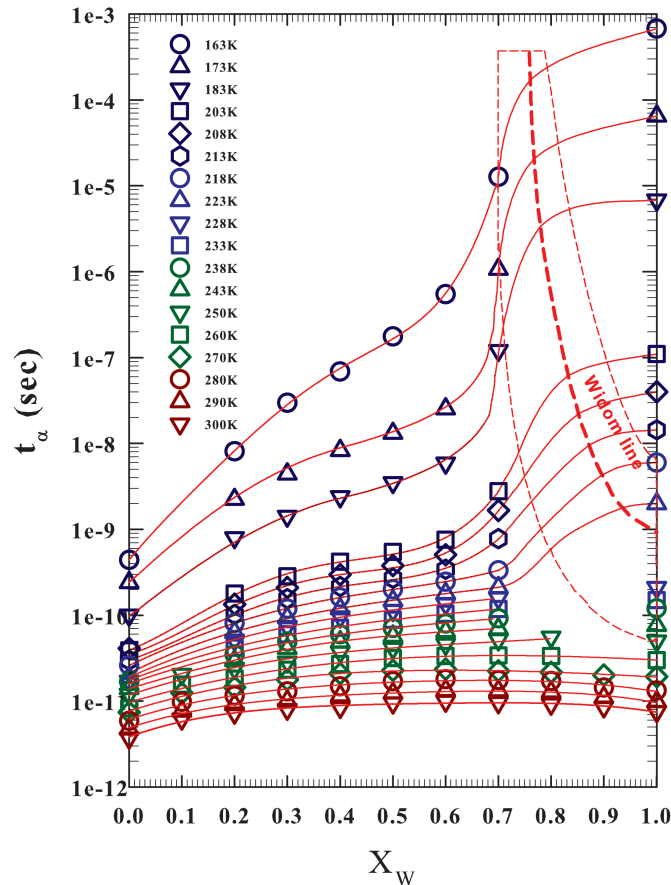

FIGURE 4.2: The solution relaxation time t_α are reported in function of X_W. The figure shows a new approach from which is highlighted how the Widom line temperature may depend on the alcohol concentration. Figure taken with permission from [84].

Therefore, our experimental study on water-methanol systems has three important findings: (i) the hydrophobicity of methanol molecules dominates the dynamics of the solution when the water HB network is less developed and on the order of picoseconds or shorter (see figure 3.2); (ii) the low temperature dynamics of the solutions are strongly influenced by the structural changes in the water at its FSDC where the LDL liquid phase takes a dominant role in the deep supercooled regime and thus supports the LLPT hypothesis; (iii) in water alcohol solutions the Widom line temperature also depends on the molar fraction: it decreases as the alcohol concentration increases.

For what concerns the interaction with protein, we converge our attentions in the role that water plays in determining the structure, the dynamics and the biological activity of proteins. We investigate, in particular, the case of water-lysozyme solution.

Firstly, we followed the evolution of the proton NMR spectra in the range of 298 $< T <$ 366 K with the HR-MAS probe, examining the thermal denaturation of hydrated

lysozyme ($h = 0.3$). In the obtained spectra (figure 3.6), all the peaks belonging to the protons of lysozyme begin to appear at ≈ 320 K, except those at 1 ppm (assigned to the methyl functional group). Therefore, at this hydration level, the protein side-chains are not so mobile to be revealed by NMR up to ≈ 320 K, noticed as the magic temperature T^*. At higher T, they become more flexible and this corresponds to have well detectable contributions. At $T \approx 344$ K, identified as the protein denaturation temperature T_D, the magnetization signal suddenly increases: a clearly sign of the insurgence of the irreversible unfolding process. The corresponding reduction of the peaks width indicates an increasing of the protein mobility induced by the almost complete hydrogen bonding breakage. Therefore, the main mechanisms that define the thermal limits of the enzymatic activity of proteins are given by the hydrogen bond coupling between hydration water and protein hydrophilic groups.

Furthermore, by means of the ^{1}H-PFGSTE NMR technique, we study the self-diffusion of protein hydration water at several hydration levels ($0.3 < h < 0.65$) across a large T range that includes the deeply supercooled regime. Our experimental evidence, reported in figure 3.7 and, for convenience, here in figure 4.3, indicates that the dynamics of protein hydration water are triggered by two characteristic phenomena. The first one is characterized by the fact that the measured fragile-to-strong dynamic crossover (FSDC) temperature is unaffected by the hydration level, and this furnishes further proof that water plays a fundamental role in the "dynamic" protein transition [76, 136, 152, 154, 191, 196]. The second result is that the first hydration shell remains liquid at all hydrations, even at the lowest temperature. This situation explains why proteins (in their dynamic and biological properties) survive inside the "No-Man's Land". Our data show that the first hydration layer ($h = 0.3$) plays a bioprotective role by remaining liquid at low T. Specifically, it protects the functioning of the local protein conformational dynamics and disallows irreversible changes in the molecular structure.

The self-diffusion data $D(T)$ in the high-T regime of bulk water indicate that T^* signals a new dynamic crossover. Specifically, when T decreases the dynamics change and there is a shift from Arrhenius to super-Arrhenius behavior. So, as already recognized, T^* strongly affects protein folding, and it marks the crossover in bulk water from "normal" liquid behavior when $T > T^*$ to behavior characterized by thermodynamic anomalies when $T < T^*$.

In the frame of the very important case of the first hydration shell of lysozyme, we performed more detailed studies of the dynamics of water linking the corresponding changes to different states of the folding-unfolding process. In particular, we differentiate between the translational and rotational contributions, which are the proton self-diffusion coefficient and the reorientational correlation time, respectively. The self-diffusion in the hydration water is slower than in the bulk solvent, and the ratio between these two values as a function of the inverse temperature, exhibits three changes at approximately 277 K, 316 K ($\approx T^*$), and 342 K ($\approx T_D$), with corresponding changes in the activation energy (as shown in figure 3.8). In the first region, when T is less than 277 K, the HB network on the protein surface is strong and stable and we obtain the activation energy of ≈ 1.8 kcal/mol. Between 277 K and 316 K, there is the thermal region of optimal biological functioning and here we have a smaller activation energy (~ 0.4 kcal/mol). At ~ 316 K, the HB network of the first hydration shell begins to crumble denoting the onset of the protein unfolding process[34]. However, when $316 < T < 342$ K and the activation energy is ≈ 2.7 kcal/mol, the unfolding process is still reversible [137]. Finally, when $T \gtrsim 342$ K and the activation energy is ~ 5.3 kcal/mol, the HB network breaks down completely and the protein structure resembles that of a linear chain of amino acids. Here, the unfolding

---

[34]Structurally T^* has been identified as the onset temperature of HB clustering [190].
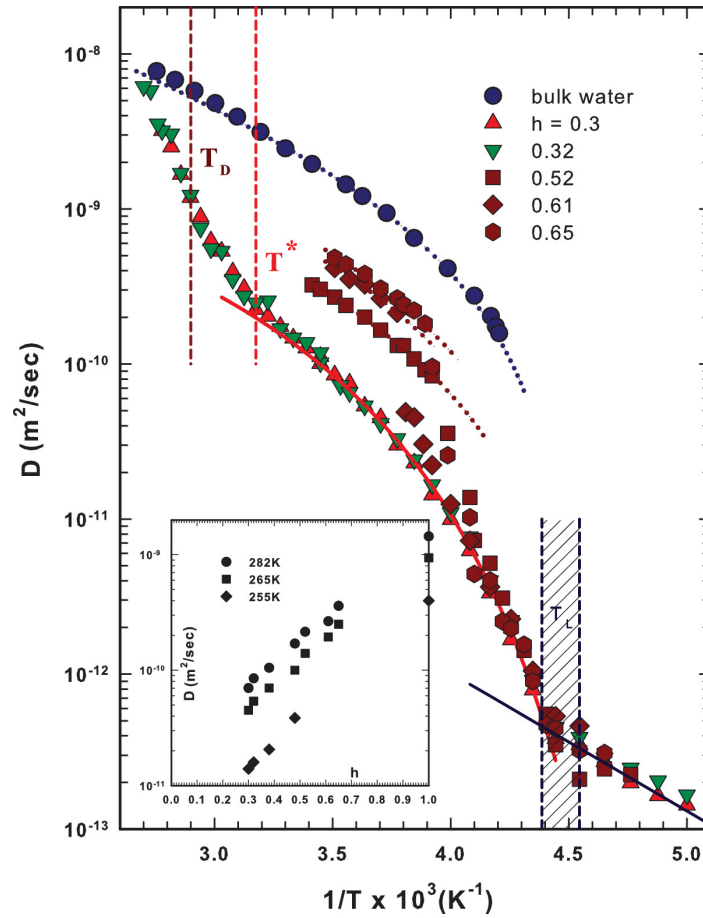
FIGURE 4.3: The self-diffusion $D(T)$ data are reported in an Arrhenius plot for several hydration levels with the data of pure bulk water [58] (blue filled dots). The three protein significant temperatures are indicated: the crossover one T_L, T_D that identifies the folding-unfolding process and T^* that marks the water transition from a normal fluid to the anomalous and complex liquid. The reported curves are the data fits with the ideal mode-coupling-theory scaling law [193, 194]. Finally, the $D(T)$ behavior at $h = 0.61$ shows a marked jump at $T \approx 265$ K as well as the proton self-diffusion data for $h = 0.52$ and 0.65. The inset displays the hydration dependence of D in the T region where all the protein hydration water remains liquid. Figure used with permission from [13].

process becomes irreversible. In figure 3.9, we found that the reorientational correlation time τ_θ in hydration water is slower than in bulk water for temperatures lower than the temperature of irreversible denaturation. When $T \sim 346$ K, τ_θ quickly shrinks approaching the values for bulk water, and the water molecules can rotate freely. Subsequently, we applied the Stokes–Einstein relation to the lysozyme hydration water, calculating the hydrodynamic radius of the particles (figure 3.10). We found that at ambient temperatures the radius coincides with the lysozyme hydrodynamic radius (≈ 1.8 nm). When $T > 320$ K, ξ decreases sharply and when $T > 345$ K its value approaches that of bulk water. This result confirms that when lysozyme unfolds completely, H_2O molecules are essentially free and no longer bridge the protein residues.

Figures 3.11, 3.12 and 3.13 show the energetic evolution that occurs during the folding and unfolding of separate peptide hydrophilic (the amide NH) and hydrophobic (methyl CH_3 and methine CH) groups in single layer hydrated lysozyme. Studying distinct thermal cycles, we notice that protein properties during this process are strongly affected by different energetic routes. Furthermore, a comparison between the behavior of these three peptide groups confirms that HBs play a role in protein folding. This is highlighted not only by the activation energy values that are of the same order of magnitude as in the HBs, but also by the magnetization $M(T)$ behavior of the methine groups in the native and the reversible unfolded phases. The higher molecular motility is caused by the "burial" effect of the HBs on the hydrophobic groups, which is particularly strong in the case of the methyl groups. The two forms of protein water, hydration water and internal water, are essential in protein folding. Because all water in the unfolded state belongs to the solvent, hydrogens in the amide groups with peptide bonds interact rapidly via HBs with H_2O. When the protein folds these interactions concern only internal water, which is linked with amides and buries the protein interiors. Thus, clusters of hydrophobic residues are formed in the folded protein and the methine groups are more mobile than the methyl groups. Figures 3.11, 3.12 and 3.13 also show that above T^* the role of hydration water becomes increasingly important and causes irreversible unfolding in the biopolymer, as T_D is approached. In the reversibility interval between T^* and T_D, the HB structure of the protein side chains allows the internal water to impose a persistent folded structure. All the measured activation energies quantitatively confirm this situation. Therefore, our findings validate the picture for which, in protein hydration, the internal water plays a very important role in "driving" the protein structure from a globular configuration to an open, unfolded configuration. In particular, this mechanism is due to the HB structure shared by water, carbonyl oxygen (C=O), and amidic proton (N–H).

Lastly, investigating the MSD of lysozyme hydration water, we have studied the changes in the diffusivity with the temperature and diffusion time Δ. For this aim, we have performed several measurements by means of PFGSTE NMR spectroscopy at different temperatures (295 K, 315 K, 335 K and 355 K) to investigate the region of folding-unfolding transition. Figure 3.14 and 3.15 showed the spin echo attenuation data: the decay of these data exhibits an increasing feature of nonlinearity as the denaturation region is approached ($T > 345$ K). The profile of this decay can be expressed by using an exponential function (see equation 2.66) and we find the presence of "anomalous" diffusion. In fact, as shown in figure 3.16, the mean-square displacement $\langle z^2 \rangle$ displays a power law dependence on observation time Δ (see equation 3.7). All these consideration prove again that, by increasing T and when protein reaches the unfold condition, the protein side chain obtain a greater motility due to the higher probability of HB breaking. Figure 3.17 reports the value of anomalous diffusion exponent α that increases with the temperature and there is a crossover at T^* in which $\alpha \approx 1$. This temperature represents the "magic point" at which the system undergoes from a condition in which $\alpha < 1$ (sub-diffusion) to $\alpha > 1$ (super-diffusion). Such a picture evidences the importance of T^*, not only in water, but generally in aqueous systems. In particular, our data confirm once more that, for $T < T^*$, water is able to form stable HBs, whereas for $T > T^*$, HBs lifetime and strength are much smaller and water behaves as a simple liquid.

In conclusion, in this thesis, the thermodynamics of water and biosystems have been extensively investigated, focusing, in particular, on the role of water in driving the properties of biosystems. We have experimentally studied the thermodynamics of the interaction between water and amphiphilic molecules starting with the simplest one (methanol) up to a more complex system, such as a protein (lysozyme). In this frame, we have highlighted the role played by hydrogen bonds and the relevance of several characteristic temperatures, e.g., T_L and T^*, in aqueous system processes. In fact, the considered

thermal range corresponds to a precise state for the hydrogen bonding (and hydrophobic effect) that determines, in an exclusive way, the physical properties of the examined system.

Bibliography

[1] D. Le Bihan, *Water - The Forgotten Biological Molecule*, edited by D. L. Bihan, and H. Fukuyama, (Pan Stanford Publishing Pte. Ltd., Nov. 2010), `http://www.panstanford.com/books/9789814267526.html`.

[2] R. M. Lynden-Bell, S. C. Morris, J. D. Barrow, J. L. Finney, and C. Harper, eds., *Water and Life: The Unique Properties of H_2O* (CRC Press; 1 edition, 2010).

[3] F. Franks, *Water, A matrix of life*, RSC Paperbacks (The Royal Society of Chemistry, 2000), pp. X001–X004, `http://dx.doi.org/10.1039/9781847552341`.

[4] H. E. Stanley, ed., *Liquid polymorphism* (John Wiley & Sons Inc., 2013), `https://doi.org/10.1002%2F9781118540350`.

[5] B. Bagchi, *Water in biological and chemical processes: from structure and dynamics to function*, Cambridge Molecular Science (Cambridge University Press, Dec. 2013), `https://doi.org/10.1017/CBO9781139583947`.

[6] P. Ball, *H_2O: A Biography of Water* (Weidenfeld & Nicolson, 1999).

[7] M. Chaplin, *Water structure and science*, `http://www1.lsbu.ac.uk/water/`.

[8] V. V. Goncharuk, *Drinking Water* (Springer International Publishing, 2014), `https://doi.org/10.1007%2F978-3-319-04334-0`.

[9] F. Franks, ed., *The physics and physical chemistry of water*, Vol. 1, Water: A Comprehensive Treatise (Springer US, 1972), `https://link.springer.com/book/10.1007%2F978-1-4684-8334-5`.

[10] F. H. Stillinger, "Theory and molecular models for water", in *Advances in chemical physics*, Vol. XXXI, edited by I. Prigogine, and S. A. Rice, (John Wiley & Sons Inc., 1975), pp. 1–101, `https://doi.org/10.1002%2F9780470143834.ch1`.

[11] Y. Maréchal, *The hydrogen bond and the water molecule* (Elsevier B.V., 2007), `http://www.sciencedirect.com/science/book/9780444519573`.

[12] F. Mallamace, C. Corsaro, D. Mallamace, S. Vasi, C. Vasi, P. Baglioni, S. V. Buldyrev, S.-H. Chen, and H. E. Stanley, "Energy landscape in protein folding and unfolding", Proc. Natl. Acad. Sci. USA **113**, 3159–3163 (2016), `https://doi.org/10.1073%2Fpnas.1524864113`.

[13] F. Mallamace, C. Corsaro, D. Mallamace, S. Vasi, C. Vasi, H. E. Stanley, and S.-H. Chen, "Some thermodynamical aspects of protein hydration water", The Journal of Chemical Physics **142**, 215103 (2015), `https://doi.org/10.1063%2F1.4921897`.

[14] M.-C. Bellissent-Funel, A. Hassanali, M. Havenith, R. Henchman, P. Pohl, F. Sterpone, D. van der Spoel, Y. Xu, and A. E. Garcia, "Water determines the structure and dynamics of proteins", Chemical Reviews **116**, 7673–7697 (2016), `https://doi.org/10.1021%2Facs.chemrev.5b00664`.

[15] F. Mallamace, C. Corsaro, D. Mallamace, S. Vasi, C. Vasi, and H. E. Stanley, "Thermodynamic properties of bulk and confined water", J. Chem. Phys. **141**, 18C504 (2014), http://aip.scitation.org/doi/10.1063/1.4895548.

[16] P. G. Debenedetti, and H. E. Stanley, "Supercooled and glassy water", Physics Today **56**, 40–46 (2003), http://physicstoday.scitation.org/doi/abs/10.1063/1.1595053.

[17] F. Franks, ed., *Water and aqueous solutions at subzero temperatures* (Springer US, 1982), https://doi.org/10.1007%2F978-1-4757-6952-4.

[18] C. L. Braun, and S. N. Smirnov, "Why is water blue?", Journal of Chemical Education **70**, 612 (1993), https://doi.org/10.1021%2Fed070p612.

[19] D. Eisenberg, and W. Kauzmann, *The structure and properties of water* (Oxford University Press, New York, 1969).

[20] W. M. Latimer, and W. H. Rodebush, "Polarity and ionization from the standpoint of the lewis theory of valence.", Journal of the American Chemical Society **42**, 1419–1433 (1920), https://doi.org/10.1021%2Fja01452a015.

[21] D. A. Smith, "A brief history of the hydrogen bond", in *Modeling the hydrogen bond*, Vol. 569, edited by D. A. Smith, ACS Symposium Series (American Chemical Society, 1994) Chap. 1, pp. 1–5, https://doi.org/10.1021%2Fbk-1994-0569.ch001.

[22] L. Pauling, *The nature of the chemical bond* (Cornell University Press, Ithaca, New York, 1960).

[23] S. J. Suresh, and V. M. Naik, "Hydrogen bond thermodynamic properties of water from dielectric constant data", The Journal of Chemical Physics **113**, 9727–9732 (2000), http://aip.scitation.org/doi/10.1063/1.1320822.

[24] I. Brovchenko, and A. Oleinikova, "Multiple phases of liquid water", ChemPhysChem **9**, 2660–2675 (2008), http://dx.doi.org/10.1002/cphc.200800639.

[25] L. G. M. Pettersson, R. H. Henchman, and A. Nilsson, "Water—the most anomalous liquid", Chemical Reviews **116**, 7459–7462 (2016), https://doi.org/10.1021%2Facs.chemrev.6b00363.

[26] A. Nilsson, and L. G. M. Pettersson, "The structural origin of anomalous properties of liquid water", Nature Communications **6**, 8998 (2015), https://doi.org/10.1038%2Fncomms9998.

[27] K. Stokely, M. G. Mazza, H. E. Stanley, and G. Franzese, "Effect of hydrogen bond cooperativity on the behavior of water", Proceedings of the National Academy of Sciences **107**, 1301–1306 (2010), http://www.pnas.org/content/107/4/1301.full.

[28] C. A. Angell, "Formation of glasses from liquids and biopolymers", Science **267**, 1924–1935 (1995).

[29] P. G. Debenedetti, "Supercooled and glassy water", Journal of Physics: Condensed Matter **15**, R1669–R1726 (2003).

[30] C. A. Angell, "Liquid fragility and the glass transition in water and aqueous solutions", Chemical Reviews **102**, 2627–2650 (2002).

[31] G. P. Johari, A. Hallbrucker, and E. Mayer, "The glass–liquid transition of hyperquenched water", Nature **330**, 552–553 (1987).

[32] A. Hallbrucker, E. Mayer, and G. P. Johari, "Glass-liquid transition and the enthalpy of devitrification of annealed vapor-deposited amorphous solid water: a comparison with hyperquenched glassy water", Journal of Physical Chemistry **93**, 4986–4990 (1989).

[33] O. Mishima, L. D. Calvert, and E. Whalley, "'Melting Ice' I at 77 K and 10 kbar: a new method of making amorphous solids", Nature **310**, 393–395 (1984).

[34] O. Mishima, L. D. Calvert, and E. Whalley, "An apparently first-order transition between two amorphous phases of ice induced by pressure", Nature **314**, 76–78 (1985), `https://doi.org/10.1038%2F314076a0`.

[35] O. Mishima, "Relationship between melting and amorphization of ice", Nature **384**, 546–549 (1996).

[36] G. S. Kell, "Density, thermal expansivity, and compressibility of liquid water from 0.deg. to 150.deg.. correlations and tables for atmospheric pressure and saturation reviewed and expressed on 1968 temperature scale", Journal of Chemical & Engineering Data **20**, 97–105 (1975), `https://doi.org/10.1021%2Fje60064a005`.

[37] National Institute of Standards and Technology (NIST), `http://webbook.nist.gov/`.

[38] W. M. Haynes, *CRC Handbook of Chemistry and Physics, 97th Edition* (CRC Press, 2016).

[39] G. P. Johari, A. Hallbrucker, and E. Mayer, "Two calorimetrically distinct states of liquid water below 150 Kelvin", Science **273**, 90–92 (1996), `https://doi.org/10.1126%2Fscience.273.5271.90`.

[40] S. Sastry, P. G. Debenedetti, F. Sciortino, and H. E. Stanley, "Singularity-free interpretation of the thermodynamics of supercooled water", Physical Review E **53**, 6144 (1996).

[41] H. Kanno, and C. A. Angell, "Water: anomalous compressibilities to 1.9 kbar and correlation with supercooling limits", The Journal of Chemical Physics **70**, 4008 (1979), `http://dx.doi.org/10.1063/1.438021`.

[42] R. J. Speedy, and C. A. Angell, "Isothermal compressibility of supercooled water and evidence for a thermodynamic singularity at -45°C", J. Chem. Phys. **65**, 851 (1976), `http://dx.doi.org/10.1063/1.433153`.

[43] S. Cerveny, F. Mallamace, J. Swenson, M. Vogel, and L. Xu, "Confined water as model of supercooled water", Chem. Rev. **116**, 7608–7625 (2016).

[44] G. E. Walrafen, and Y. C. Chu, "Shear viscosity, heat capacity, and fluctuations of liquid water, all at constant molal volume", J. Phys. Chem. **95**, 8909–8921 (1991).

[45] C. H. Cho, J. Urquidi, S. Singh, and G. W. Robinson, "Thermal offset viscosities of liquid H_2O, D_2O, and T_2O", J. Phys. Chem. B **103**, 1991–1994 (1999), `http://pubs.acs.org/doi/abs/10.1021/jp9842953`.

[46] C. H. Cho, J. Urquidi, and G. W. Robinson, "Molecular-level description of temperature and pressure effects on the viscosity of water", J. Chem. Phys. **111**, 10171 (1999).

[47] P. G. Debenedetti, and F. H. Stillinger, "Supercooled liquids and the glass transition", Nature **410**, 259–267 (2001).

[48] C. A. Angell, "Relaxation in liquids, polymers and plastic crystals – strong/fragile patterns and problems", J. Non-Cryst. Solids **131–133**, 13–31 (1991), `https://doi.org/10.1016/0022-3093(91)90266-9`.

[49] H. Vogel, "The law of the relationship between viscosity of liquids and the temperature", Phys. Z. **22**, 645–646 (1921).

[50] G. S. Fulcher, "Analysis of recent measurements of the viscosity of glasses", J. Am. Ceram. Soc. **8**, 339–355 (1925).

[51] G. Tamman, and W. Hesse, "Die abhängigkeit der viscosität von der temperatur bie unterkühlten flüssigkeiten", Zeitschrift für Anorganische und Allgemeine Chemie **156**, 245–257 (1926).

[52] K. Ito, C. T. Moynihan, and C. A. Angell, "Thermodynamic determination of fragility in liquids and a fragile-to-strong liquid transition in water", Nature **398**, 492–495 (1999).

[53] A. Faraone, L. Liu, C.-Y. Mou, C.-W. Yen, and S.-H. Chen, "Fragile-to-strong liquid transition in deeply supercooled confined water", J. Chem. Phys. **121**, 10843–10846 (2004).

[54] F. Mallamace, M. Broccio, C. Corsaro, A. Faraone, L. Liu, C. Y. Mou, and S. H. Chen, "Dynamical properties of confined supercooled water: an NMR study", J. Phys.: Condens. Matter **18**, S2285–S2297 (2006), `http://iopscience.iop.org/article/10.1088/0953-8984/18/36/S04/meta`.

[55] I. Chang, F. Fujara, B. Geil, G. Heuberger, T. Mangel, and H. Sillescu, "Translational and rotational molecular motion in supercooled liquids studied by NMR and forced Rayleigh scattering", J. Non-Cryst. Solids **172**, Relaxations in Complex Systems, 248 –255 (1994), `http://www.sciencedirect.com/science/article/pii/002230939490443X`.

[56] S. H. Chen, F. Mallamace, C. Y. Mou, M. Broccio, C. Corsaro, A. Faraone, and L. Liu, "The violation of the Stokes–Einstein relation in supercooled water", Proc. Natl. Acad. Sci. USA **103**, 12974–12978 (2006).

[57] P. Kumar, "Breakdown of the Stokes–Einstein relation in supercooled water", Proc. Natl. Acad. Sci. U.S.A. **103**, 12955–12956 (2006).

[58] W. S. Price, H. Ide, and Y. Arata, "Self-Diffusion of Supercooled Water to 238 K Using PGSE NMR Diffusion Measurements", J. Phys. Chem. A **103**, 448–450 (1999).

[59] J. H. Simpson, and H. Y. Carr, "Diffusion and nuclear spin relaxation in water", Phys. Rev. **111**, 1201 (1958).

[60] F. Mallamace, P. Baglioni, C. Corsaro, J. Spooren, H. E. Stanley, and S.-H. Chen, "Transport properties of supercooled confined water", Riv. Nuovo Cimento **34**, 253–388 (2011).

[61] O. Mishima, and H. E. Stanley, "The relationship between liquid, supercooled and glassy water", Nature **396**, 329–335 (1998).

[62] R. J. Speedy, "Stability-limit conjecture. An interpretation of the properties of water", J. Phys. Chem. **86**, 982–991 (1982).

[63] P. G. Debenedetti, and M. C. D'Antonio, "Stability and tensile strength of liquids exhibiting density maxima", AIChE Journal **34**, 447–455 (1988), `http://dx.doi.org/10.1002/aic.690340312`.

[64] S. Sastry, F. Sciortino, and H. E. Stanley, "Limits of stability of the liquid phase in a lattice model with water-like properties", J. Chem. Phys. **98**, 9863 (1993).

[65] M. Sasai, "The random graph model of hydrogen bond network", Bull. Chem. Soc. Jpn. **66**, 3362–3371 (1993).

[66] S. S. Borick, P. G. Debenedetti, and S. Sastry, "A lattice model of network-forming fluids with orientation-dependent bonding: equilibrium, stability, and implications for the phase behavior of supercooled water", J. Phys. Chem. **99**, 3781–3792 (1995).

[67] P. H. Poole, F. Sciortino, U. Essmann, and H. E. Stanley, "Spinodal of liquid water", Phys. Rev. E **48**, 3799–3817 (1993), `https://doi.org/10.1103/PhysRevE.48.3799`.

[68] L. P. N. Rebelo, P. G. Debenedetti, and S. Sastry, "Singularity-free interpretation of the thermodynamics of supercooled water. II. Thermal and volumetric behavior", J. Chem. Phys. **109**, 626–633 (1998), `http://dx.doi.org/10.1063/1.476600`.

[69] H. E. Stanley, and J. Teixeira, "Interpretation of the unusual behavior of H_2O and D_2O at low temperatures: tests of a percolation model", J. Chem. Phys. **73**, 3404–3422 (1980), `http://dx.doi.org/10.1063/1.440538`.

[70] P. H. Poole, F. Sciortino, U. Essmann, and H. E. Stanley, "Phase behaviour of metastable water", Nature **360**, 324–328 (1992).

[71] F. H. Stillinger, and A. Rahman, "Improved simulation of liquid water by molecular dynamics", J. Chem. Phys. **60**, 1545 (1974), `http://dx.doi.org/10.1063/1.1681229`.

[72] W. L. Jorgensen, J. Chandrasekhar, J. D. Madura, R. W. Impey, and M. L. Klein, "Comparison of simple potential functions for simulating liquid water", J. Chem. Phys. **79**, 926 (1983), `http://dx.doi.org/10.1063/1.445869`.

[73] F. Sciortino, P. H. Poole, U. Essmann, and H. E. Stanley, "Line of compressibility maxima in the phase diagram of supercooled water", Phys. Rev. E **55**, 727 (1997), `https://doi.org/10.1103/PhysRevE.55.727`.

[74] M. Yamada, S. Mossa, H. E. Stanley, and F. Sciortino, "Interplay between time-temperature transformation and the liquid-liquid phase transition in water", Phys. Rev. Lett. **88**, 195701 (2002), `https://doi.org/10.1103/PhysRevLett.88.195701`.

[75] O. Mishima, and H. E. Stanley, "Decompression-Induced Melting of Ice IV and the Liquid- Liquid Transition in Water", Nature **392**, 164–168 (1998).

[76] L. Liu, S.-H. Chen, A. Faraone, C.-W. Yen, and C.-Y. Mou, "Pressure Dependence of Fragile-to-Strong Transition and a Possible Second Critical Point in Supercooled Confined Water", Phys. Rev. Lett. **95**, 117802 (2005), `https://link.aps.org/doi/10.1103/PhysRevLett.95.117802`.

[77] L. Liu, S.-H. Chen, A. Faraone, C.-W. Yen, C.-Y. Mou, A. I. Kolesnikov, E. Mamontov, and J. Leao, "Quasielastic and inelastic neutron scattering investigation of fragile-to-strong crossover in deeply supercooled water confined in nanoporous silica matrices", J. Phys.: Condens. Matter **18**, S2261–S2284 (2006), `https://doi.org/10.1088/0953-8984/18/36/S03`.

[78] L. Xu, P. Kumar, S. V. Buldyrev, S.-H. Chen, P. H. Poole, F. Sciortino, and H. E. Stanley, "Relation between the Widom Line and the Dynamic Crossover in Systems with a Liquid-Liquid Critical Point", Proc. Natl. Acad. Sci. **102**, 16558–16562 (2005).

[79] G. Adam, and J. Gibbs, "On the temperature dependence of cooperative relaxation properties in glass-forming liquids", J. Chem. Phys. **43**, 139–146 (1965), `http://dx.doi.org/10.1063/1.1696442`.

[80] Z. Sun, G. Sun, Y. Chen, and L. Xu, "Liquid-liquid phase transition in water", Science China Physics, Mechanics & Astronomy **57**, 810–818 (2014), `http://dx.doi.org/10.1007/s11433-014-5451-z`.

[81] F. Franks, ed., *Aqueous solutions of amphiphiles and macromolecules*, Vol. 4, Water: A Comprehensive Treatise (Springer US, 1975), `http://www.springer.com/gp/book/9781468429602`.

[82] D. Chandler, "Interfaces and the driving force of hydrophobic assembly", Nature **437**, 640–647 (2005), `http://dx.doi.org/10.1038/nature04162`.

[83] C. Tanford, *The hydrophobic effect: formation of micelles and biological membranes*, 2nd edition (Wiley, 1980).

[84] F. Mallamace, C. Corsaro, D. Mallamace, C. Vasi, S. Vasi, and H. E. Stanley, "Dynamical properties of water-methanol solutions", J. Chem. Phys. **144**, 064506 (2016).

[85] R. A. Jones, *Soft condensed matter*, Oxford Master Series in Physics (Oxford University Press, Aug. 2002).

[86] P. Alexandridis, and B. Lindman, eds., *Amphiphilic block copolymers: self-assembly and applications* (Elsevier Science, Oct. 2000).

[87] A. H. Narten, and A. Habenschuss, "Hydrogen bonding in liquid methanol and ethanol determined by x-ray diffraction", J. Chem. Phys. **80**, 3387–3391 (1984), `http://dx.doi.org/10.1063/1.447093`.

[88] S. Sarkar, and R. N. Joarder, "Molecular clusters and correlations in liquid methanol at room temperature", J. Chem. Phys. **99**, 2032–2039 (1993), `http://dx.doi.org/10.1063/1.465266`.

[89] H. S. Frank, and M. W. Evans, "Free volume and entropy in condensed systems iii. entropy in binary liquid mixtures; partial molal entropy in dilute solutions; structure and thermodynamics in aqueous electrolytes", J. Chem. Phys. **13**, 507 (1945), `http://dx.doi.org/10.1063/1.1723985`.

[90] R. E. Gibson, "The compressions and specific volumes of aqueous solutions of resorcinol and methanol at 25° and the behavior of water in these solutions", J. Am. Chem. Soc. **57**, 1551–1557 (1935), `http://dx.doi.org/10.1021/ja01312a013`.

[91] W. Kauzmann, "Some factors in the interpretation of protein denaturation", Adv. Protein Chem. **14**, 1–63 (1959), `http://www.sciencedirect.com/science/article/pii/S0065323308606087`.

[92] S. Z. Mikhail, and W. R. Kimel, "Densities and viscosities of methanol-water mixtures.", J. Chem. Eng. Data **6**, 533–537 (1961), `http://dx.doi.org/10.1021/je60011a015`.

[93] H. Schott, "Hydration of primary alcohols", J. Chem. Eng. Data **14**, 237–239 (1969), `http://dx.doi.org/10.1021/je60041a004`.

[94]   Z. J. Derlacki, A. J. Easteal, A. V. J. Edge, L. A. Woolf, and Z. Roksandic, "Diffusion coefficients of methanol and water and the mutual diffusion coefficient in methanol-water solutions at 278 and 298 K", J. Phys. Chem. **89**, 5318–5322 (1985), http://dx.doi.org/10.1021/j100270a039.

[95]   L. A. Woolf, "Insights into solute-solute-solvent interactions from transport property measurements with particular reference to methanol-water mixtures and their constituents", Pure Appl. Chem. **57**, 1083–1090 (1985), http://dx.doi.org/10.1351/pac198557081083.

[96]   A. J. Easteal, and L. A. Woolf, "(p, V_m, T, x) measurements for [(1 - x)H_2O + xCH_3OH] in the range 278 to 323 K and 0.1 to 280 MPa I. Experimental results, isothermal compressibilities, thermal expansivities, and partial molar volumes", J. Chem. Thermodyn. **17**, 49–62 (1985), http://www.sciencedirect.com/science/article/pii/002196148590031X.

[97]   A. J. Easteal, and L. A. Woolf, "(p, V_m, T, x) measurements for [(1 - x)H_2O + xCH_3OH] in the range 278 to 323 K and 0.1 to 280 MPa II. Thermodynamic excess properties", J. Chem. Thermodyn. **17**, 69–82 (1985), http://www.sciencedirect.com/science/article/pii/0021961485900333.

[98]   A. K. Soper, and J. L. Finney, "Hydration of methanol in aqueous solution", Phys. Rev. Lett. **71**, 4346–4349 (1993), https://link.aps.org/doi/10.1103/PhysRevLett.71.4346.

[99]   N. Micali, S. Trusso, C. Vasi, D. Blaudez, and F. Mallamace, "Dynamical properties of water-methanol solutions studied by depolarized Rayleigh scattering", Phys. Rev. E **54**, 1720–1724 (1996), https://link.aps.org/doi/10.1103/PhysRevE.54.1720.

[100] F. Aliotta, C. Vasi, G. Maisano, D. Majolino, F. Mallamace, and P. Migliardo, "Role of the H bond and cooperative effects in normal and supercooled water studied by anisotropic low frequency light scattering", J. Chem. Phys. **84**, 4731–4738 (1986), http://dx.doi.org/10.1063/1.450007.

[101] O. Conde, and J. Teixeira, "Depolarized light scattering of heavy water, and hydrogen bond dynamics", Mol. Phys. **53**, 951–959 (1984), http://dx.doi.org/10.1080/00268978400102761.

[102] F. Franks, ed., *Water in Crystalline Hydrates Aqueous Solutions of Simple Non-electrolytes*, Vol. 2, Water: A Comprehensive Treatise (Springer US, 1973), http://www.springer.com/it/book/9781475769609.

[103] H. Tanaka, and K. E. Gubbins, "Structure and thermodynamic properties of water-methanol mixtures: Role of the water-water interaction", J. Chem. Phys. **97**, 2626–2634 (1992), http://dx.doi.org/10.1063/1.463051.

[104] S. Dixit, W. C. K. Poon, and J. Crain, "Hydration of methanol in aqueous solutions: a raman spectroscopic study", J. Phys.: Condens. Matter **12**, L323 (2000), http://stacks.iop.org/0953-8984/12/i=21/a=103.

[105] S. Dixit, J. Crain, W. C. K. Poon, J. L. Finney, and A. K. Soper, "Molecular segregation observed in a concentrated alcohol-water solution", Nature **416**, 829–832 (2002), http://dx.doi.org/10.1038/416829a.

[106] A. Soper, "The radial distribution functions of water and ice from 220 to 673 K and at pressures up to 400 MPa", Chem. Phys. **258**, 121–137 (2000), http://www.sciencedirect.com/science/article/pii/S030101040000001798.

[107] T. Yamaguchi, K. Hidaka, and A. K. Soper, "The structure of liquid methanol revisited: a neutron diffraction experiment at -80 °C and +25 °C", Mol. Phys. **96**, 1159–1168 (1999), http://dx.doi.org/10.1080/00268979909483060.

[108] J. L. Finney, D. T. Bowron, R. M. Daniel, P. A. Timmins, and M. A. Roberts, "Molecular and mesoscale structures in hydrophobically driven aqueous solutions", Biophys. Chem. **105**, 391–409 (2003), http://www.sciencedirect.com/science/article/pii/S0301462203001042.

[109] J.-H. Guo, Y. Luo, A. Augustsson, S. Kashtanov, J.-E. Rubensson, D. K. Shuh, H. Ågren, and J. Nordgren, "Molecular Structure of Alcohol-Water Mixtures", Phys. Rev. Lett. **91**, 157401–4 (2003), https://link.aps.org/doi/10.1103/PhysRevLett.91.157401.

[110] L. Dougan, S. P. Bates, R. Hargreaves, J. P. Fox, J. Crain, J. L. Finney, V. Réat, and A. K. Soper, "Methanol-water solutions: A bi-percolating liquid mixture", J. Chem. Phys. **121**, 6456–6462 (2004), http://dx.doi.org/10.1063/1.1789951.

[111] D. T. Bowron, J. L. Finney, and A. K. Soper, "Structural Investigation of Solute-Solute Interactions in Aqueous Solutions of Tertiary Butanol", J. Phys. Chem. B **102**, 3551–3563 (1998), http://dx.doi.org/10.1021/jp972780c.

[112] D. T. Bowron, A. K. Soper, and J. L. Finney, "Temperature dependence of the structure of a 0.06 mole fraction tertiary butanol-water solution", J. Chem. Phys. **114**, 6203–6219 (2001), http://dx.doi.org/10.1063/1.1354167.

[113] S. K. Allison, J. P. Fox, R. Hargreaves, and S. P. Bates, "Clustering and microimmiscibility in alcohol-water mixtures: Evidence from molecular-dynamics simulations", Phys. Rev. B **71**, 024201 (2005), https://link.aps.org/doi/10.1103/PhysRevB.71.024201.

[114] A. K. Soper, L. Dougan, J. Crain, and J. L. Finney, "Excess Entropy in Alcohol-Water Solutions: A Simple Clustering Explanation", J. Phys. Chem. B **110**, PMID: 16494400, 3472–3476 (2006), http://dx.doi.org/10.1021/jp054556q.

[115] C. Corsaro, J. Spooren, C. Branca, N. Leone, M. Broccio, C. Kim, S.-H. Chen, H. E. Stanley, and F. Mallamace, "Clustering Dynamics in Water/Methanol Mixtures: A Nuclear Magnetic Resonance Study at 205 K < T < 295 K", J. Phys. Chem. B **112**, PMID: 18672927, 10449–10454 (2008), http://dx.doi.org/10.1021/jp803456p.

[116] C. Corsaro, R. Maisano, D. Mallamace, and G. Dugo, "1H NMR study of water/methanol solutions as a function of temperature and concentration", Physica A **392**, 596–601 (2013), http://www.sciencedirect.com/science/article/pii/S0378437112009739.

[117] G. Guevara-Carrion, J. Vrabec, and H. Hasse, "Prediction of self-diffusion coefficient and shear viscosity of water and its binary mixtures with methanol and ethanol by molecular simulation", J. Chem. Phys. **134**, 074508 (2011), http://dx.doi.org/10.1063/1.3515262.

[118] F. Kurata, T. W. Yergovich, and G. W. Swift, "Density and viscosity of aqueous solutions of methanol and acetone from the freezing point to 10.deg.", J. Chem. Eng. Data **16**, 222–226 (1971), http://dx.doi.org/10.1021/je60049a004.

[119] M. Nagasaka, K. Mochizuki, V. Leloup, and N. Kosugi, "Local Structures of Methanol-Water Binary Solutions Studied by Soft X-ray Absorption Spectroscopy", J. Phys. Chem. B **118**, PMID: 24694018, 4388–4396 (2014), `http://dx.doi.org/10.1021/jp4091602`.

[120] F. Franks, *Characterization of proteins* (Humana Press, 1988), `http://www.springer.com/la/book/9780896031098`.

[121] Y. Levy, and J. N. Onuchic, "Water mediation in protein folding and molecular recognition", Annu. Rev. Biophys. Biomol. Struct. **35**, 389–415 (2006), `https://doi.org/10.1146/annurev.biophys.35.040405.102134`.

[122] W. Doster, A. Bachleitner, R. Dunau, M. Hiebl, and E. Lüscher, "Thermal properties of water in myoglobin crystals and solutions at subzero temperatures.", Biophys. J. **50**, 213–219 (1986), `http://www.ncbi.nlm.nih.gov/pmc/articles/PMC1329738/`.

[123] J. A. Rupley, and G. Careri, "Protein hydration and function", Adv. Protein Chem. **41**, 37–172 (1991), `http://www.sciencedirect.com/science/article/pii/S0065323308601977`.

[124] S. Ebbinghaus, S. J. Kim, M. Heyden, X. Yu, U. Heugen, M. Gruebele, D. M. Leitner, and M. Havenith, "An extended dynamical hydration shell around proteins", Proc. Natl. Acad. Sci. U.S.A. **104**, 20749–20752 (2007), `http://www.pnas.org/content/104/52/20749.full`.

[125] S. Bandyopadhyay, S. Chakraborty, and B. Bagchi, "Secondary structure sensitivity of hydrogen bond lifetime dynamics in the protein hydration layer", J. Am. Chem. Soc. **127**, PMID: 16305255, 16660–16667 (2005), `http://dx.doi.org/10.1021/ja054462u`.

[126] A. Oleinikova, N. Smolin, I. Brovchenko, A. Geiger, and R. Winter, "Formation of Spanning Water Networks on Protein Surfaces via 2D Percolation Transition", J. Phys. Chem. B **109**, PMID: 16851183, 1988–1998 (2005), `http://dx.doi.org/10.1021/jp045903j`.

[127] N. Smolin, A. Oleinikova, I. Brovchenko, A. Geiger, and R. Winter, "Properties of spanning water networks at protein surfaces", J. Phys. Chem. B **109**, PMID: 16852340, 10995–11005 (2005), `http://dx.doi.org/10.1021/jp050153e`.

[128] M. Nakasako, "Water–protein interactions from high–resolution protein crystallography", Phil. Trans. R. Soc. Lond. B **359**, 1191–1206 (2004), `http://rstb.royalsocietypublishing.org/content/359/1448/1191`.

[129] I. Brovchenko, and A. Oleinikova, "Which properties of a spanning network of hydration water enable biological functions?", ChemPhysChem **9**, 2695–2702 (2008), `http://dx.doi.org/10.1002/cphc.200800662`.

[130] A. Paciaroni, S. Cinelli, E. Cornicchi, A. D. Francesco, and G. Onori, "Fast fluctuations in protein powders: the role of hydration", Chem. Phys. Lett. **410**, 400–403 (2005), `http://www.sciencedirect.com/science/article/pii/S0009261405008079`.

[131] M. S. Cheung, A. E. García, and J. N. Onuchic, "Protein folding mediated by solvation: water expulsion and formation of the hydrophobic core occur after the structural collapse", Proc. Natl. Acad. Sci. USA **99**, 685–690 (2002), `http://www.pnas.org/content/99/2/685.abstract`.

[132] L. Pauling, R. B. Corey, and H. R. Branson, "The structure of proteins: Two hydrogen-bonded helical configurations of the polypeptide chain", Proc. Natl. Acad. Sci. USA **37**, 205–211 (1951), `http://www.pnas.org/content/37/4/205.short`.

[133] S. Chakraborty, S. K. Sinha, and S. Bandyopadhyay, "Low-Frequency Vibrational Spectrum of Water in the Hydration Layer of a Protein: A Molecular Dynamics Simulation Study", J. Phys. Chem. B **111**, PMID: 17994720, 13626–13631 (2007), `http://dx.doi.org/10.1021/jp0746401`.

[134] A. J. Rowe, "Probing hydration and the stability of protein solutions – a colloid science approach", Biophys. Chem. **93**, The hydration problems in Solution biophysics, 93–101 (2001), `http://www.sciencedirect.com/science/article/pii/S0301462201002149`.

[135] D. Vitkup, D. Ringe, G. A. Petsko, and M. Karplus, "Solvent mobility and the protein 'glass' transition", Nat. Struct. Mol. Biol. **7**, 34–38 (2000), `http://dx.doi.org/10.1038/71231`.

[136] S.-H. Chen, L. Liu, E. Fratini, P. Baglioni, A. Faraone, and E. Mamantov, "Observation of fragile-to-strong dynamic crossover in protein hydration water", Proc. Natl. Acad. Sci. U.S.A. **103**, 9012–9016 (2006), `http://www.pnas.org/content/103/24/9012.full`.

[137] F. Mallamace, C. Corsaro, D. Mallamace, P. Baglioni, H. E. Stanley, and S.-H. Chen, "A possible role of water in the protein folding process", J. Phys. Chem. B **115**, 14280–14294 (2011), `http://pubs.acs.org/doi/abs/10.1021/jp205285t`.

[138] G. Zaccai, "The effect of water on protein dynamics", Phil. Trans. R. Soc. Lond. B **359**, 1269–1275 (2004), `http://rstb.royalsocietypublishing.org/content/359/1448/1269`.

[139] Research Collaboratory for Structural Bioinformatics: Protein Data Bank, `https://www.rcsb.org/pdb/home/home.do`.

[140] E. Hsi, and R. G. Bryant, "Nuclear magnetic resonance relaxation in frozen lysozyme solutions", J. Am. Chem. Soc. **97**, 3220–3221 (1975), `http://dx.doi.org/10.1021/ja00844a051`.

[141] F. Cavatorta, M. P. Fontana, and A. Vecli, "Raman spectroscopy of protein-water interactions in aqueous solutions", J. Chem. Phys. **65**, 3635–3640 (1976), `http://dx.doi.org/10.1063/1.433549`.

[142] B. D. Hilton, E. Hsi, and R. G. Bryant, "Proton nuclear magnetic resonance relaxation of water on lysozyme powders", J. Am. Chem. Soc. **99**, 8483–8490 (1977), `http://dx.doi.org/10.1021/ja00468a017`.

[143] Y. Fujita, and Y. Noda, "Effect of hydration on the thermal denaturation of lysozyme as measured by differential scanning calorimetry", Bull. Chem. Soc. Jpn. **51**, 1567–1568 (1978), `https://doi.org/10.1246/bcsj.51.1567`.

[144] S. R. Samanta, and G. E. Walrafen, "Raman intensities and interactions in aqueous lysozyme solutions", J. Chem. Phys. **68**, 3313–3315 (1978), `http://dx.doi.org/10.1063/1.436140`.

[145] P.-H. Yang, and J. A. Rupley, "Protein-water interactions. Heat capacity of the lysozyme-water system", Biochemistry **18**, PMID: 444485, 2654–2661 (1979), `http://dx.doi.org/10.1021/bi00579a035`.

[146] F. Aliotta, M. P. Fontana, R. Giordano, P. Migliardo, and F. Wanderlingh, "Raman scattering in lysozyme solutions", J. Chem. Phys. **75**, 4307–4309 (1981), `http://dx.doi.org/10.1063/1.442636`.

[147] P. L. Poole, and J. L. Finney, "Sequential hydration of a dry globular protein", Biopolymers **22**, 255–260 (1983), `http://dx.doi.org/10.1002/bip.360220135`.

[148] D. Bourret, and J. Parello, "Hydration of lysozyme in aqueous solution as studied by self-diffusion nmr measurements and by kerr-dielectric relaxation", J. Phys. Colloques **45**, C7–255–C7–258 (1984), `https://doi.org/10.1051/jphyscol:1984729`.

[149] J. E. Schinkel, N. W. Downer, and J. A. Rupley, "Hydrogen exchange of lysozyme powders. Hydration dependence of internal motions", Biochemistry **24**, PMID: 3978078, 352–366 (1985), `http://dx.doi.org/10.1021/bi00323a018`.

[150] G. Salvetti, E. Tombari, L. Mikheeva, and G. P. Johari, "The endothermic effects during denaturation of lysozyme by temperature modulated calorimetry and an intermediate reaction equilibrium", J. Phys. Chem. B **106**, 6081–6087 (2002), `http://dx.doi.org/10.1021/jp025587d`.

[151] A. Sokolov, J. Roh, E. Mamontov, and V. G. Sakai, "Role of hydration water in dynamics of biological macromolecules", Chem. Phys. **345**, Neutrons in Biology, 212–218 (2008), `http://www.sciencedirect.com/science/article/pii/S0301010407002881`.

[152] F. Mallamace, S.-H. Chen, M. Broccio, C. Corsaro, V. Crupi, D. Majolino, V. Venuti, P. Baglioni, E. Fratini, C. Vannucci, and H. E. Stanley, "Role of the solvent in the dynamical transitions of proteins: the case of the lysozyme-water system", J. Chem. Phys. **127**, 045104 (2007), `http://dx.doi.org/10.1063/1.2757171`.

[153] M. Lagi, X. Chu, C. Kim, F. Mallamace, P. Baglioni, and S.-H. Chen, "The Low-Temperature Dynamic Crossover Phenomenon in Protein Hydration Water: Simulations vs Experiments", J. Phys. Chem. B **112**, PMID: 18205352, 1571–1575 (2008), `http://dx.doi.org/10.1021/jp710714j`.

[154] G. Zaccai, "How Soft Is a Protein? A Protein Dynamics Force Constant Measured by Neutron Scattering", Science **288**, 1604–1607 (2000), `http://science.sciencemag.org/content/288/5471/1604`.

[155] D. Mallamace, C. Corsaro, C. Vasi, S. Vasi, G. Dugo, and F. Mallamace, "The protein irreversible denaturation studied by means of the bending vibrational mode", Physica A **412**, 39–44 (2014), `https://doi.org/10.1016%2Fj.physa.2014.06.007`.

[156] F. Mallamace, C. Corsaro, D. Mallamace, S. Vasi, C. Vasi, and G. Dugo, "The role of water in protein's behavior: the two dynamical crossovers studied by NMR and FTIR techniques", Comput. Struct. Biotechnol. J. **13**, 33–37 (2015), `https://doi.org/10.1016%2Fj.csbj.2014.11.007`.

[157] F. Mallamace, C. Corsaro, D. Mallamace, N. Cicero, S. Vasi, G. Dugo, and H. E. Stanley, "Dynamical changes in hydration water accompanying lysozyme thermal denaturation", Frontiers of Physics **10** (2015) `10.1007/s11467-015-0486-9`, `https://doi.org/10.1007%2Fs11467-015-0486-9`.

[158]   S. Vasi, C. Corsaro, D. Mallamace, and F. Mallamace, "The time dependence dynamics of hydration water changes upon crossing T*", Nuovo Cimento C **39**, 308 (1–9) (2016).

[159]   P. Zeeman, "Vii. doublets and triplets in the spectrum produced by external magnetic forces", Philos. Mag. **44**, 55–60 (1897), http://dx.doi.org/10.1080/14786449708621028.

[160]   W. Gerlach, and O. Stern, "Der experimentelle nachweis des magnetischen moments des silberatoms", Zeitschrift für Physik **8**, 110–111 (1922), http://dx.doi.org/10.1007/BF01329580.

[161]   I. I. Rabi, J. M. B. Kellogg, and J. R. Zacharias, "The magnetic moment of the proton", Phys. Rev. **46**, 157–163 (1934), https://link.aps.org/doi/10.1103/PhysRev.46.157.

[162]   E. M. Purcell, H. C. Torrey, and R. V. Pound, "Resonance absorption by nuclear magnetic moments in a solid", Phys. Rev. **69**, 37–38 (1946), https://link.aps.org/doi/10.1103/PhysRev.69.37.

[163]   F. Bloch, W. W. Hansen, and M. Packard, "The nuclear induction experiment", Phys. Rev. **70**, 474–485 (1946), https://link.aps.org/doi/10.1103/PhysRev.70.474.

[164]   A. Abragam, *The principles of nuclear magnetism* (Oxford, Oxford, UK, 1961).

[165]   R. W. Brown, Y.-C. N. Cheng, E. M. Haacke, M. R. Thompson, and R. Venkatesan, eds., *Magnetic Resonance Imaging: Physical Principles and Sequence Design*, Second Edition (John Wiley & Sons, 2014), http://onlinelibrary.wiley.com/book/10.1002/9781118633953.

[166]   M. H. Levitt, *Spin dynamics: basics of nuclear magnetic resonance*, 2nd Edition (John Wiley & Sons Inc, 2008).

[167]   E. D. Becker, *High Resolution NMR: Theory and Chemical Applications* (ELSEVIER LTD, Oct. 11, 1999), 424 pp.

[168]   W. S. Price, *Nmr studies of translational motion: principles and applications*, Cambridge Molecular Science (Cambridge University Press, 2009).

[169]   G. H. Sørland, *Dynamic pulsed-field-gradient nmr*, Vol. 114, Springer Series in Chemical Physics (Springer Berlin Heidelberg, Sept. 20, 2014), 354 pp., https://link.springer.com/book/10.1007%2F978-3-662-44500-6.

[170]   T. D. W. Claridge, *High-Resolution NMR Techniques in Organic Chemistry* (Elsevier Science, 2016).

[171]   E. Butler, *AVANCE. Con SGU per la generazione di frequenza. Manuale per Principianti. Versione Italiana.* Questo manuale è stato tradotto da Anna Minoja ed altri, Bruker Biospin Italia S.r.l., Bruker Biospin GmbH (2003).

[172]   E. O. Stejskal, and J. E. Tanner, "Spin diffusion measurements: spin echoes in the presence of a time-dependent field gradient", J. Chem. Phys. **42**, 288–292 (1965), http://dx.doi.org/10.1063/1.1695690.

[173]   E. L. Hahn, "Spin echoes", Phys. Rev. **80**, 580–594 (1950), https://link.aps.org/doi/10.1103/PhysRev.80.580.

[174]   H. Y. Carr, and E. M. Purcell, "Effects of diffusion on free precession in nuclear magnetic resonance experiments", Phys. Rev. **94**, 630–638 (1954), https://journals.aps.org/pr/abstract/10.1103/PhysRev.94.630.

[175] W. S. Price, "Pulsed-field gradient nuclear magnetic resonance as a tool for study-ing translational diffusion: part 1. basic theory", Concepts Magn. Reson. **9**, 299–336 (1997), `https://goo.gl/LJ7eu4`.

[176] G. H. Sørland, "Short-time pfgste diffusion measurements", J. Magn. Reson. **126**, 146–148 (1997), `https://doi.org/10.1006/jmre.1997.1154`.

[177] J. Stepišnik, "Validity limits of gaussian approximation in cumulant expansion for diffusion attenuation of spin echo", Physica B **270**, 110–117 (1999), `http://www.sciencedirect.com/science/article/pii/S0921452699900160X`.

[178] H. Walderhaug, and B. Nyström, "Anomalous diffusion in an aqueous system of a poly(ethylene oxide)-poly(propylene oxide)-poly(ethylene oxide) triblock copolymer during gelation studied by pulsed field gradient nmr", J. Phys. Chem. B **101**, 1524–1528 (1997), `http://pubs.acs.org/doi/abs/10.1021/jp962197g`.

[179] J. Stepišnik, "Averaged propagator of restricted motion from the gaussian approx-imation of spin echo", Physica B **344**, 214–223 (2004), `http://www.sciencedirect.com/science/article/pii/S0921452603009177`.

[180] J.-H. Chen, and S. Singer, "Chapter 4 - High-Resolution Magic Angle Spin-ning NMR Spectroscopy", in *The handbook of metabonomics and metabolomics*, edited by J. C. Lindon, J. K. Nicholson, and E. Holmes, (Elsevier Science B.V., Amsterdam, 2007), pp. 113–147, `http://www.sciencedirect.com/science/article/pii/B9780444528414500059`.

[181] E. R. Andrew, A. Bradbury, and R. G. Eades, "Removal of dipolar broadening of nuclear magnetic resonance spectra of solids by specimen rotation", Nature **183**, 1802–1803 (1959), `http://dx.doi.org/10.1038/1831802a0`.

[182] I. J. Lowe, "Free induction decays of rotating solids", Phys. Rev. Lett. **2**, 285–287 (1959), `https://link.aps.org/doi/10.1103/PhysRevLett.2.285`.

[183] F. Engelke, *High Resolution Magic Angle Spinning Spectroscopy*, Bruker Elek-tronik GmbH (1998).

[184] W. L. Fitch, G. Detre, C. P. Holmes, J. N. Shoolery, and P. A. Keifer, "High-Resolution 1H NMR in Solid-Phase Organic Synthesis", J. Org. Chem. **59**, 7955–7956 (1994), `http://dx.doi.org/10.1021/jo00105a006`.

[185] J. C. Lindon, O. P. Beckonert, E. Holmes, and J. K. Nicholson, "High-resolution magic angle spinning NMR spectroscopy: Application to biomedical studies", Prog. Nucl. Magn. Reson. Spectrosc. **55**, 79–100 (2009), `https://doi.org/10.1016/j.pnmrs.2008.11.004`.

[186] O. Beckonert, M. Coen, H. C. Keun, Y. Wang, T. M. D. Ebbels, E. Holmes, J. C. Lindon, and J. K. Nicholson, "High-resolution magic-angle-spinning NMR spec-troscopy for metabolic profiling of intact tissues", Nat. Protocols **5**, 1019–1032 (2010), `http://dx.doi.org/10.1038/nprot.2010.45`.

[187] C. Corsaro, N. Cicero, D. Mallamace, S. Vasi, C. Naccari, A. Salvo, S. V. Giofrè, and G. Dugo, "HR-MAS and NMR towards Foodomics", Food Res. Int. **89**, 4th Foodomics Conference - Food for the World, 1085–1094 (2016), `http://www.sciencedirect.com/science/article/pii/S0963996916304240`.

[188] W. Götze, and L. Sjögren, "Relaxation processes in supercooled liquids", Rep. Prog. Phys. **55**, 241 (1992), http://stacks.iop.org/0034-4885/55/i=3/a=001.

[189] T. DeFries, and J. Jonas, "Pressure dependence of NMR proton spin-lattice relaxation times and shear viscosity in liquid water in the temperature range -15–10 °C", J. Chem. Phys. **66**, 896–901 (1977), http://dx.doi.org/10.1063/1.433995.

[190] F. Mallamace, C. Corsaro, and H. E. Stanley, "A singular thermodynamically consistent temperature at the origin of the anomalous behavior of liquid water", Sci. Rep. **2**, 993 (2012), http://dx.doi.org/10.1038/srep00993.

[191] F. Mallamace, M. Broccio, C. Corsaro, A. Faraone, D. Majolino, V. Venuti, L. Liu, C.-Y. Mou, and S.-H. Chen, "Evidence of the existence of the low-density liquid phase in supercooled, confined water", Proc. Natl. Acad. Sci. U.S.A. **104**, 424–428 (2007), http://www.pnas.org/content/104/2/424.abstract.

[192] M. Karplus, "Behind the folding funnel diagram", Nat. Chem. Biol. **7**, 401–404 (2011).

[193] W. Götze, *Complex Dynamics of Glass-Forming Liquids: A Mode-Coupling Theory*, International Series of Monographs on Physics (Oxford University Press, 2009).

[194] F. Mallamace, C. Corsaro, H. E. Stanley, and S.-H. Chen, "The role of the dynamic crossover temperature and the arrest in glass-forming fluids", Eur. Phys. J. E **34**, 94 (2011), https://doi.org/10.1140/epje/i2011-11094-7.

[195] G. Sartor, A. Hallbrucker, and E. Mayer, "Characterizing the secondary hydration shell on hydrated myoglobin, hemoglobin, and lysozyme powders by its vitrification behavior on cooling and its calorimetric glass–>liquid transition and crystallization behavior on reheating.", Biophys. J. **69**, 2679–2694 (1995), http://www.ncbi.nlm.nih.gov/pmc/articles/PMC1236505/.

[196] M. Fomina, G. Schirò, and A. Cupane, "Hydration dependence of myoglobin dynamics studied with elastic neutron scattering, differential scanning calorimetry and broadband dielectric spectroscopy", Biophys. Chem. **185**, 25–31 (2014), http://www.sciencedirect.com/science/article/pii/S0301462213001968.

[197] Z. Wang, E. Fratini, M. Li, P. Le, E. Mamontov, P. Baglioni, and S.-H. Chen, "Hydration-dependent dynamic crossover phenomenon in protein hydration water", Phys. Rev. E **90**, 042705 (2014), https://link.aps.org/doi/10.1103/PhysRevE.90.042705.

[198] S.-H. Chong, "Connections of activated hopping processes with the breakdown of the Stokes-Einstein relation and with aspects of dynamical heterogeneities", Phys. Rev. E **78**, 041501 (2008), https://link.aps.org/doi/10.1103/PhysRevE.78.041501.

[199] F. Sterpone, G. Stirnemann, and D. Laage, "Magnitude and molecular origin of water slowdown next to a protein", J. Am. Chem. Soc. **134**, PMID: 22335572, 4116–4119 (2012), http://dx.doi.org/10.1021/ja3007897.

[200] B. Jana, S. Pal, and B. Bagchi, "Hydration dynamics of protein molecules in aqueous solution: unity among diversity#", J. Chem. Sci. **124**, 317–325 (2012), https://doi.org/10.1007/s12039-012-0231-7.

[201] S. Perticaroli, L. Comez, P. Sassi, M. Paolantoni, S. Corezzi, S. Caponi, A. Morresi, and D. Fioretto, "Hydration and aggregation of lysozyme by extended frequency range depolarized light scattering", J. Non-Cryst. Solids **407**, cited By 3, 472–477 (2015).

[202] D. W. G. Smith, and J. G. Powles, "Proton spin-lattice relaxation in liquid water and liquid ammonia", Mol. Phys. **10**, 451–463 (1966), `http://dx.doi.org/10.1080/00268976600100571`.

[203] E. Lang, and H.-D. Lüdemann, "Pressure and temperature dependence of the longitudinal proton relaxation times in supercooled water to –87 °C and 2500 bar", J. Chem. Phys. **67**, 718–723 (1977), `http://dx.doi.org/10.1063/1.434878`.

[204] P. S. Hubbard, "Nuclear magnetic relaxation by intermolecular dipole-dipole interactions", Phys. Rev. **131**, 275–282 (1963), `https://link.aps.org/doi/10.1103/PhysRev.131.275`.

[205] N. Bloembergen, E. M. Purcell, and R. V. Pound, "Relaxation Effects in Nuclear Magnetic Resonance Absorption", Phys. Rev. **73**, 679–712 (1948), `https://journals.aps.org/pr/abstract/10.1103/PhysRev.73.679`.

[206] S. Khodadadi, S. Pawlus, and A. P. Sokolov, "Influence of hydration on protein dynamics: combining dielectric and neutron scattering spectroscopy data", J. Phys. Chem. B **112**, PMID: 18942780, 14273–14280 (2008), `http://dx.doi.org/10.1021/jp8059807`.

[207] S. Khodadadi, S. Pawlus, J. H. Roh, V. G. Sakai, E. Mamontov, and A. P. Sokolov, "The origin of the dynamic transition in proteins", J. Chem. Phys. **128**, 195106 (2008), `http://dx.doi.org/10.1063/1.2927871`.

[208] B. Halle, and M. Davidovic, "Biomolecular hydration: from water dynamics to hydrodynamics", Proc. Natl. Acad. Sci. USA **100**, 12135–12140 (2003), `http://www.pnas.org/content/100/21/12135.abstract`.

[209] A. S. Parmar, and M. Muschol, "Hydration and hydrodynamic interactions of lysozyme: effects of chaotropic versus kosmotropic ions", Biophys. J. **97**, 590–598 (2009), `http://www.ncbi.nlm.nih.gov/pmc/articles/PMC2711313/`.

[210] J. D. Bryngelson, J. N. Onuchic, N. D. Socci, and P. G. Wolynes, "Funnels, pathways, and the energy landscape of protein folding: a synthesis", Proteins: Struct., Funct., Bioinf. **21**, 167–195 (1995), `http://dx.doi.org/10.1002/prot.340210302`.

[211] G. I. Makhatadze, and P. L. Privalov, "Energetics of protein structure", Adv. Protein Chem. **47**, 307–425 (1995), `http://www.sciencedirect.com/science/article/pii/S0065323308605483`.

[212] R. Zwanzig, A. Szabo, and B. Bagchi, "Levinthal's paradox.", Proc. Natl. Acad. Sci. U.S.A. **89**, 20–22 (1992), `http://www.ncbi.nlm.nih.gov/pmc/articles/PMC48166/`.

[213] P. G. Wolynes, J. N. Onuchic, and D. Thirumalai, "Navigating the folding routes", Science **267**, 1619–1620 (1995), `http://science.sciencemag.org/content/267/5204/1619`.

[214] S. Yip, and M. P. Short, "Multiscale materials modelling at the mesoscale", Nat. Mater. **12**, 774–777 (2013), `http://dx.doi.org/10.1038/nmat3746`.

[215] M. Sundaralingam, and Y. C. Sekharudu, "Water-inserted alpha-helical segments implicate reverse turns as folding intermediates", Science **244**, 1333–1337 (1989), `http://science.sciencemag.org/content/244/4910/1333`.

[216] S. T. R. Walsh, R. P. Cheng, W. W. Wright, D. O. V. Alonso, V. Daggett, J. M. Vanderkooi, and W. F. DeGrado, "The hydration of amides in helices; a comprehensive picture from molecular dynamics, IR, and NMR", Protein Sci. **12**, 520–531 (2003), `http://www.ncbi.nlm.nih.gov/pmc/articles/PMC2312439/`.

[217] A. Cooper, "Heat capacity effects in protein folding and ligand binding: a re-evaluation of the role of water in biomolecular thermodynamics", Biophys. Chem. **115**, BIFI 2004 International Conference Biology after the Genoma: A Physical View, 89–97 (2005), `http://www.sciencedirect.com/science/article/pii/S0301462204003539`.

[218] J. Stepišnik, "Time-dependent self-diffusion by NMR spin-echo", Physica B **183**, 343–350 (1993), `http://www.sciencedirect.com/science/article/pii/092145269390124O`.

[219] A. Oleinikova, N. Smolin, and I. Brovchenko, "Influence of water clustering on the dynamics of hydration water at the surface of a lysozyme", Biophys. J. **93**, 2986–3000 (2007), `http://dx.doi.org/10.1529/biophysj.107.108753`.

[220] B. F. Rasmussen, A. M. Stock, D. Ringe, and G. A. Petsko, "Crystalline ribonuclease A loses function below the dynamical", Nature **357**, 423–424 (1992), `http://dx.doi.org/10.1038/357423a0`.

[221] J. Klafter, M. F. Shlesinger, and G. Zumofen, "Beyond brownian motion", Phys. Today **49**, 33–39 (1996), `http://physicstoday.scitation.org/doi/10.1063/1.881487`.

[222] S. Havlin, and D. Ben-Avraham, "Diffusion in disordered media", Adv. Phys. **51**, 187–292 (2002), `http://dx.doi.org/10.1080/00018730110116353`.

[223] R. Metzler, J.-H. Jeon, A. G. Cherstvy, and E. Barkai, "Anomalous diffusion models and their properties: non-stationarity, non-ergodicity, and ageing at the centenary of single particle tracking", Phys. Chem. Chem. Phys. **16**, 24128–24164 (2014), `http://dx.doi.org/10.1039/C4CP03465A`.

[224] F. Mallamace, C. Corsaro, H. E. Stanley, D. Mallamace, and S.-H. Chen, "The dynamical crossover in attractive colloidal systems", J. Chem. Phys. **139**, 214502 (2013), `http://dx.doi.org/10.1063/1.4833595`.

[225] M. Marchi, F. Sterpone, and M. Ceccarelli, "Water rotational relaxation and diffusion in hydrated lysozyme", J. Am. Chem. Soc. **124**, PMID: 12047201, 6787–6791 (2002), `http://dx.doi.org/10.1021/ja025905m`.

[226] J. Kärger, and F. Stallmach, "Pfg nmr studies of anomalous diffusion", in *Diffusion in condensed matter: methods, materials, models*, edited by P. Heitjans, and J. Kärger, (Springer Berlin Heidelberg, Berlin, Heidelberg, 2005) Chap. 10, pp. 417–459, `https://doi.org/10.1007/3-540-30970-5_10`.

[227] Z. Hu, J. Jiang, and S. I. Sandler, "Water in hydrated orthorhombic lysozyme crystal: insight from atomistic simulations", J. Chem. Phys. **129**, 075105 (2008), `http://dx.doi.org/10.1063/1.2969811`.